The Thesis committee for Andrew Joseph Kurzawski
certifies that this is the approved version of the following thesis:

Ablation and Ignition by Impinging Jet Flows

APPROVED BY

SUPERVISING COMMITTEE:

Supervisor: _____
Ofodike A. Ezekoye

_____
Joseph H. Koo

Ablation and Ignition by Impinging Jet Flows

by

Andrew Joseph Kurzawski, B.S.M.E.

THESIS

Presented to the Faculty of the Graduate School of

The University of Texas at Austin

in Partial Fulfillment

of the Requirements

for the Degree of

MASTER OF SCIENCE IN ENGINEERING

The University of Texas at Austin

December 2013

This thesis is dedicated to my family and friends for their constant support and encouragement.

Acknowledgments

First, I would like to thank my advisor, Dr. Ofodike Ezekoye, for sharing his extensive knowledge of heat transfer and providing guidance throughout my studies. This work was made possible by the efforts of Dr. Ezekoye in leading a research group that values sharing and pursuing knowledge. I would like to thank Dr. Joseph Koo for his helpful feedback on my thesis. I would also like to thank Dr. Koo and the researchers who conducted the ablation experiments, especially Colin Yee and Dr. Maurizio Natali, for their work and collaboration. Additionally, I would like to thank the past University of Texas Fire Research Group members who contributed to the burn structure construction and experiments, including Dr. Colin Beal, Dr. Craig Weinschenk, Dr. Kristopher Overholt, and Kevin Carollo. I would not have been able to write this thesis without the efforts of these researchers.

I would like to thank Dr. Kristopher Overholt for sharing his strong passion for all things fire. I am thankful for his contributions to the University of Texas Fire Research Group (UTFRG), as well as his friendship and encouragement in the pursuit of my graduate studies. I would like to acknowledge other past and present UTFRG members for their camaraderie and willingness to discuss interesting problems and ideas, especially Jan-Michael Cabrera, Mustafa Abbasi, and Austin Anderson. I would also like to thank several other friends and colleagues who have made my graduate school experience enjoyable, especially Kristin Ramsey, David Dinh, and Alex Headley.

Finally, I would like to thank my parents, Anne and Ken, and my brother Phil for all that they have done for me. I am constantly thankful for the love and support

of my family.

Ablation and Ignition by Impinging Jet Flows

Andrew Joseph Kurzawski, M.S.E.
The University of Texas at Austin, 2013

Supervisor: Ofodike A. Ezekoye

Two separate heat transfer problems that involve jet flows impinging on a reacting target are studied through modeling and experimentation. The first system is an ablating carbon-carbon specimen exposed to high heat fluxes from an oxy-acetylene torch which has applications in atmospheric re-entry vehicles. The second system involves the penetration of hot gases into the void space in a compartment. The fire protection stands to benefit from knowledge of this system, both in building component design and informing firefighting personnel. Both problems can be modeled as a jet flow impinging on a flat surface where hot gases from the jet lead to primarily convective heat transfer.

Ablation experiments are outlined and a theoretical framework is developed. A serial inversion technique is tested for predicting the recession rate observed in the experiments. A novel inversion technique that takes advantage of parallel computing is developed to circumvent the shortcomings of the serial technique. These techniques are then compared to synthetically generated and experimental data for different data streams and error signals.

Compartment-scale experiments were conducted to test hot gas penetration into void spaces. Anecdotal evidence was observed outside of the intended test section

prompting further investigation into the mechanics of ignition in void spaces. A theoretical framework is established to predict possibility of ignition under varied environmental factors. A leakage-scale experiment is constructed to gain insight into conditions that result in ignition of materials in void spaces.

Table of Contents

Acknowledgments v

Abstract vii

List of Tables xii

List of Figures xiii

Chapter 1. Introduction: Ablation and Ignition by Impinging Jet Flows 1

1.1 Introduction 1
1.2 Ablation Problem Motivation and Introduction 2
1.3 Void Space Ignition Problem Motivation and Introduction 5

Chapter 2. Ablation: Recession Experiments and Modeling for Carbon Surface Oxidation Processes 10

2.1 Recession Experiments and Modeling Overview 10
2.2 Ablation Experimental System 10
2.2.1 Sample production and instrumentation 11
2.2.1.1 Ablation Testing Setup 14
2.2.1.2 Ablation Test Results 16
2.2.2 Acoustic Time of Flight Analysis 19
2.3 Forward Thermal Ablation Model 20
2.4 Thermal-Acoustic Inversion 24
2.4.1 Serial Inversion Algorithm 25
2.4.1.1 Serial Inversion Performance for Different Error Signals 27
2.4.1.2 Serial Inversion on Experimental Data 30
2.4.2 Parallel Inversion Algorithm 32
2.4.2.1 IHS Implementation 33
2.4.2.2 Performance 36
2.4.3 Comparison of IHS and Serial Inversion on Synthetic and Experimental Data 39
2.5 Conclusions 45

Chapter 3. Void Space Ignition **47**
3.1 Void Space Ignition Overview 47
3.2 Compartment-Scale Experimental System and Characterization 47
3.2.1 Experimental burners and HRR 49
3.2.2 Fan specification 50
3.2.3 Experimental conditions 50
3.3 Computational Fluid Dynamics Model Setup 52
3.4 Experimental and Computational Results 53
3.4.1 Temperature measurements 53
3.4.2 Pressure predictions 55
3.4.3 Thermal penetration 57
3.5 Theory and Analysis 61
3.5.1 Compartment scale 61
3.5.2 Leakage scale 64
3.5.3 Analysis 67
3.6 Small Scale Experimental System 70
3.6.1 Development of experiment 71
3.6.2 Scoping 75
3.6.3 Flow characterization 80
3.6.4 Ignition Experiments 80
3.7 Conclusions 87

Chapter 4. Conclusions **90**
4.1 Conclusions 90

Appendices **92**

Appendix A. Iterative Hypercube Sampler Code Excerpts **93**
A.1 Root Processor 93
A.2 Worker Processors 93

Appendix B. Void Box Experimental Method **95**

Appendix C. Void Space Experimental Data **97**
C.1 Test Matrix 97
C.2 Temperature Plots 99
C.3 Pressure Plots 106
C.4 Char Patterns 110

Bibliography **112**

Vita **117**

List of Tables

2.1 Total recession, test duration, and recession rates for the tests 1-3. . . 19
2.2 Example model input parameters 23
2.3 Iteration parameters 25
2.4 Synthetic parameter values and percent error for three error modes with the serial algorithm. 27
2.5 Recession. 30
2.6 Timing for IHS code (Serial time = 11.8 hours) 37
2.7 Efficiency and idle processors during the last scatter/gather of each iteration 39
2.8 Synthetic parameter values and percent error for three error modes with the IHS algorithm. 40
2.9 Recession. 41
2.10 Comparison of error inverting for experimental data with the serial and IHS algorithms. 42
2.11 Total recession for the tests 1-3 compared to IHS predicted total recession. 45

3.1 Scoping tests and findings. 76
3.2 Results of OSB ignition tests, "X" indicates no ignition event occurred, "N" indicates not cataloged (*Outlet thermocouple slipped out of alignment). 82
3.3 Calculated Reynolds number, Nusselt number and heat transfer coefficient for ignition tests (omitting tests 9 and 14). 86

C.1 Scoping raw inputs and absolute timing. 98
C.2 Char pattern dimensions for ignition experiments (*Char pattern reached the edge of the sample). 110

List of Figures

1.1 Schematic of a jet impingement flow. 2
1.2 Potential access points for hot gas to enter the void space on a standard wall. 7
1.3 Test section with leakages highlighted by red circles. 8

2.1 Post burning image of the CC plug 12
2.2 Dimensions of the sample and thermocouple holes. 13
2.3 Full view of the OTB with an unburned C/C sample. 15
2.4 C/C sample plug with thermocouples in the brass holder. 15
2.5 Temperature profiles for four thermocouple experiments 1-3. 17
2.6 Distance versus thermocouple break time at 1432^{o}C for tests 1-3. . . 18
2.7 Autocorrelation with an enveloping function 20
2.8 Schematic of the transducer setup for a non-ablating test. 21
2.9 Schematic of ablating system 21
2.10 Example temperature profiles for a test with four thermocouples . . . 23
2.11 Finding the minimum error using the golden section search for a specific parameter v_j 26
2.12 Temperature and Time of Flight for single temperature error signal. . 28
2.13 Temperature and Time of Flight for time of flight error signal. 29
2.14 Temperature and Time of Flight for time of flight and single temperature error signal. 29
2.15 Temperature profiles for Test 1 (left) and Test 2 (right) with four thermocouples. 31
2.16 Basic operation of the Iterative Hypercube Sampler (IHS): a search space is defined in step 1, samples are drawn in step 2 and repeated for a set number of iterations, the minimum error is found in step 3, and a new search space is defined (refinement) in step 4. 34
2.17 Workflow of IHS code 35
2.18 Speedup for M^N=729 38
2.19 Temperature and Time of Flight for IHS inversion with a combination error signal (top) and temperature only error signal (bottom). 41
2.20 Temperature and Time of Flight for IHS inversion with a time of flight error signal. 42

2.21 Experimental and IHS predicted temperature profiles for Test 3 with two point error (left) and one point error (right). 43
2.22 Recession rate time history predicted by the IHS and manual recession rate for tests 1-3. 44

3.1 Geometry of the burn structure at The University of Texas at Austin. 48
3.2 Mid-elevation failure location front view (left) and test section rear view (right). 49
3.3 Plan view of burn structure showing burner and thermocouple locations. 52
3.4 Temperature profiles at several thermocouple trees and various elevations. 54
3.5 Natural ventilation (left) and improper PPV (right) for 150 kW fire cases. 54
3.6 Natural ventilation (left) and improper PPV (right) for 400 kW fire cases. 55
3.7 Pressure profiles for (a) natural ventilation (b) proper PPV and (c) improper PPV. 56
3.8 Electrical outlet mounted at mid wall elevation prior to fire (left) and typical plugs and switches post fire (right). 58
3.9 Smoke alarm placement at upper level of fire compartment (left). Close-up view of smoke detector (top right) and half-inch gap behind smoke detector for electrical wiring access (bottom right). 59
3.10 Void space cavity shown from back view (left), inset of void space showing half-inch smoke alarm wiring access gap (top right), wood placed in void space adjacent to wiring gap (middle right), and fiberglass insulation surrounding wood panel in void space (bottom right). 60
3.11 Post-fire damage to wood panel in void space behind smoke detector access hole (left) and thermocouple temperatures behind smoke detector in void space (right). 60
3.12 Compartment scale heat and mass transfer schematic connected to the leakage scale. 62
3.13 Leakage outlet temperature versus geometry for Leakage Height = 2.4 m and HRR = (left) 400 kW and (right) 150 kW. 68
3.14 Leakage outlet temperature versus HRR and hole diameter for a fixed leakage diameter = 1 cm and leakage height = 2.4 m). 69
3.15 Top down illustration inside the void box. 72
3.16 Steel diffuser. 73
3.17 Void box setup for scoping tests 1 through 3. 74
3.18 Sample holder with drywall (left) and oriented strand board (right) targets. 75

3.19 Temperatures during scoping test 4 inside the box (left) and at the outlet and target (right). The leakage section was inserted at 120 seconds, the target was positioned 300 seconds, and the gas was turned off at 450 seconds. 78
3.20 Temperatures during scoping test 7 inside the box (left) and at the outlet and target (right). 78
3.21 Full experimental set up. 79
3.22 Velocity versus gage pressure for room temperature leakage test. . . . 80
3.23 Anemometer set up for room temperature leakage test. 81
3.24 Char pattern for test nine. 83
3.25 Charring observed on tape after test fourteen (left) and staple arrangement for securing the outlet thermocouple (right). 83
3.26 Charring observed ten seconds after target was positioned (left) and brief flame flicker at 282 seconds after target was positioned (right). . 84
3.27 Flickering OSB before the burner was turned off (left) and intensified glowing after the burner was turned off and the air left on (right). . . 85
3.28 Time to ignition versus average outlet temperature for OSB samples at 1cm spacing (left) and 2.5cm spacing (right). Red indicates glowing ignition and blue indicates flaming ignition. 87

Chapter 1

Introduction: Ablation and Ignition by Impinging Jet Flows

1.1 Introduction

The body of this work examines two separate heat transfer problems that both involve jet flows impinging on a reacting target. The focus is on deepening the understanding in each system through the development of theory, experiments, and modeling that works towards practical application of the findings of this work. The first system is an ablating carbon-carbon specimen exposed to high heat fluxes from an oxy-acetylene torch. The goal is development of a system that can calculate the rate of material loss with applications for re-entry vehicles. The second system involves the penetration of hot gases into the void space in a compartment. Understanding the ignition risk for this scenario has applications in building fire protection, both for building component design and informing firefighting personnel.

Both problems can be modeled as a jet flow impinging on a flat surface as illustrated in Figure 1.1. Hot gases flowing from the jet lead to primarily convective heat transfer to the target material. In the ablation process, solid material is liberated from the target and in the void space problem, this heating can lead to pyrolysis and ignition of the material. Using the overarching theme of impinging jet heat transfer, the work embodied in this thesis seeks to understand the issues associated with the two scenarios through experimental and modeling efforts.

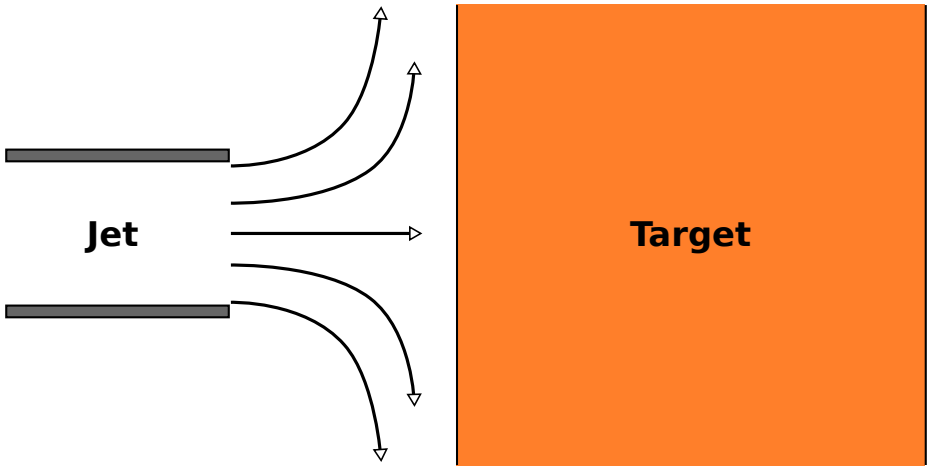

Figure 1.1: Schematic of a jet impingement flow.

1.2 Ablation Problem Motivation and Introduction

Re-entry vehicles are equipped with thermal protection systems (TPS) that are designed to withstand exposure to extreme conditions. Typically, these vehicles will experience greater than Mach 3 speeds at essentially atmospheric-pressure, upstream conditions for durations of tens to hundreds of seconds. The surface is expected to experience maximum temperatures in the range of 2000 K to 3000 K. The external surface of the vehicle is designed to primarily protect the aerostructure from thermal loading from the high energy external flow conditions and must also work as an aerodynamic body and as a structural component [1, 2]. Surfaces of interest must be tailored to a particular trajectory and are constrained by various engineering constraints, such as weight and structural and thermochemical robustness. Current external surfaces use materials such as carbon/carbon composites (CCCs) as well as CCCs overlaid with various thin films, such as Si3N4, SiC, HfB2, etc. One subset of TPS is designed to dissipate heat through thermochemical erosion of the surface of the system.

The development of novel TPS will rely on reliable sensor system able to

characterize the evolution of the TPS as it is thermochemically assaulted. There are interesting constraints and requirements for sensor systems that can be used to characterize the TPS and measure ablation rates. These constraints include the need to resolve relatively small changes in the ablative material given that the ablation rates for many systems are quite small (i.e., order 0.01 - 1 mm/sec). Also, depending on the trajectory, there is a possibility of ionized gases (e.g., in re-entry scenarios). Finally, the primary requirement of the TPS is to absorb heat and thus the temperature distribution and heat load of the ablative material will evolve in time. Thus, one must identify in advance the type of trajectory and the type of TPS material of interest as one envisions the particular type of sensor system to include. The various types of constraints that exist in TPS thickness characterization lead one to explore so-called sensor fusion processes in which multiple sensors are used with software and modeling glues connecting the sensor signals together in order to retrieve a coherent picture of the TPS evolution.

Many different technologies for recession sensors have been tested in entry vehicle applications, primarily with high-density ablating TPS materials. Simpler sensors have been based on the use of thermocouples and "breakwire" arrangements. In a breakwire sensor arrangement, multiple thermocouples or pairs of wires are embedded in a TPS plug with their junctions located at different depths. As the TPS surface recedes, the penetrating local temperature profile initially changes the resistance of each wire and then melts each wire at some failure temperature, breaking the electric circuit. However, for some ablators, the thermally modified material (e.g., char) is electrically conductive, and even with the failed wires, can produce incorrect sensor readings, hindering interpretation of the real status of the TPS.

A second type of electrical measurement system can be developed using a

capacitance measurement principle. Shull et al. [3] show the use of such systems in measuring the properties (including thickness) of a variety of conducting and dielectric materials including PMMA. The basic sensor consists of a source and receiver. The problems with using a purely capacitive system are that the sensor will respond not only to the change in thickness of the sample, but also to chemical composition changes associated with thermal degradation. The sensor system would have to be able to delineate composition and thermal changes from simple recession and shape change. Again, this suggests that a sensor system in which the compositional changes as well as the recessional changes are taken into consideration.

Recession might also be measured by means of ultrasonic transducers and receivers. This method of recession measurement has not been widely used in a planetary probe environment. An ultrasonic transducer produces an acoustic wave through the TPS material. A part of the wave is reflected back toward the receiver when it reaches the extent of the material. Various types of source-receiver configurations are commonly used for non-destructive testing (NDT). Pulse-echo and pitch-catch configurations are typical. Sample thickness can be determined from time of flight of the acoustic wave. A benefit of this system, like a capacitance system, is the non-destructive nature of an ultrasonic transducer. The problem with the use of ultrasonic time of flight transducers is that the signals depend on the local speed of sound within the TPS which is temperature and composition dependent. For unsteady recession, the temperature profile and the TPS composition are unknown and thus errors are likely if one uses the ultrasonic transducers as stand-alone sensors. There is need for temperature measurements and an inversion technique to correct the acoustic signal interpretation.

This work explored the development of fast computational algorithms that

can support the real-time sensor measurements using data assimilation methods. Of particular interest and importance will be the use of inverse heat transfer (IHT) analysis to thermally characterize the TPS response using a minimum number of in-depth temperature measurements. The problem formulation in IHT is mathematically ill-conditioned and regularization techniques are applied to generate meaningful solutions. Several studies in the literature have applied IHT techniques to determine ablation rate or wear rate [4–6].

This work examined experimental and numerical use of a coupled-transducer system comprised of thermocouple temperature measurements and time of flight acoustic measurements to determine the recession rate of a carbon-phenolic ablative material. The ablation experiments were conducted in an Oxy-acetylene Test Bed (OTB). This requires the construction of a numerical ablation model and wrapper that inverts for the temperature profile and ablation rate.

1.3 Void Space Ignition Problem Motivation and Introduction

A fire contained within a room can spread into void spaces in the walls and ceiling through penetrations in the material that lines the compartment. This can be problematic for firefighters conducting overhaul operations because a fire located within the void space can be difficult to detect and failure to do so can result in fire spread through the void spaces to other rooms within the structure. Few studies have looked at how a room and contents fire transitions to a structural fire. With respect to ventilation, it is unknown if application of positive pressure ventilation (PPV) affects this transition. One of the active areas of fire research is the coupling of the fire to the structure. Lightweight wood frame construction represents the majority of residential construction in the U.S. The construction details and choice of materials will affect

the overall fire resistance of the structure. Adherence to building code standards on fireproofing and use of less flammable materials will obviously reduce the likely loss if a fire takes place. Because of the relative lack of knowledge on the fire penetration into wall spaces, this research examined how fire might penetrate into the void spaces of wood framed structures.

The primary type of structure that poses the greatest risk to a structure fire transition is a wood framed structure with balloon frame. Mittendorf [7] reported that platform construction effectively began in the 1950s. Prior to that, balloon frame construction was used in a significant fraction of residential structures. In balloon frame construction, the wall studs extend from the ground floor through the second floor and into the attic. Unlike in platform construction where plates are used to frame walls for each floor, in balloon frame construction, there sometimes is no inherent fire stopping mechanism inhibiting the spread of fire between floors. The American Wood Council in the 2001, Details for Conventional Wood Construction, makes clear the need for firestopping in new balloon frame construction. For older balloon frame construction, it is not apparent the extent to which firestops were used in construction. The lack of inherent firestopping in balloon frame construction buildings is one of the main reasons for the concern about the use of PPV in such buildings.

In the U.S.A., a critical barrier to the penetration of hot gas products into void spaces is provided by the gypsum-board skin of the compartment. For most compartments, there are many penetrations within the compartment's gypsum-board skin. Common potential access points include security system wiring (e.q. smoke detectors and cameras), ventilation fixtures, light switches, and electrical outlets among others (Fig. 1.2). A hole in the gypsum may create opportunities for void space ignition.

One of the purposes of this work is to identify hole size, fire size, and hole locations that are prone to igniting a given material in void spaces.

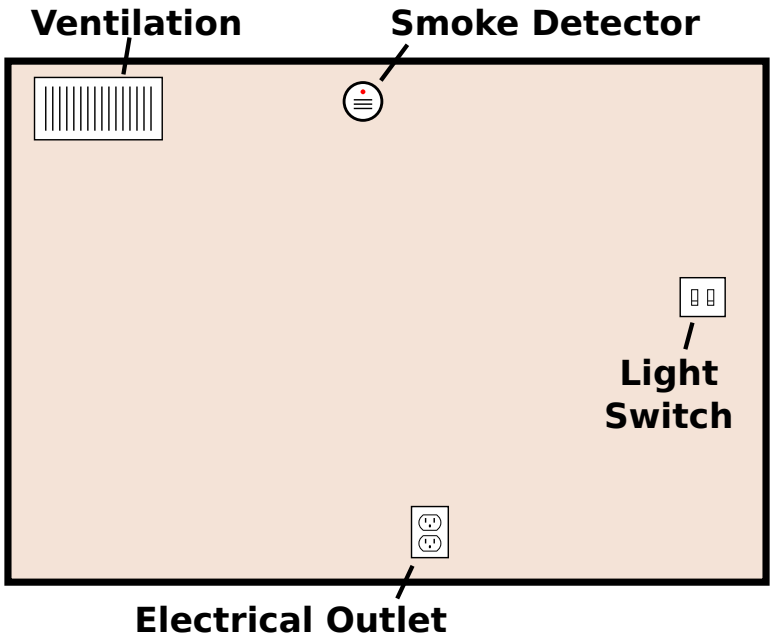

Figure 1.2: Potential access points for hot gas to enter the void space on a standard wall.

An experimental room was outfitted with representative leakages located in a test section that contains a void space. Figure 1.3 shows two leakages; a square hole at mid-compartment height representative of an electrical outlet or light switch panel and a smaller rectangular slot ceiling height representative of a hole cut out to provide wiring access for devices such as smoke detectors or security systems.

There is evidence that PPV, when used properly, can improve the conditions for victims and firefighters [7]. Some practical details of this technique are available [8–12]. Svensson [13] conducted experiments with a 370 kW fire in a three-room training facility and concluded that PPV increases the heat release rate (HRR) of the fire, reduces temperature on the upwind side of the fire, and increases the temperature on the downwind side. Kerber and Walton [14, 15] analyzed the fan flow associated with

Figure 1.3: Test section with leakages highlighted by red circles.

PPV and have also analyzed the effects of PPV on the fire room conditions. Among other things they found that after application of PPV there was an initially sharp rise in the HRR relative to natural ventilation conditions, but that this increase in HRR was of relatively short duration. After some time, the HRR dropped below the level associated with natural ventilation. Previous studies conducted by the University of Texas Fire Research Group (UTFRG) have highlighted various aspects of PPV [16–19], but has not detailed how a fire can transition from a room contents fire to a structure fire.

This work was motivated by tests performed between two limiting conditions: natural ventilation and improper PPV. Room temperatures and pressures for these tests were determined from experiments and modeling. Temperature data was also taken within a void space built into the room-scale test chamber and in one case ignition was observed in one of the wooden frame elements behind the gypsum board. Further modeling done at the leakage scale to examine effects of leakage and environ-

ment variables (leakage geometry, gas temperature, pressure, etc.) on the possibility for ignition of a material located within the void space. Leakage-scale experiments were conducted to understand ignition in the void space that can cause a room and contents fire to transition into a structure fire.

Chapter 2

Ablation: Recession Experiments and Modeling for Carbon Surface Oxidation Processes

2.1 Recession Experiments and Modeling Overview

The work in this chapter builds upon recession experiments conducted by the Koo research group and Dr. Natali of the University of Perugia published in the proceedings of the 49th AIAA/ASME/SAE/ASEE Joint Propulsion Conference [20, 21]. Along with some experimental results, part of the modeling work in this chapter was published by the author in the proceedings of the ASME Summer Heat Transfer Conference [22]. It begins with the design, production, and setup of the experimental ablation system, then details the results of one set of recession experiments and preliminary acoustic analysis, and proceeds to the construction of a forward thermal model for an ablating system. Lastly, two inversion techniques are presented and compared for performance on synthetic and experimental ablation data.

2.2 Ablation Experimental System

A coupled acoustic and thermal experimental system was developed. This required the design and testing of methods for taking thermal and acoustic measurements of a sample material exposed to low power heating and the oxy-acetylene test bed (OTB).

The original OTB was built by Dr. Natali at the University of Perugia, Italy [23]. This system used 0.25 mm miniture K-type thermocouples in both four

and eight tier configurations where the thermocouples are staggered 0.5 mm between tiers beginning 2 mm from the front (hot) face of the sample [20]. A series of tests were conducted on sample plugs made of carbon/carbon (C/C) material. As the plug is heated the thermocouples provide data about the temperature profile within the plug, and finally break when the ablation front reaches the thermocouple and destroys the junction in the tip of the thermocouple. By knowing the depth of the thermocouple and the time at which it broke, the position of the ablation front and rate of ablation can be calculated in real time.

At the University of Texas (UT) at Austin, an OTB similar to Dr. Natali's setup was built by Eric Allcorn [24] for easy comparison of experimental data. The UT OTB used 0.5 mm TCs and less expensive production methods to cut down on testing costs. The following sections summarize the work of Yee *et al* [21] from which data will be used in testing inversion methods presented later in this chapter. Yee's tested six C/C samples with four thermocouple tiers and three C/C samples with nine thermocouple tiers. Additionally, four carbon phenolic samples with four thermocouple tiers were tested in this OTB.

The inversion methods developed in this thesis will be compared to the experimental data from the first three C/C tests with four thermocouple tiers from Yee. To date, the OTB technology has been tested extensively on two types of C/C composites (low density C/C and high density C/C) on a hole configuration based on blind holes [20, 21]. The following sections summarize experimental development work carried out by Yee and the results of the first three C/C tests.

2.2.1 Sample production and instrumentation

The C/C plugs had to have dimensions of 15 mm x 15 mm x 15 mm so that they could be mounted and used with the OTB. Thermocouples larger than 0.25 mm

had to be used, but all of the thermocouples needed to fit within the torch diameter of roughly 3 mm. As seen in Figure 2.1, the oxyacetylene torch acts upon the sample in a cone. By keeping the holes closer together, the four thermocouples will experience the same heat flux and remain within the deepest section of the ablation crater. The deepest hole was drilled at 13.0 mm (2.0 mm from the hot surface) and the remaining thermocouples were staggered at 0.5 mm increments (i.e. 2.5 mm, 3.0 mm from the surface, etc.).

Figure 2.1: Post burning image of the CC plug

The distance between the thermocouples must be large enough to maintain structural stability of the sample and prevent cross-talk between the thermocouples because C/C is a conductive material. A spacing of 2 mm was used for 0.5 mm thermocouples in the UT experiments compared to Dr. Natali's original 1 mm spacing for 0.25 mm thermocouples (later increased to 2 mm for ease of production). Creating holes for the thermocouples was accomplished with a #73 drill (0.610 mm diameter) which leaves roughly 0.1 mm of clearance for the thermocouple adhesive and increases the ease of assembly. Figure 2.2 shows the dimensions of the final sensor plug and

thermocouple depths for a four thermocouple arrangement.

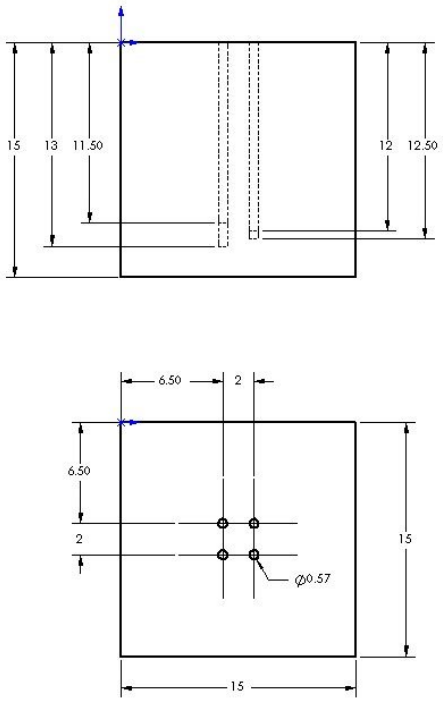

Figure 2.2: Dimensions of the sample and thermocouple holes.

Conventional drilling was chosen for its low cost compared to Electrical Discharge Machining (EDM) that was used for creating the original samples. Laser drilling was also tested on the original samples but the quality of holes produced by EDM was found to be superior. Ultimately, larger thermocouples and conventional production methods helped to greatly reduce the cost of experiments. The C/C plugs were constructed in two main steps: the holes were machined with conventional drilling and the thermocouples were installed with a high-temperature adhesive. Drilling was done in three steps to reduce the risk of drill bit breakage. If the drill bit broke in a hole, the sample had to be discarded because the broken bit could not be removed. An adhesive was used to secure the thermocouples inside the C/C plugs. This graphite-based epoxy was chosen for its high strength and ability to

resist high intensity thermal conditions for a short amount of time.

2.2.1.1 Ablation Testing Setup

The oxyacetylene torch mounted in the OTB is capable of producing flame temperatures up to 3000^oC and it was adjusted for these tests to produce a heat flux of 940 MW/m^2. This is comparable with the experimental conditions in Dr. Natali's original tests. The four thermocouples were connected to a data acquisition device (DAQ) and at a rate of 10 Hz. The duration of time that the samples were exposed to the torch ranged from 90 to 180 seconds in these experiments. Figure 2.3 shows the torch mounted in the OTB. There are slides for positioning the torch and an adjustable screw to fix the flame at a distance of 6 mm. This spacing was determined to produce the desired heat flux of 940 MW/m^2 and the calibrations were conducted by Eric Allcorn [24]. A metal shield for protecting the sample while the torch is being lit is mounted on a slider perpendicular to the torch slider mounts.

The OTB contains a vice that holds the brass sample holder. This sample holder was initially developed to hold cylindrical samples, so additional holes were drilled and tapped to securely hold the cube shaped samples (Fig. 2.4).

The torch was regulated by flow meters for fuel and air with both gases kept at a gage pressure of 0.5 bar. The flow for the experiments was set at a 1:5 fuel to air ratio to produce the required heat flux. The test procedure is as follows: the steel plate was used to block the sample while only acetylene was supplied to the torch and ignited, then the air was brought up to a 1:1 fuel to air ratio, the acetylene was adjusted to its final value, and finally the air was adjusted to a 1:5 fuel to air ratio. At this point the DAQ software was started and the heat shield was removed before bringing the flame into position at 6 mm from the sample. Each test was run for the prescribed amount of time at which point the torch was turned off and the DAQ was

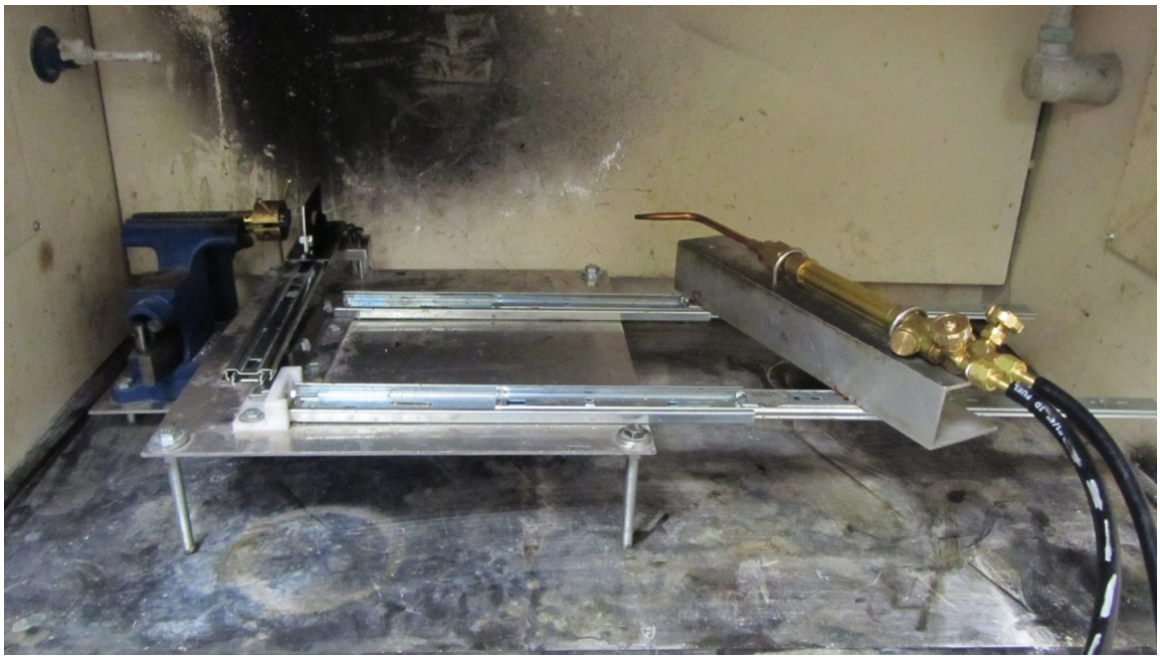

Figure 2.3: Full view of the OTB with an unburned C/C sample.

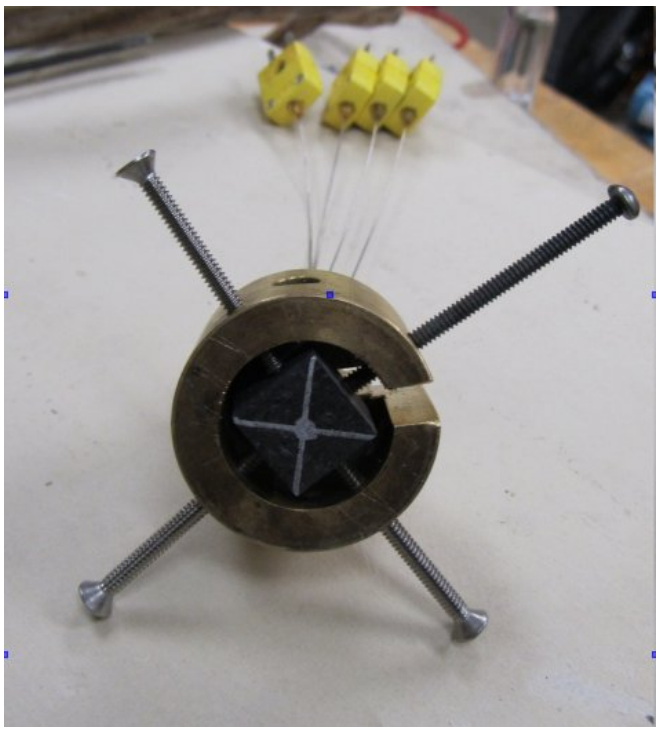

Figure 2.4: C/C sample plug with thermocouples in the brass holder.

left running while the sample cooled.

Two preliminary 90 second exposure tests were conducted on C/C samples to check the torch calibration. The recession rate was calculated by measuring the crater depth with digital calipers and dividing by the test time. The first sample was the same as Dr. Natali's original material and the recession rate matched within experimental uncertainty. The UT test had a recession rate of 0.054 ± .007 mm/s compared to 0.057 ± .007 mm/s for Dr. Natali's sample. The second sample was a denser C/C and had an ablation rate of .032 ± .007 mm/s. This value was used to calculate a test time of 180 seconds to produce a burn depth of 3.5 mm so that all four thermocouples would be damaged and the ablation front could be tracked.

2.2.1.2 Ablation Test Results

Six rounds of C/C four tier tests were conducted using the procedures detailed above. The first three tests are described in this section for analysis with the inversion techniques presented in the following sections. Further testing was conducted on C/C samples with nine thermocouple tiers and carbon phenolic samples with four tiers the results of which can be found in Yee *et al* [21].

The temperature profiles for tests one through three are displayed in Figure 2.5. Breakage occurs when flame reaches the thermocouple which is evident by a sharp jump or instability in the signal. Unstable data recorded after breakage was removed in Figure 2.5 to improve readability.

It was expected that the thermocouples would break sequentially beginning with the thermocouple located closest to the surface, however, this did not occur in all three cases. This could be due to inconsistent heat flux applied to the samples. Further analysis showed that the thermocouples broke at different temperatures so a

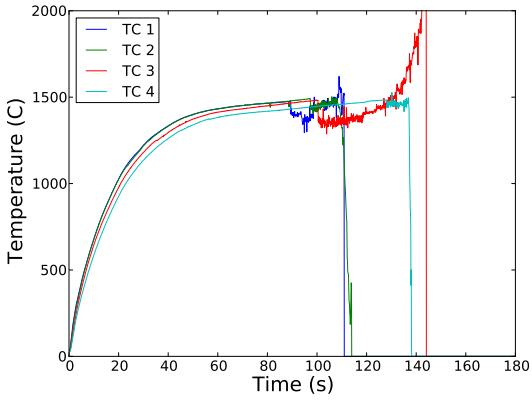

(a) Test 1

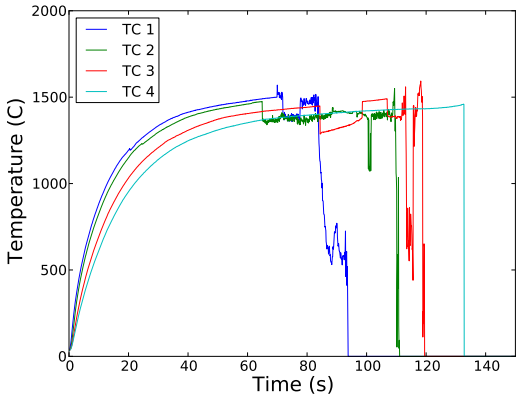

(b) Test 2

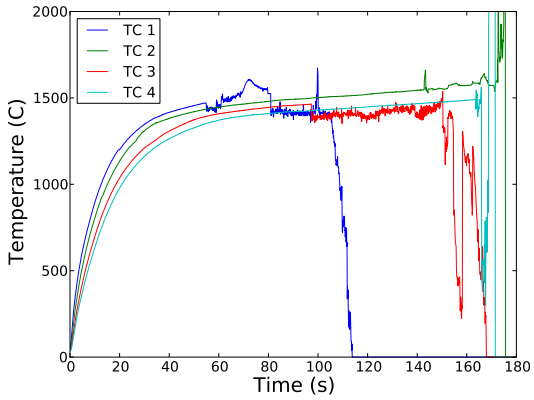

(c) Test 3

Figure 2.5: Temperature profiles for four thermocouple experiments 1-3.

"break temperature" was formulated to determine the recession rate. This was done by averaging the final break temperature of all the thermocouples (1482 ± 25^{o}C) and subtracting two standard deviations to arrive at a value of 1432^{o}C. Two standard deviations were used to ensure that the break temperature was reached by at least 98% of the thermocouples.

Time to break was measured as the time to reach 1432^{o}C. This was assumed to be the point at which the flame reached the thermocouple. Figure 2.6 shows the erosion distance versus time for each of the three tests, with the dots indicating the

time at which each thermocouple reached the break temperature. Using a boundary condition of no erosion at time equals zero, a trend line was fit to the break time data to determine the average recession rate. This value was calculated as the slope of the trend line.

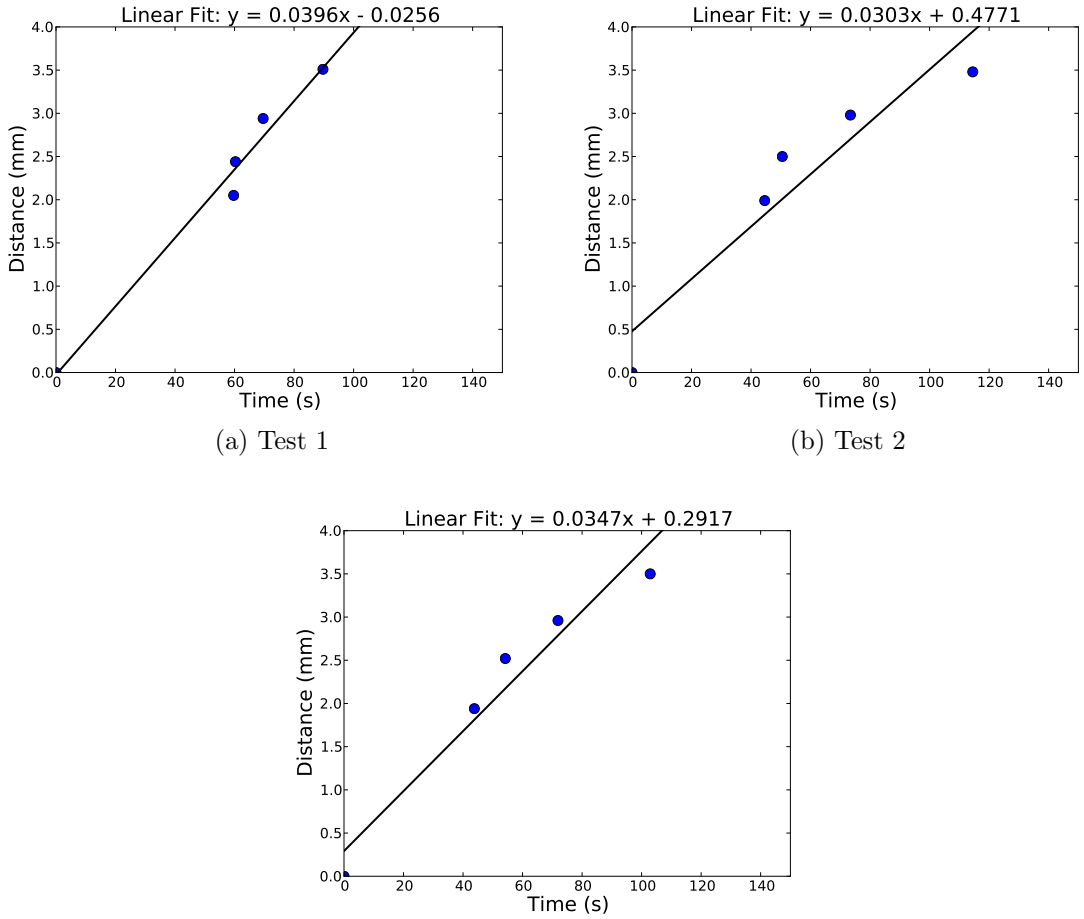

(a) Test 1

(b) Test 2

(c) Test 3

Figure 2.6: Distance versus thermocouple break time at 1432^{o}C for tests 1-3.

The average recession rate is compared to the manual recession rate in Table 2.1. The manual recession rate was determined by measuring the final crater depth in the sample after testing and dividing by the test time in which the sample was exposed to the flame.

Table 2.1: Total recession, test duration, and recession rates for the tests 1-3.

Test Number	Test Duration (s)	Total Recession (mm)	Manual Recession Rate (mm/s)	Average Recession Rate (mm/s)
1	180	7.14	0.0397	0.0396
2	150	4.55	0.0303	0.0303
3	180	4.73	0.0263	0.0347

We can see that the average recession rate matched well with the manual recession rate for tests one and two, which shows that the average recession rate could be used to predict the total recession. However, the average recession rate for test three was calculated to be 0.0347 mm/s which multiplied by the test duration equates to an over-predicted total recession distance of 6.25 mm compared to the experimental value of 4.73 mm.

2.2.2 Acoustic Time of Flight Analysis

For the acoustic measurements, a pulse-receiver and ultrasonic transducer were used to measure sample thicknesses of a carbon-phenolic material for non-ablative (purely heating) cases. In order to accurately determine time delays, the measured waveform must be cross-correlated with itself. Since back reflections occur at a periodic rate, there is a specific time delay that, if applied to a received waveform, would make that instance of the waveform very similar to the original instance. In Figure 2.7), it can be seen that at a time delay of $t_{delay} = 0$, the autocorrelation has its global maximum because at this point the waveform is most similar to another instance of itself. The desirable time delay is the one that is located at a local maximum, which occurs at 8.48 μs as shown in Figure 2.7. This figure shows that the local maximum was calculated by applying an enveloping function, in turn finding the local maximum of that enveloping function.

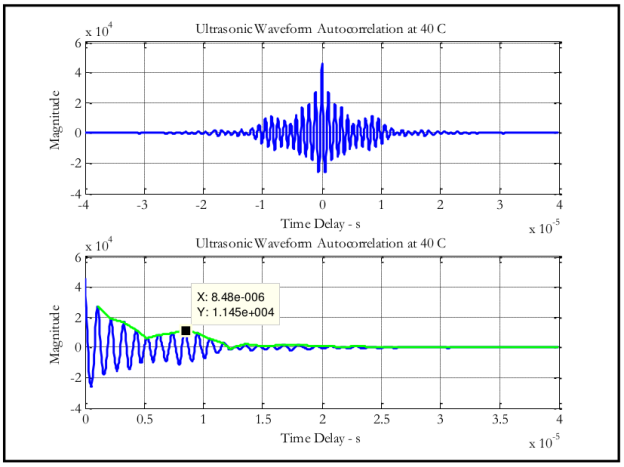

Figure 2.7: Autocorrelation with an enveloping function

Received time delays are inadequate when the speed of sound is not known in the sample. Since the speed of sound is largely affected by temperature, it is necessary to observe the temperature changes at different depths in the sample. One of the motivators for the coupled acoustic-thermal analysis system is the need for internal temperature measurements. With these temperature data points, a temperature profile in the specimen can be fitted around the measured data. To generate a temperature profile that will fit the data, a thermal model of the ablating system must be created.

2.3 Forward Thermal Ablation Model

To predict the thermal conditions and recession rate in the ablation experiments, a simple finite volume model has been constructed for the unsteady temperature distribution in an ablation solid, $T(x,t)$. A schematic of the ablation process and relevant physical parameters is depicted in Figure 2.9, where T is temperature inside the material, u is the recession velocity and α is the thermal diffusivity.

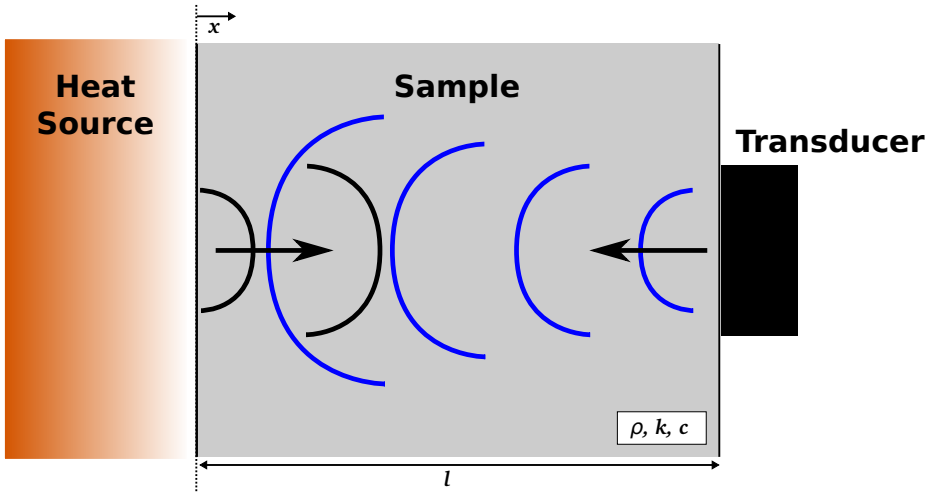

Figure 2.8: Schematic of the transducer setup for a non-ablating test.

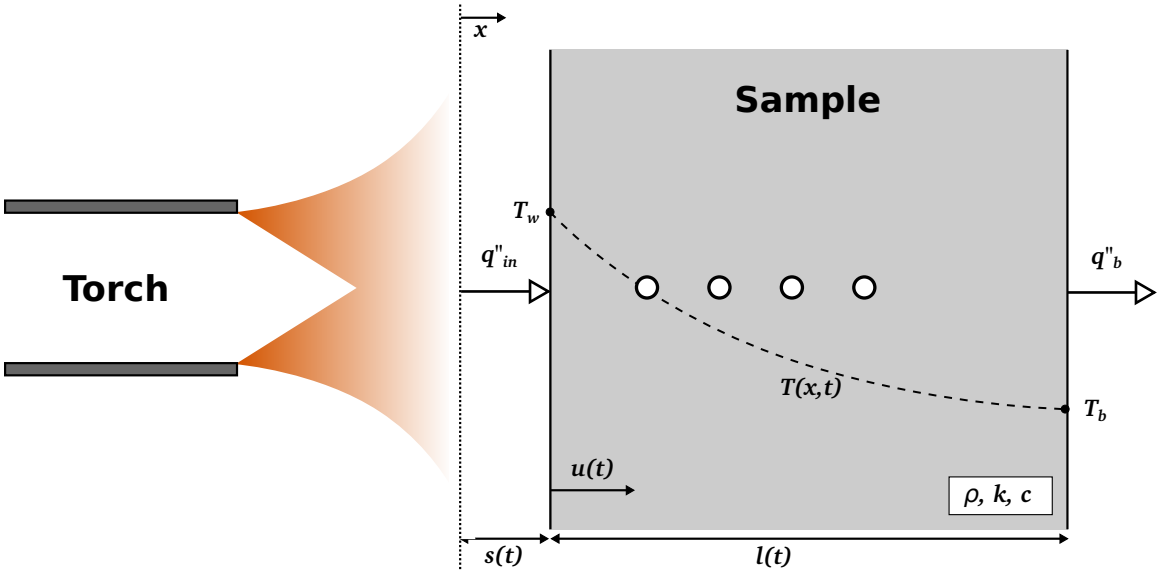

Figure 2.9: Schematic of ablating system

$$\frac{\partial T}{\partial t} - u\frac{\partial T}{\partial x} = \alpha\frac{\partial^2 T}{\partial x^2} \tag{2.1}$$

Boundary conditions are a prescribed gas temperature, heat transfer coefficient and a mass loss rate specified by an Arrhenius model at $x = 0$.

$$q''_{in} = -k\frac{\partial T}{\partial x} = h(T_\infty - T_w), \quad x = 0 \tag{2.2}$$

$$m'' = \rho u = Y_{ox} A \exp(-T_a/T), \quad x = 0 \tag{2.3}$$

The gas temperature and heat transfer coefficient are also prescribed at the back of the model.

$$q''_b = -k\frac{\partial T}{\partial x} = h_b(T_{\infty,b} - T_{w,b}), \quad x = l(t) \tag{2.4}$$

Predictions of the in-depth thermocouple responses using this model are shown below in Figure 2.10 for a scenario that is nominally the same as the experimental OTB ablation cases. The input parameters and values are listed in Table 2.2. It is assumed that there is sufficient oxygen available at the surface of the material for the reaction to occur, but in reality the oxygen concentration might change for different conditions. Note that thermocouple failure is predicted by the model once the recession process begins. A detailed comparison will be made on the ability of the forward model to predict recession rates in the Inversion Based Assessment section.

Using the forward thermal ablation model, we are able to predict the acoustical time of flight and change in time of flight for the sensor system shown in Figure 2.8. We can assume that the time of flight measurement takes place over a time period that is small relative to the time for which the spatial temperature variation evolves. As such, the time of flight measurement primarily involves a weighted spatial integration of a function of temperature.

$$\tau(t) = \int_0^{l(t)} \frac{dx}{V(T)} = \int_{T(0)}^{T(l)} (\frac{dT}{dx})^{-1} \frac{dT}{V(T)} \tag{2.5}$$

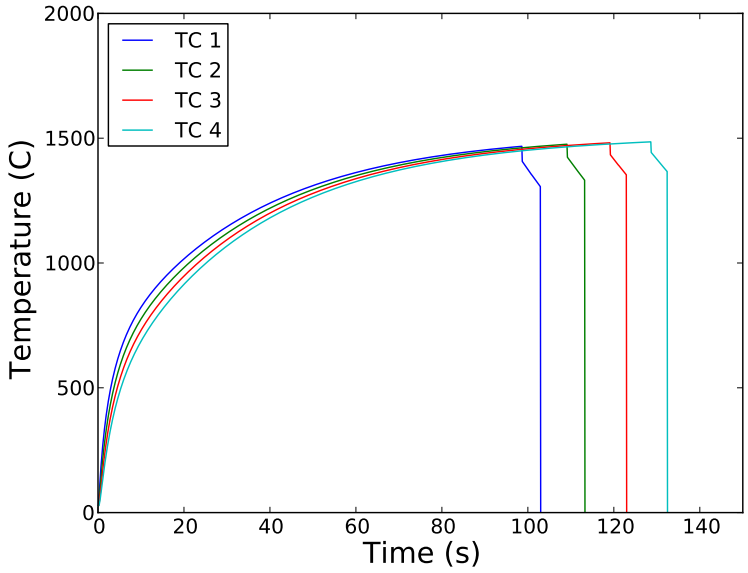

Figure 2.10: Example temperature profiles for a test with four thermocouples

Table 2.2: Example model input parameters

Parameter	Value	Units
T_∞	1800	K
h	2048	$\frac{W}{m^2 K}$
c	901	$\frac{J}{kgK}$
k	10.15	$\frac{W}{mK}$
ρ	2520	$\frac{kg}{m^3}$
$T_{\infty,b}$	473	K
h_b	50.0	$\frac{W}{m^2 K}$
A	80	$\frac{m}{s}$
T_a	25000	K
Y_{ox}	1.0	–

The change in time of flight with respect to time can be shown to be:

$$\frac{d\tau}{dt} = \frac{1}{V(T(l))}\frac{dl}{dt} - \int_{T(0)}^{T(l)} (\frac{dV}{dT})(\frac{\partial T}{\partial t})(\frac{dT}{dx})^{-1}\frac{dT}{V(T)^2} \tag{2.6}$$

$$\frac{d\tau}{dt} = \frac{1}{V(T(l))}\frac{dl}{dt} - \int_0^1 (\frac{dV}{dT})(\alpha\frac{\partial T}{\partial t})\frac{dx}{V(T)^2} \tag{2.7}$$

For these problems, $\frac{dl}{dt}$ is negative and we define it to be u. We solve for this recession velocity $u(t)$ as:

$$u(t) = -V(l)[\frac{d\tau}{dt} + \int_0^1 (\frac{dV}{dT})(\frac{\partial T}{\partial t})(\frac{dT}{dx})^{-1}\frac{dT}{V(T)^2}] \tag{2.8}$$

$$u(t) = -V(l)[\frac{d\tau}{dt} + \int_0^1 (\frac{dV}{dT})(\frac{\partial T}{\partial t})(u\frac{\partial T}{\partial x} + \alpha\frac{\partial^2 T}{\partial x^2})\frac{dT}{V(T)^2}] \tag{2.9}$$

Note that the time rate of change of time of flight ($\frac{d\tau}{dt}$) is a measured quantity using the acoustic transducer. As previously noted, a few discrete temperatures are measured and these must be used with an ablation model $T(x,t)$ and the time of flight model to generate a self-consistent temperature field and recession rate. The change in time of flight is a measure of the total energy absorbed by the sensor.

2.4 Thermal-Acoustic Inversion

As previously discussed, in the problem of interest, a high heat flux is directed towards a carbon based material at $x = 0$. Given the temperature measurements and the time of flight measurement, we seek the recession rate or equivalently, the sample length. Several approaches are reasonable. In each case, we need to construct an ablation model, $T(x,t;\vec{v},u)$, to invert for selected unknown parameters, $\vec{v}$, which are listed in Tab. 2.3.

In the first case, we seek to minimize the error, e, defined as:

$$\epsilon(\vec{v},u) = W_1\sum[Y(x_i) - T(x_i)]^2 + W_2\sum[\tau_E - \tau]^2 \tag{2.10}$$

Table 2.3: Iteration parameters

Parameter	Symbol	Units
Front (Flame) Side Temperature	T_∞	K
Flame Side Heat Transfer Coefficient	h	$\frac{W}{m^2K}$
Material Specific Heat	c	$\frac{J}{kgK}$
Material Conductivity	k	$\frac{W}{mK}$

where W_1 and W_2 are weighting constants. Between two evaluations of the error, we have a global constraint that the recession rate is related to the sample length by $u = -\frac{dl}{dt}$. Two other approaches are explored using either temperature data or time of flight data only for the error signal. We consider the minimization of the temperature error subject to a constraint on the recession velocity. This can be expressed as

$$\epsilon(\vec{v}, u) = \sum [Y(x_i) - T(x_i)]^2 \tag{2.11}$$

A similar approach can also be taken with the minimization of the time of flight error.

$$\epsilon(\vec{v}, u) = \sum [\tau_E - \tau]^2 \tag{2.12}$$

2.4.1 Serial Inversion Algorithm

The error signal is minimized by a golden section search [25] on each parameter in $\vec{v}$. The golden section search was chosen because it provides a simple method for probing a function (the error signal in this case) for the minimum value. First, the bounds and starting values are chosen for $\vec{v}$ and the algorithm starts on the first parameter by calculating the error signal at the bounds and the first and second golden points ($v_{j,1}$ and $v_{j,2}$).

$$v_{j,1} = \frac{\phi v_{j,high} + v_{j,low}}{\phi + 1} \tag{2.13}$$

$$v_{j,2} = \frac{\phi v_{j,low} + v_{j,high}}{\phi + 1} \tag{2.14}$$

If the error at $v_{j,1}$ is greater than $v_{j,2}$, then $v_{j,1}$ becomes the new bound and vice versa. Then a new golden point is calculated such that there are two bounds and two golden points and the golden point errors are compared again. This is repeated until the distance between the high and low bounds is less than 0.5% of the value of the lower bound (Fig. 2.11).

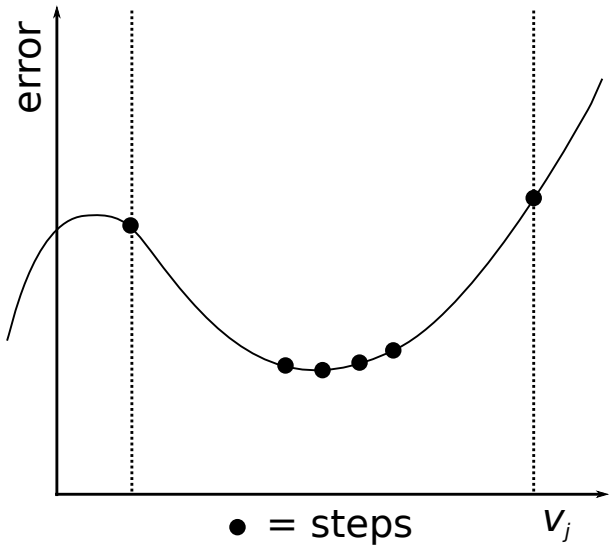

Figure 2.11: Finding the minimum error using the golden section search for a specific parameter v_j

The algorithm updates the list of parameters and moves to the next parameter in $\vec{v}$ until all parameters have been minimized. Next, the algorithm repeats this process starting at the first parameter and using the updated values. This is done

multiple times until the total change in all parameter values is less than a specified tolerance.

2.4.1.1 Serial Inversion Performance for Different Error Signals

The performance of the inversion algorithm can be tested on synthetic data generated by the forward model. This data is generated by choosing random values for each parameter within a reasonable range and collecting time history of temperatures at discrete points throughout the material and the time of flight of a signal traveling through the material. A single set of parameter values was used for all synthetic experiments to facilitate comparison between different error signals and algorithms (Tab. 2.4). The error displayed in Table 2.4 is calculated by $100 \times (v_{predicted} - v_{synth})/v_{synth}$, where a positive percentage means that the predicted value exceeded the synthetic value by that amount and likewise for negative percentages. By examining the performance of the previously mentioned error signals, we can discuss the physical significance of conditioning on each signal and gain insight on the appropriate choice for determining the recession velocity of a real system.

Table 2.4: Synthetic parameter values and percent error for three error modes with the serial algorithm.

Parameter (Units)	Synthetic Value	Temperature Error	Time of Flight Error	Combination Error
$T_\infty(K)$	2700	-46.5%	-61.4%	-48.3%
$h(W/m^2K)$	1800	0.7%	-4.0%	0.7%
$c(J/kgK)$	10	-39.7%	13.6%	-40.1%
$k(W/mK)$	1500	-44.1%	-47.1%	-45.5%

We begin by using the error of the temperature at a single point for an arbitrary duration of 150 seconds (Eqn. (2.11)). This is analogous to using the data from a single thermocouple in an OTB experiment. In Figure 2.12a, the matched temperature

(TC4) and temperature another arbitrary point (TC1) are both very close. The predicted ToF in Figure 2.12b follows the synthetic profile until the ablation process begins to take over around 100 seconds. From Table 2.4, we can see that only the original value of the front side heat transfer coefficient was captured while the other parameter values differed 39% or more from the synthetic values.

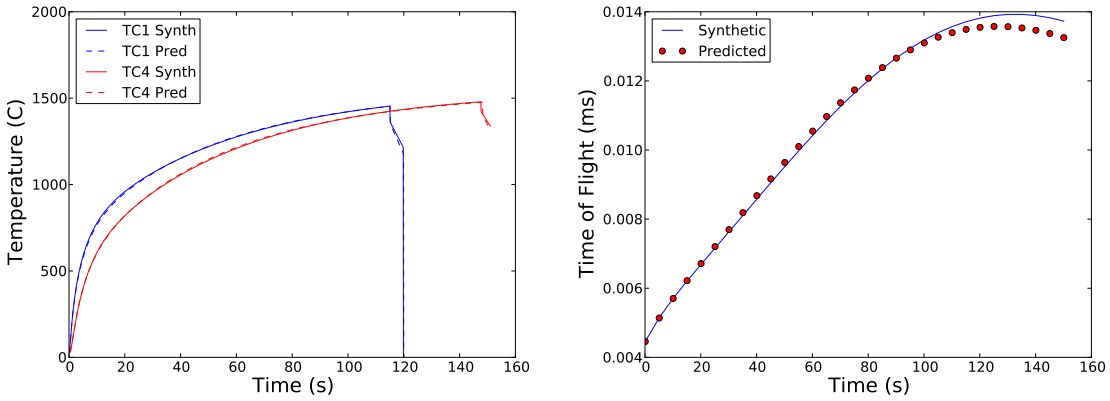

Figure 2.12: Temperature and Time of Flight for single temperature error signal.

Next, we will examine using only the error of the time of flight as represented in Eqn. (2.12). The ability to use only time of flight data would be advantageous because it provides a means for non-destructively predicting the recession rate. The time of flight is analogous to the total energy content of the material, however, it is indiscriminate of the spatial temperature profile which is visible in the poor fit in Figure 2.13a. Figure 2.13b shows good alignment with the synthetic time of flight, but under-predicts the temperature in the material.

With an understanding of the advantages and limitations of the previous error methods, the next logical step is to combine them as a weighted sum as per Eqn. (2.10). In this case, the temperature and time of flight are weighted evenly: $W_1 = W_2 = 1$. As seen in Figure 2.14a and Figure 2.14b, a better prediction is made,

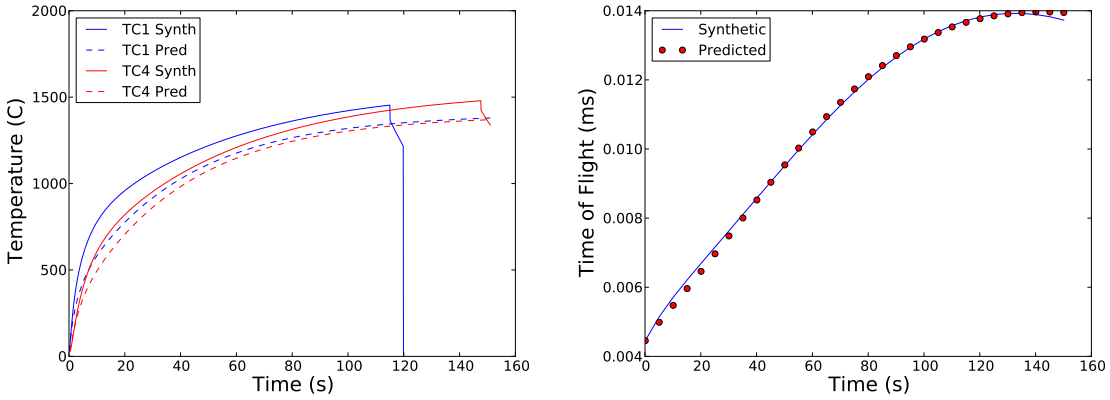

Figure 2.13: Temperature and Time of Flight for time of flight error signal.

but the spatial temperature profile is still being smeared such that the temperature at the ablating surface is predicted to be lower than the surface temperature resulting from the synthetic data, this in turn leads to under-prediction of the ablation rate.

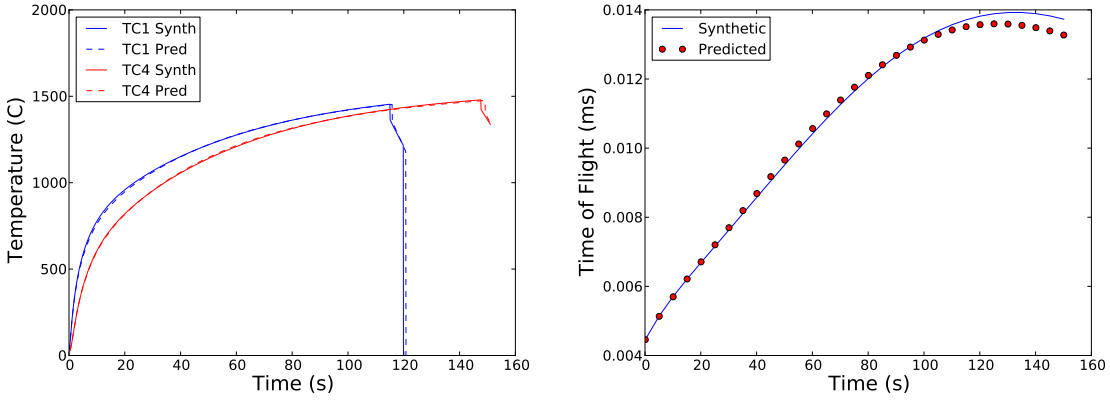

Figure 2.14: Temperature and Time of Flight for time of flight and single temperature error signal.

Looking across each of the proposed error signals, the following patterns were observed. The number of times forward thermal ablation model was called was similar for each of the error signals with the temperature error making the lowest number of

model calls at 742, and the combination and time of flight error signals making 805 and 806 calls respectively. For the golden search method, a higher number of model calls means that it took the algorithm longer to reach a minimum value. The total recession was consistently under-predicted in relation to the synthetic value, with error calculated by using the temperature profile at a single point yielding the closest prediction of 3.485 mm compared with the synthetic recession of 3.517 mm (Tab. 2.5). In the case of the time of flight only error signal, under-predicted temperatures lead to an under-predicted total ablation depth of 1.341 mm. Upon examination of the variables (Tab. 2.4), we see that only the front heat transfer coefficient was within 5% of the synthetic value in each case with the other variables differing by up to 48.3%. Despite the original values not being captured correctly, in some cases the temperature profiles are being reproduced almost exactly. This suggests that the inversion method is getting hung up in local minimum and that there are multiple combinations of input variables that can generate similar temperature and time of flight profiles.

Table 2.5: Recession.

	Total Recession
Synthetic Value	3.517 mm
Temperature Error	3.485 mm
Time of Flight Error	1.341 mm
Combination Error	3.439 mm

2.4.1.2 Serial Inversion on Experimental Data

A series of ablation tests were conducted on a carbon-carbon material in the OTB. Each test had either four or nine thermocouples embedded within the material. Additionally, the total recession was measured after each test. The ablation model described previously was coupled to the thermal measurements to predict the recession

rate. Because only temperature data was available for these experiments, the error signal was calculated as a combination of the first and last thermocouples.

$$\epsilon(\vec{v}, u) = \sum [Y(x_1) - T(x_1)]^2 + \sum [Y(x_{last}) - T(x_{last})]^2 \tag{2.15}$$

Examples of the use of the inversion model to determine the temperature profiles are shown in Figure 2.15a and Figure 2.15b. As seen in Figure 2.15a, there is a larger temperature gradient within the material than what is being predicted.

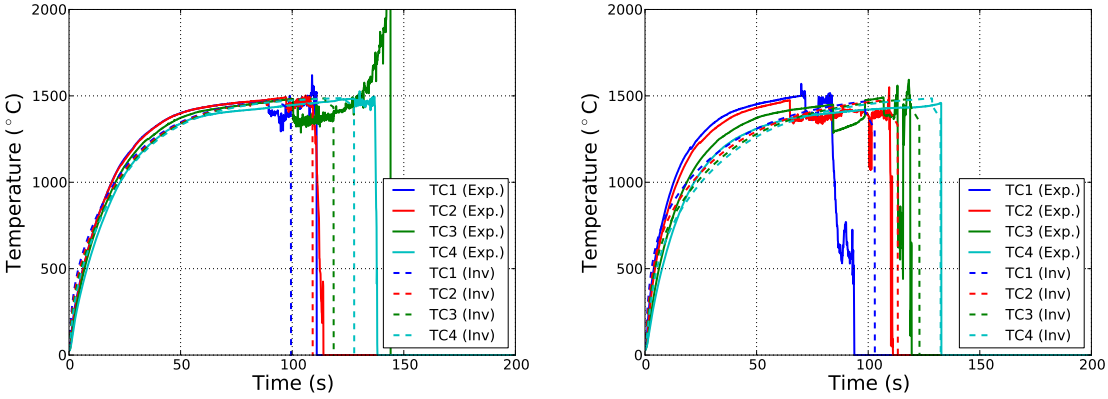

Figure 2.15: Temperature profiles for Test 1 (left) and Test 2 (right) with four thermocouples.

Out of all the four-thermocouple experiments, test one had the lowest error. For the other two tests, the serial algorithm got stuck in local minima and exited the process after one pass through the iteration variables. This equates to 120 forward model calls for test 2 and 122 forward model calls for test 3, whereas the algorithm spent longer searching for the minimum error for test one by making 822 model calls (which is on the same order as the synthetic inversion process). The result of this can be seen in Figure 2.15b where the serial inversion method performs poorly. This highlights several problems with the golden section search. This method assumes that

there is only one minimum in the search space, when in reality we do not know the shape of the space. Additionally, this method is sensitive to the initial bounds of the parameter space with no way of predicting how the model will respond to changes in the bounds. To circumvent this problem we must develop a new algorithm that can search a high dimensional parameter space for a minimum error.

2.4.2 Parallel Inversion Algorithm

The initial plan for the new algorithm was to parallelize the golden section search with Message Passing Interface (MPI) and the tridiagonal matrix solver within the finite volume model with Open Multi-Processing (OpenMP). Further research revealed that parallelization of the finite volume model would have poor speedup [26] due to the small size of the tridiagonal matrix the code is solving. A new inversion method called the iterative hypercube sampler (IHS) was developed in Python using MPI for parallelization. Compared to the golden section search, the IHS takes advantage of multiprocessing by generating more finite volume model calls in parallel resulting in much faster wall clock times by using a greater number CPU hours.

The principle behind the IHS is simple, bounds are set on the search space with a uniform probability that the parameter lies within those bounds creating a hypercube (Fig 2.16a). Each uniform distribution is binned into regions of equal probability and a random sample is drawn from each unique region in the hypercube (Fig 2.16b). This equates to M^N samples, where M is the number of bins and N is the number of parameters. The program runs the forward thermal ablation model for each sample, computes the error for the given experimental data and input parameters, and stores the error value and input parameters in a Python dictionary where each bin combination has a unique key corresponding to its location in the hypercube. Random sampling of the search space is repeated for a user defined number of iterations where

a greater number of iterations relates to better coverage of the search space. At the end of this sequence, the code finds the bin with the smallest error (Fig 2.16c) and uses the key to create bounds for a new hypercube (Fig 2.16d). Within the code this is referred to as a refinement, with the number of refinements specified by the user.

The decision to use random sampling side-steps two issues with the golden section search: sticking in local minima and dependence upon previous values. Independence of finite volume model calls lends itself to effective parallelization, limited only by the number of calls in an iteration. Most of the serial model was written in Python with the exception of the tridiagonal matrix solver which was written in Fortran. The IHS was implemented in Python using *mpi4py*, which is an MPI package for Python that is freely available on the internet.

The following sections detail the implementation of the IHS as well as the performance results from running the program on the Stampede system.

2.4.2.1 IHS Implementation

To parallelize the IHS, a master-worker system was implemented where the root processor does the random sampling of input parameter values and finds the minimum error at each iteration. The basic work flow can be seen in Figure 2.17. Several issues were considered while developing the code: how to communicate data (collective or point-to-point), how to minimize serial time on the root processor, and how to store data between iterations and refinements.

Collective scatter and gather was chosen as opposed to a dynamic point-to-point solution for communication between processors. There are three motivating factors behind this decision. First, each finite volume call takes about the same amount of time ($\sim$5.7 seconds on a 2.7 GHz processor), so creating a dynamic solution

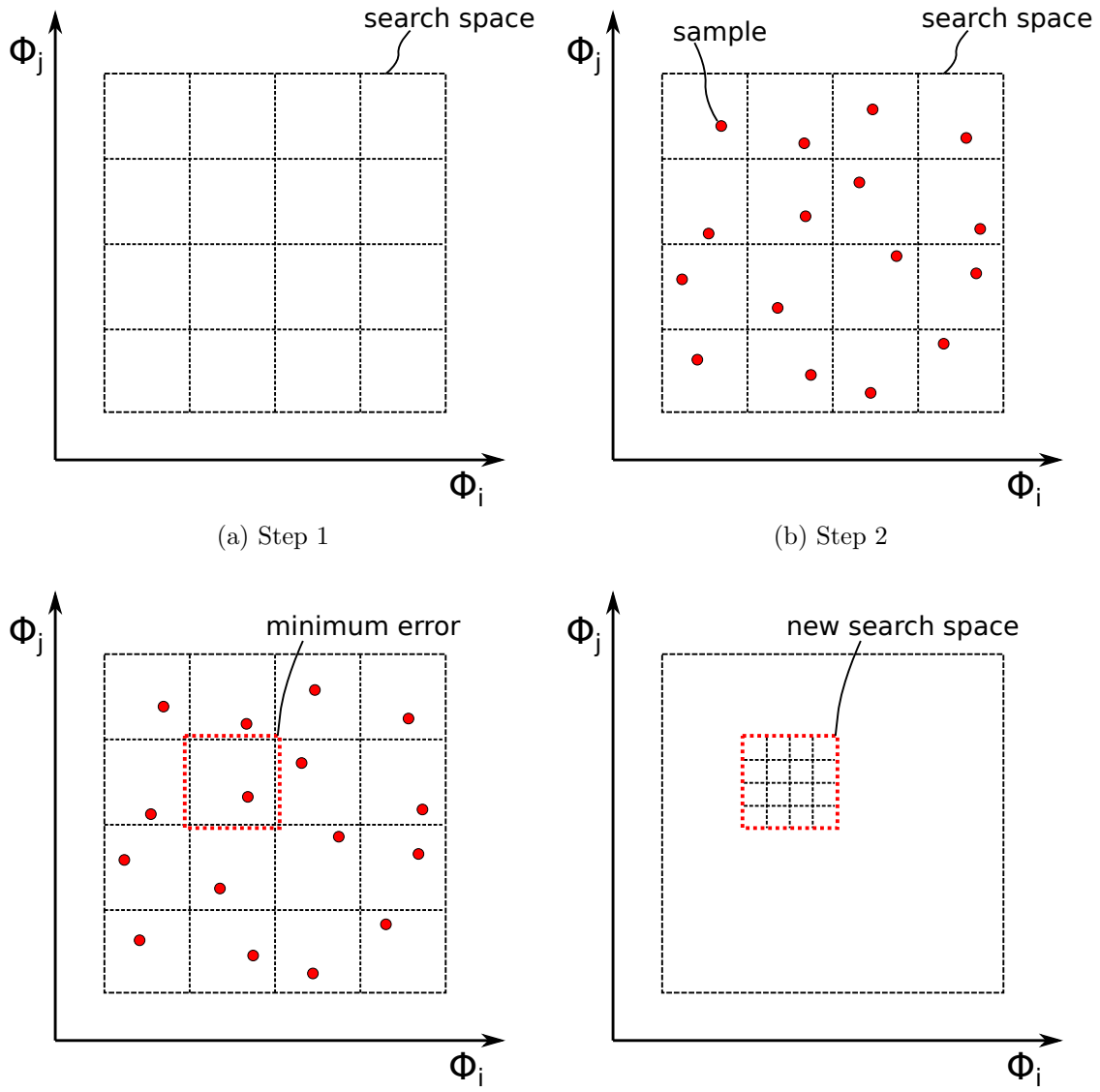

(a) Step 1

(b) Step 2

(c) Step 3

(d) Step 4

Figure 2.16: Basic operation of the Iterative Hypercube Sampler (IHS): a search space is defined in step 1, samples are drawn in step 2 and repeated for a set number of iterations, the minimum error is found in step 3, and a new search space is defined (refinement) in step 4.

would provide little improvement. Also, using collective communications scales better when distributing information to increasingly larger numbers of cores. Finally, the amount of time spent by the root processor doing serial calculations is very small

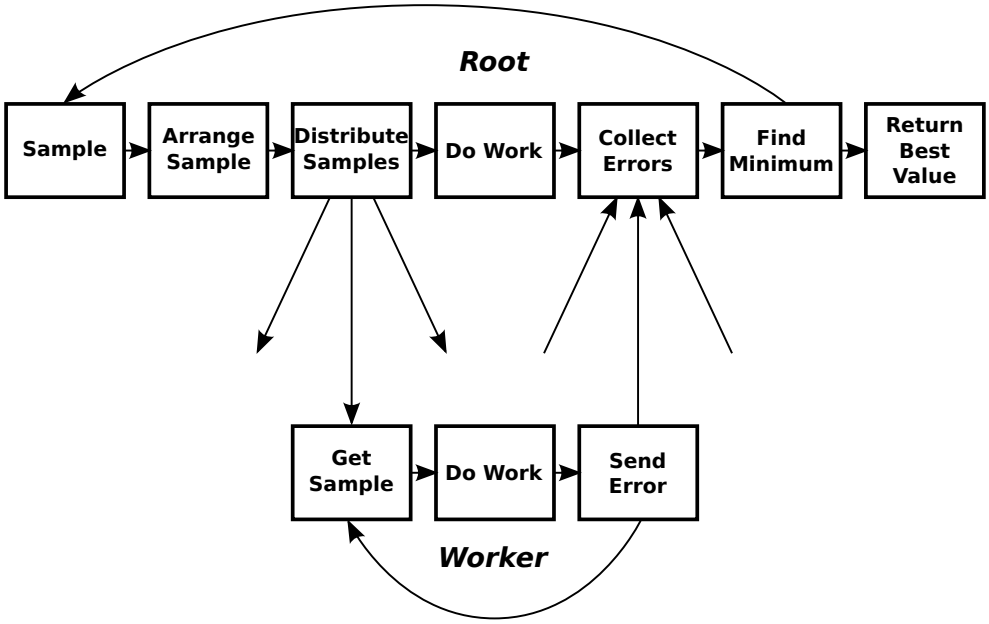

Figure 2.17: Workflow of IHS code

compared to one finite volume model call. The code for the communication process on the root processor can be seen in Appendix A.1.

Between the scatter and gather communications, there is a finite volume call. Because the code uses blocking communications and the serial processes take much less time than the finite volume model, the root node was made a worker processor between rounds of communication. The implementation of the worker processes is similar to the root with the exception of a few *if* statements that allow the workers to exit the *while* loop of waiting for work. This is accomplished by sending placeholder text to the processors that do not receive work at the end of an iteration and sending *None* when all iterations are complete (Appendix A.2).

Finally, a few comments on the serial sections and data storage are necessary to complete the discussion of the code implementation. Python dictionaries simpli-

fied data storage between iterations and refinements. Dictionaries are lists of items that are indexed by keys as opposed to a fixed numerical sequence. In the IHS there are three main dictionaries: the argument dictionary, error dictionary and minimum dictionary. The argument and error dictionaries are iteration specific, while the minimum dictionary persists between iterations. The minimum dictionary's keys take the form XXXXXX_XX, where the first six digits represent the location of the sub-hypercube from which the sample was drawn, and the final two digits are the iteration and refinement numbers. The lists corresponding to each key contain the error value and the sampled parameter values. Decomposing this key allows the minimum to be easily tracked between iterations, and new hypercube dimensions to be calculated at each refinement. At the end of execution, the code returns a key and parameter pair corresponding to the lowest error. Post-processing scripts can then run the finite volume model with these values and generates plots to be compared to the experiments and synthetic data.

2.4.2.2 Performance

To analyze the performance of the parallel IHS code, the number of bins (M) was set at three with five iterations per hypercube and one refinement resulting in ten iterations total. The number of input parameters (N) for the finite volume model is set to six (including the back heat transfer coefficient and gas temperature). This equates to 729 model calls per iteration for a grand total of 7290 model calls. First, the temperature output predicted by the finite volume model was checked after one parallel run to verify that the error was being minimized. Improving the accuracy of the thermal finite volume model is the subject of ongoing research, however, this is an improvement on the results from the golden section search. Additionally, increasing the number of iterations and refinements will increase accuracy to an extent. To

complete a timely performance analysis, values for the number of iterations and refinements were chosen that resulted in a serial time of under 12 hours. The following parallel performance analysis will aid in determining the optimal number of cores to use in future research.

To measure the scaling performance of the code and calculate speedup and efficiency, timers were inserted into the code to measure total run time, time spent by the root processor doing serial tasks, and communication time (Table 2.6). The percentage of time spent by the root processor doing serial calculations, such as finding minima or sampling new parameters is less than 0.5% of the total time in each case, indicating that the use of scatter and gather is appropriate for communications. Each time value decreases as processor number increases because the number of communication calls decreases as the size of the communicator increases. However, there are a few anomalies that are better explained by tracking the speedup and efficiency.

Table 2.6: Timing for IHS code (Serial time = 11.8 hours)

# of Procs	Total Time (m)	Root Serial Time (s)	Communication Time (s)
16	46.4	1.98	183.3
32	24.0	1.23	106.1
64	13.1	0.80	29.64
128	6.5	0.55	30.08
256	3.3	0.43	27.74
368	2.2	0.39	11.50
512	2.3	0.40	11.46
640	2.2	0.40	15.86
736	1.2	0.36	6.01

Figure 2.18 shows the speedup of the IHS code for the previously described conditions. The code scales well up to 368 cores after which it begins to diverge from the ideal considerably. We know that the code will not scale above M^N processors, 729 in this case, because this is the number of tasks per iteration and the code will

not loop back and start a new iteration until the current one is complete. When the number of processors exceeds 729 the speedup moves back towards ideal, however any processors requested beyond this point will sit idle during execution and the speedup will flat-line.

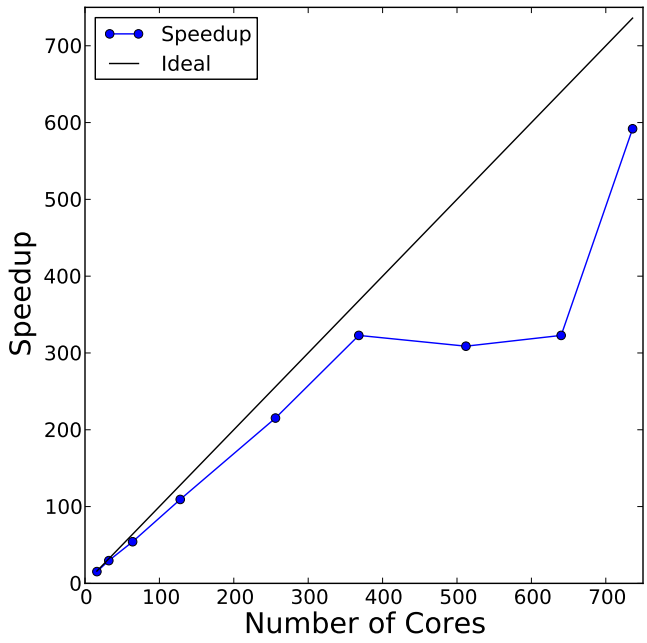

Figure 2.18: Speedup for M^N=729

To better understand this behavior, we examine the efficiency listed in Table 2.7. To demonstrate the dependence of scaling on M^N, Table 2.7 also lists the number of idle processors in the last work sequence of each iteration. This is calculated by $P - (M^N \% P)$, where P is the number of processors in the communicator. As expected, minimizing this number leads to higher efficiency.

Ultimately, the parallel implementation of this code works well when the user makes the appropriate choice for the number of cores. Based on the scaling analysis, this number is $\frac{M^N}{2}$ rounded up to the nearest multiple of cores per node. This

Table 2.7: Efficiency and idle processors during the last scatter/gather of each iteration

# of Procs	Efficiency	Idle Procs
16	0.95	7
32	0.92	7
64	0.84	39
128	0.85	39
256	0.84	39
368	0.88	7
512	0.60	295
640	0.50	551
736	0.80	7

choice presents the best balance between efficiency and total run time. The parallel components of this code could be further improved by removing the barrier between iterations or creating a dynamic solution that skips high error valued sub-hypercubes in the proceeding iterations. The number of iterations could also be increased on early refinements where covering a large search space is of higher importance.

2.4.3 Comparison of IHS and Serial Inversion on Synthetic and Experimental Data

The IHS was run on synthetic and experimental data using the same synthetic input parameters and error modes as the serial algorithm. The number of bins was chosen to be five, which equates to 625 forward model calls per iteration. The number of refinements was set at two which produces a hypercube whose bounds are 0.8% of their original value. This was chosen to be similar to the exit criteria for the serial model which stops when the input parameters are changing by less than 1% between passes. The result is 9,375 forward model calls per IHS simulation, whereas the serial algorithm reaches a minimum within 900 forward model calls. In this configuration, the IHS consumes about ten times as many CPU hours (number of cores times wall

clock time) as the serial method, but it can be run in a shorter wall clock time with the proper number of cores.

Table 2.8 shows the relative error when inverting for synthetic parameters. All predicted values were within 20% of the synthetic values with an average difference of 9.9%, compared to the serial method where the highest error was 61.4% with an average of 32.6%. Due to the stochastic nature of the IHS, these values will be different for each simulation.

Table 2.8: Synthetic parameter values and percent error for three error modes with the IHS algorithm.

Parameter (Units)	Synthetic Value	Temperature Error	Time of Flight Error	Combination Error
$T_\infty(K)$	2700	16.0%	12.4%	19.4%
$h(W/m^2K)$	1800	-0.2%	1.1%	-0.4%
$c(J/kgK)$	10	10.8%	8.4%	8.7%
$k(W/mK)$	1500	14.0%	14.2%	13.5%

When comparing the parameter errors between each error mode, the time of flight error signal appears to perform slightly better than the other two error signals. However, if we examine the total predicted recession in Table 2.9, we can see that the temperature only error signal performs the best with a difference of 0.003 mm from the synthetic value. The combination signal also performs well with a difference of 0.007 mm. The temperature and time of flight profiles for these two error signals are displayed in Figure 2.19 which, upon visual inspection, supports the level of accuracy presented by Tables 2.8 and 2.9 as the profiles for the two error signals appear to be almost identical.

To gain more insight to performance of the time of flight only error signal, we can view the temperature and time of flight profiles in Figures 2.20a and 2.20b. Unlike the serial method each of the error modes performed similarly, but in the case

Table 2.9: Recession.

	Total Recession
Synthetic Value	3.517 mm
Temperature Error	3.520 mm
Time of Flight Error	4.046 mm
Combination Error	3.510 mm

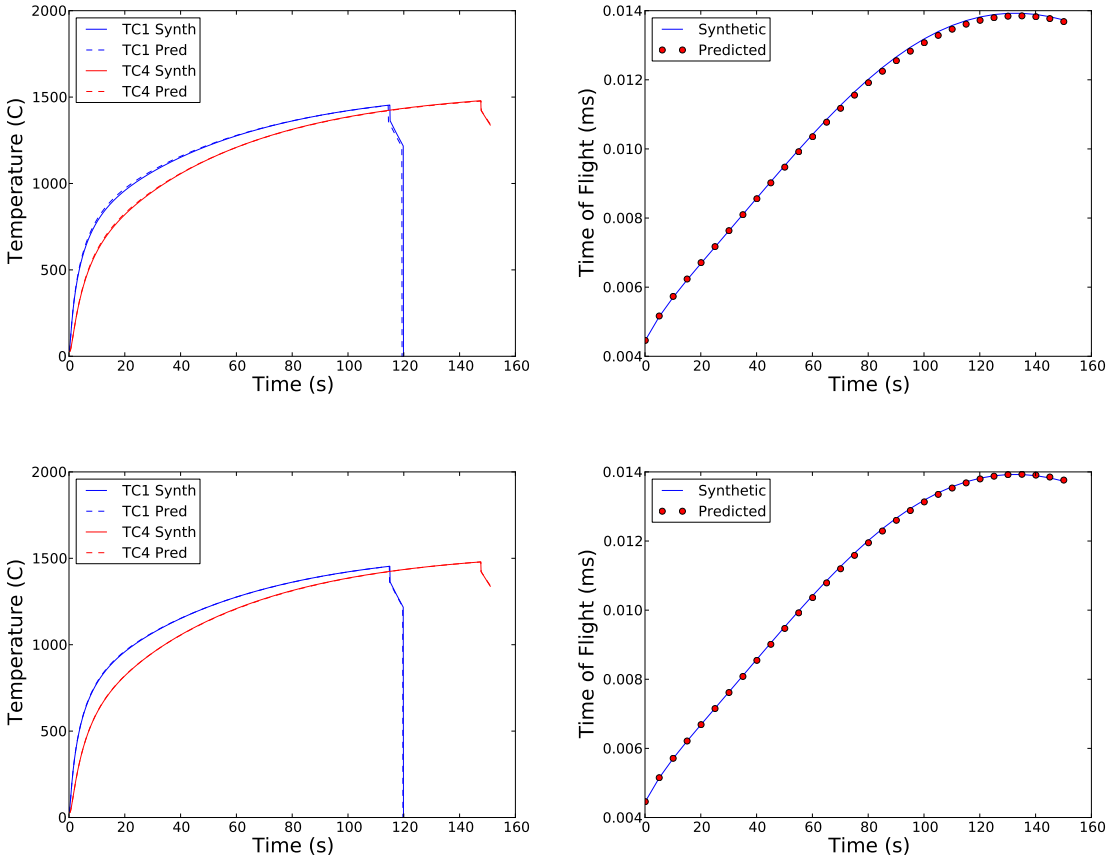

Figure 2.19: Temperature and Time of Flight for IHS inversion with a combination error signal (top) and temperature only error signal (bottom).

of the time of flight error signal the predicted temperatures were slightly higher than the synthetic data. The result is a higher surface temperature, and therefore higher ablation rate and total recession distance (Tab 2.9).

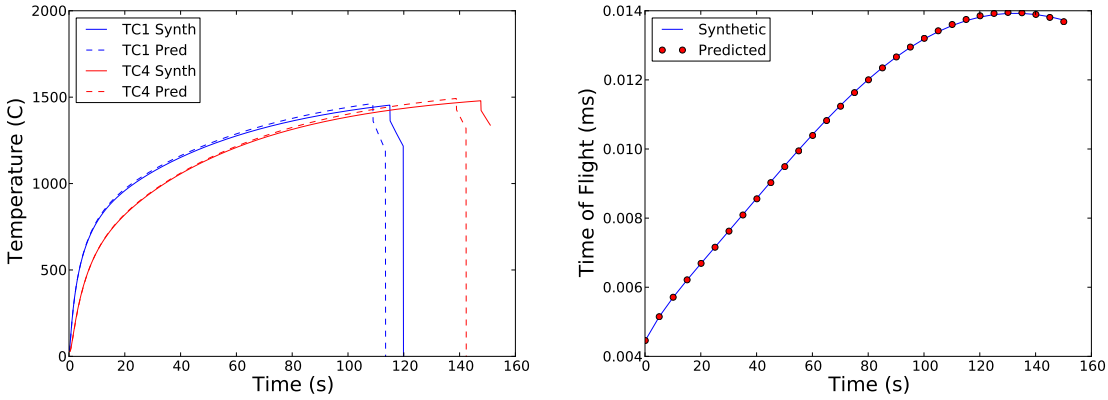

Figure 2.20: Temperature and Time of Flight for IHS inversion with a time of flight error signal.

In the IHS, the same two point temperature error was used to invert for experimental data. Overall, the total error from the IHS was lower than the serial error (Tab. 2.10).

Table 2.10: Comparison of error inverting for experimental data with the serial and IHS algorithms.

Test Number	Serial Error	IHS Error
1	3.9×10^6	2.8×10^6
2	17.4×10^6	10.6×10^6
3	61.8×10^6	10.7×10^6

However, by examining the experimental temperatures versus those predicted by the model, we can see that the profile was not predicted correctly. The difference between the first and last points (TC1 and TC4) around 50 seconds is on the order of 100^oC in the experiment and 10^oC in the model predictions for test number three (Fig 2.21a). The temperature profiles predicted by the model collapsed on each other in each of the experiments. To determine if this was a function of using two points for the error signal, the IHS was re-run with only TC4 as the error signal as

this performed the best when inverting for synthetic data. However, the predicted temperature profiles all collapsed on the experimental TC4.

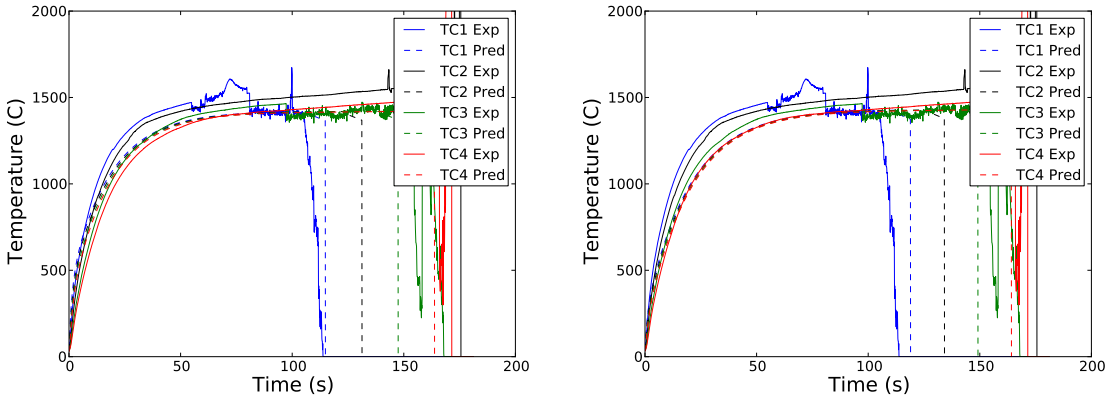

Figure 2.21: Experimental and IHS predicted temperature profiles for Test 3 with two point error (left) and one point error (right).

A major goal of the ablation experiments was to predict the recession rate of the sample. Preliminary analysis was done to calculate the average recession rate using two methods. The first involved measuring the total recession distance after the test and dividing by the test duration. For the second method, a "break temperature" was prescribed and the average recession was determined by fitting a trend line through the thermocouple break points, the results of which were shown in Figure 2.6 and Table 2.1. The forward thermal ablation model allows for calculation of the recession rate as a function of time as shown in Figure 2.22. The transient heating stage is reflected in the recession rate and can be seen from the beginning of heating until around 100 seconds in each test. Beyond this point, the recession rate approaches a steady value that is consistently higher than the average manual recession rate.

Further insight into the performance of the model can be gained by comparing the predicted and experimental total recession distance as shown in Table 2.11. The IHS underpredicted the total recession by 1.08 mm, 0.58 mm, and 0.60 mm for each

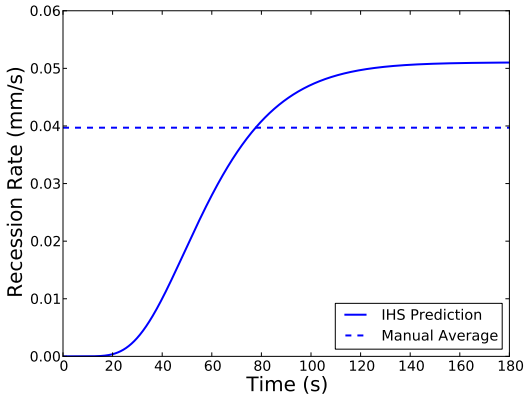

(a) Test 1

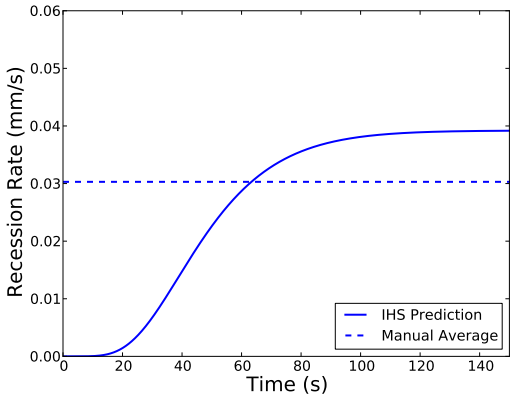

(b) Test 2

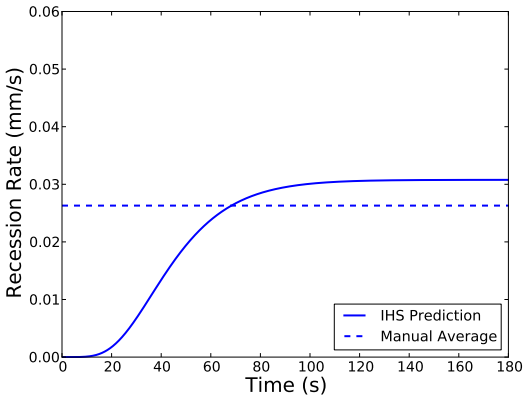

(c) Test 3

Figure 2.22: Recession rate time history predicted by the IHS and manual recession rate for tests 1-3.

respective case. This could be due to the underprediction of the magnitude of the hot face surface temperature during the beginning portion of the tests which would result in a lower recession rate. Possible solutions to this problem include inverting for the Arrhenius parameters or developing a more robust representation of the ablation kinetics.

These results suggest that further improvements will need to be made to the forward model. There are several paths open for future work, a few of which are

Table 2.11: Total recession for the tests 1-3 compared to IHS predicted total recession.

Test Number	Total Experimental Recession (mm)	Total IHS Recession (mm)
1	7.14	6.06
2	4.55	3.97
3	4.73	4.13

presented as follows. A more detailed physical representation of the ablation process and/or the thermocouples used to record experimental temperatures could be added to the forward model. Another approach would be to expand the number of input parameters in the search space to include the Arrhenius activation energy term and pre-exponential coefficient.

2.5 Conclusions

A one-dimensional finite volume heat transfer model was created that could generate the time history of the temperature and acoustic time of flight in an ablating material. An experimental system was designed for thermal and acoustic measurements. This system was then tested and a series of ablation experiments were carried out. A golden section search method that inverts for the ablation rate was then developed using the forward heat transfer model as a predictor. Several error modes were tested within the golden section method using synthetic data. The method was then run on the experimental thermal data and it was found to have several shortcomings; namely the dependence on previous values and propensity to get caught in local minima. To solve these issues, a new inversion method (IHS) was developed that can run in parallel. This method was found to be more accurate when inverting for synthetic and experimental data. Future work can be done on the forward heat transfer model to improve the representation of physics in the ablation process. An

improved forward model coupled with the IHS could lead to a relatively quick and accurate method for predicting the ablation rate of a material.

Chapter 3

Void Space Ignition

3.1 Void Space Ignition Overview

The work in this section builds upon compartment scale experiments conducted by the University of Texas at Austin Fire Research Group (UTFRG). An overview of these experiments is included in this thesis to provide motivation for the void space ignition modeling and experiments. This section begins with a description of the compartment scale experiments and discussion of the results. This transitions into the development of a theory for understanding the void space ignition observed at the compartment scale and leads to the development of a void leakage scale experimental system used to conduct a set of ignition experiments.

3.2 Compartment-Scale Experimental System and Characterization

Experiments were conducted in a structure consisting of a single room and an entrance hallway, as shown in Figure 3.1. The ceiling is 2.44 m in height everywhere except within the void space, which is 3.05 m tall and open at the top. The experimental structure is 5.82 m in length, 4.78 m wide, and the hallway partition is located 1.42 m from the right wall. The hallway is 2.24 m long and 1.42 m in width. The hallway partition is located 0.10 m from the doorway.

The test section was constructed with 1.6 cm thick gypsum board fastened to 0.10 m wide studs that are 3.05 m tall (Fig. 3.2b). To approximate leakage paths

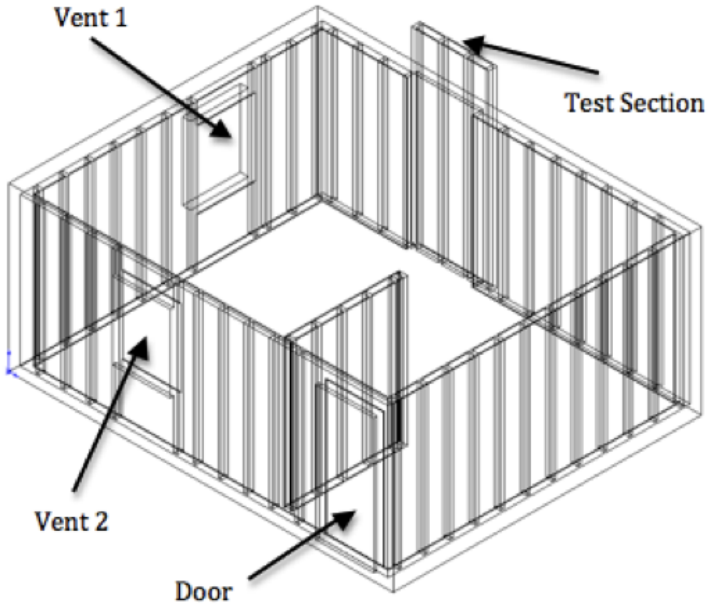

Figure 3.1: Geometry of the burn structure at The University of Texas at Austin.

from the interior compartments to the wall spaces, two types of gypsum failure areas were created in the experimental system: a large square cross-section hole of 6 cm x 6 cm and a smaller area of 1 cm x 2 cm. The primary gypsum failure area is the square cross-section hole (6 cm by 6 cm) in the gypsum board of a wall in the fire room at an elevation of 1.2 m (Fig. 3.2a). This hole exposes a void space (between the wall studs) to the main room. Two different types of electrical panels (either light switches or electrical plugs) were inserted into the primary failure area to simulate potential failure paths for fire to penetrate from the room into the void space. A much smaller failure area of approximately 2.0 cm^2, that might be associated with a penetration resulting from remodeling etc., was placed at a height of 2.14 m. It is of interest to understand what type of breach in a room's protective gypsum wall coverage promotes void space ignition and whether firefighter use of PPV increases the chance of this ignition process.

In these experiments, the void space is designed to resemble structural void

Figure 3.2: Mid-elevation failure location front view (left) and test section rear view (right).

spaces in balloon frame construction, which represents a worst-case structural failure system for a pressurized fire compartment. The gypsum failure areas were placed through the interior gypsum wallboard of the void space to expose the void space to the main room. The studs within the void space are separated by 0.41 m, and the full dimensions of the void space were 0.10 m by 0.41 m by 3.05 m. Fiberglass insulation was inserted in the void spaces between the studs to more realistically model a typical wall assembly.

3.2.1 Experimental burners and HRR

Two 30 cm (12 in) by 30 cm (12 in) by 20 cm (8 in) sand burners fueled with propane were used as the burner system for the compartment. The sand burner design was based on ASTM E 2257, a standard for room fire tests [27]. A rotameter was installed in-line between the propane source tank and sand burners to regulate the fuel flow rate. The HRR is found by multiplying the fuel mass flow rate by the heat of combustion of the fuel (43.7 kJ/g). The burners were found to have a critical mass

flow rate, above which point the gas would fluidize the sand instead of percolating through it. This critical flow rate is equivalent to HRRs of 250 kW. Therefore, for safety reasons, experimental HRRs were limited to 200 kW per burner.

3.2.2 Fan specification

For tests in which a positive pressure fan was used, the experiments used a 4.85 kW (6.5 hp) motor, commercial PPV fan to generate the airflow. The fan has a diameter of 0.61 m and was operated at full throttle. It was rated to produce 13.12 m^3/s when operated at 3,500 rpm. The fan was set 2.44 m from the door based on literature recommendations for best effectiveness [14, 28]. A distance of 2.44 m was chosen as it falls in the middle of the recommended range. The fan height was adjustable and was set at a centerline height of 0.71 m (the height of the fan with legs extended) so that the jet of air produced best sealed the doorway.

3.2.3 Experimental conditions

For all experimental cases, the fire burned in an initially closed compartment for approximately 5 minutes and then was ventilated. PPV flow experiments were performed for three venting configurations: Scenario 1) door open, window open, fan inactive (natural ventilation), Scenario 2) door opened, window open, fan active (proper PPV), and Scenario 3) door open, window closed, fan active (improper PPV). The maximum pressurization occurred for the case in which the windows were closed (approximately 50 Pa). This is called improper PPV and represents a worst-case scenario with respect to the ventilation process and "pushes" the fire into the void space. Since leakage can significantly affect conditions during the application of PPV [17], the experimental structure leakage was determined according to the blower-door test as described by ASHRAE Standard 119 [29]. For this test, an impermeable membrane

is sealed across the doorway and around the outside shroud of a fan that is located in the doorway, blowing out of the compartment. The flow rate produced by the fan and the resulting compartment pressure were recorded and a standard method was used to characterize the leakage using these data. The method produces an effective leakage area (ELA), which corresponds to the actual leakage area present in a structure and a normalized leakage value (NL), which can be used to compare the leakage of one structure to others. The leakage test was conducted and the ELA and NL values obtained were 0.029 m^2, and 1.02, respectively. Sherman and Dickerhoff [30] provide an average normalized leakage for a residential structure to be 1.72 with a standard deviation of 0.84. The leakage in the experimental structure is within one standard deviation of average residential houses.

Bi-directional probes were used to measure the velocities produced during the cold flow experiments. These probes, as first described by McCaffrey, can be used to determine the incident flow velocity by measuring the differential pressure established across the probe [31]. Each probe used in the experiments was connected to a differential pressure transducer (Setra Model 264).

Flow through the structure was measured by placing three probes in the doorway, four probes in the windows (when applicable), and three probes near the top of the void space. The probes in the door were spaced at 0.61 m, 1.22 m, and 1.83 m elevation along the doorway centerline. The four probes in the window were spaced evenly, effectively dividing the window into quadrants. Finally, the probes in the void space were located at an elevation of 2.75 m and evenly spaced across the 0.41 m test section. All of the probes were oriented to measure velocity normal to each of the associated vents.

Additional instrumentation included 32 thermocouples to measure tempera-

ture at four elevations over eight spatial locations. Thermocouple trees are fixed at eight distinct spatial locations. Figure 3.3 shows the location of each of the thermocouple trees as well as the location for the burners.

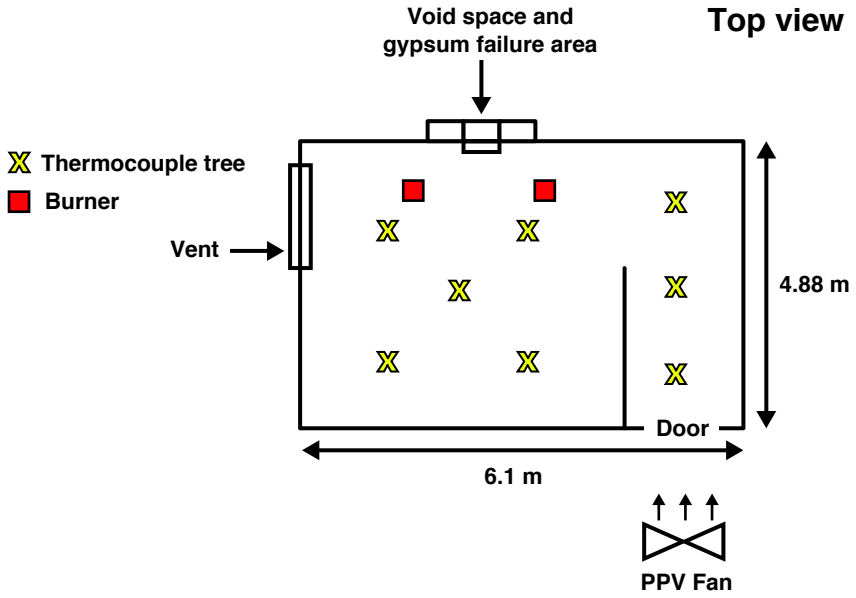

Figure 3.3: Plan view of burn structure showing burner and thermocouple locations.

3.3 Computational Fluid Dynamics Model Setup

The computational fluid dynamics model, Fire Dynamics Simulator (FDS) version 6.0 (SVN revision 13186), was used in this study to model the UT Austin burn structure and characterize the effects of PPV on the thermal and flow conditions in the structure. Fire Dynamics Simulator is a computational fluid dynamics model that numerically solves a form of the Navier-Stokes equations appropriate for low-speed, thermally-driven flow with an emphasis on smoke and heat transport from fires McGrattan et al. [32]. The computational domain had dimensions of 9.6 m by 9.6 m by 3.2 m. The burn structure dimensions were the same as the experimental setup shown in Figure 3.3. The grid cells were 15 cm on all sides. The fire was set

to be 400 kW using two burners each with a specified HRR of 200 kW. The fuel was propane. The walls had properties of gypsum board; a thickness of 0.016 m (5/8 in), thermal conductivity of 0.48 W/m-K, specific heat of 0.84 kJ/kg-K, and density of 1440 kg/m^3. The PPV fan was set up as an HVAC device with an inlet, outlet, and specified volume flow rate. A tangential fan velocity component was used as detailed in a previous study by Weinschenk et al. [19].

The instrument in the FDS scenario included thermocouples, velocity probes, and a pressure gage to match the instrumentation in the experiments. An additional nine pressure sensors were located 0.25 m away from the GFA and were used to measure the pressure over the height of the compartment during various ventilation scenarios. The pressure sensors were located between the two burners at heights of 0.3 m, 0.6 m, 0.9 m, 1.2 m, 1.5 m, 1.8 m, 2.1 m, and 2.3 m.

3.4 Experimental and Computational Results

3.4.1 Temperature measurements

Temperature measurements are shown in Figure 3.4 at various elevations within the compartment for several thermocouple trees. Thermal stratification is clearly seen for this 150 kW fire case when no fan pressurization is applied (i.e., natural ventilation).

In the interior of the compartment there was relatively little effect of improper PPV on temperatures within the compartment. This was evident for both low and high HRRs. Figure 3.5 shows the interior compartment temperatures for 150 kW fire conditions. Figure 3.6 shows that the same types of temperature profiles exist for a 400 kW fire. These temperatures correspond to a thermocouple tree located in the center of the fire room. Note that the peak temperatures at the highest elevations of

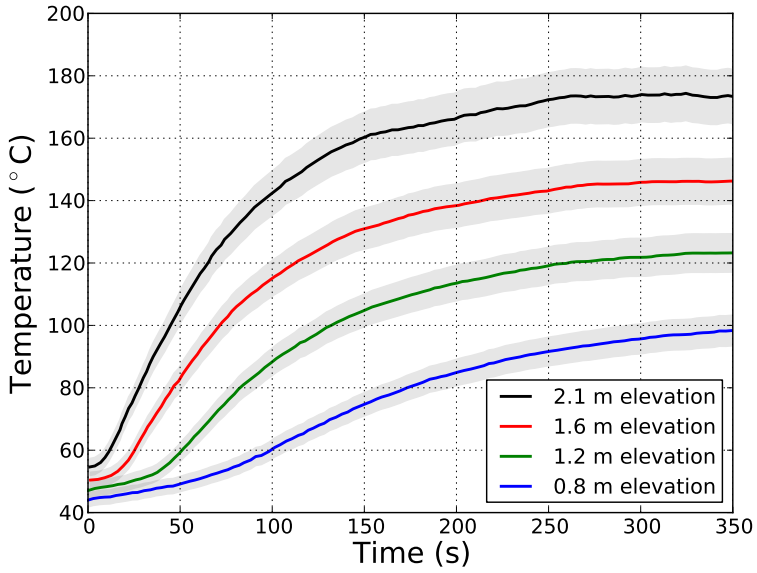

Figure 3.4: Temperature profiles at several thermocouple trees and various elevations.

the fire room reach 300 C for the 400 kW fire test.

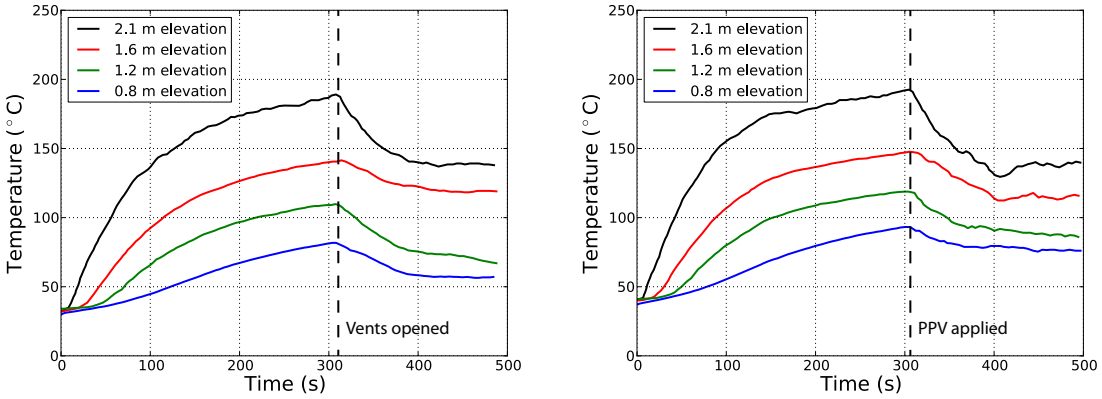

Figure 3.5: Natural ventilation (left) and improper PPV (right) for 150 kW fire cases.

The highest temperatures occur at the highest elevations in the compartment prior either naturally venting the compartment or applying PPV. Note that after ventilation, either naturally or by PPV, temperatures decrease at all elevations. How-

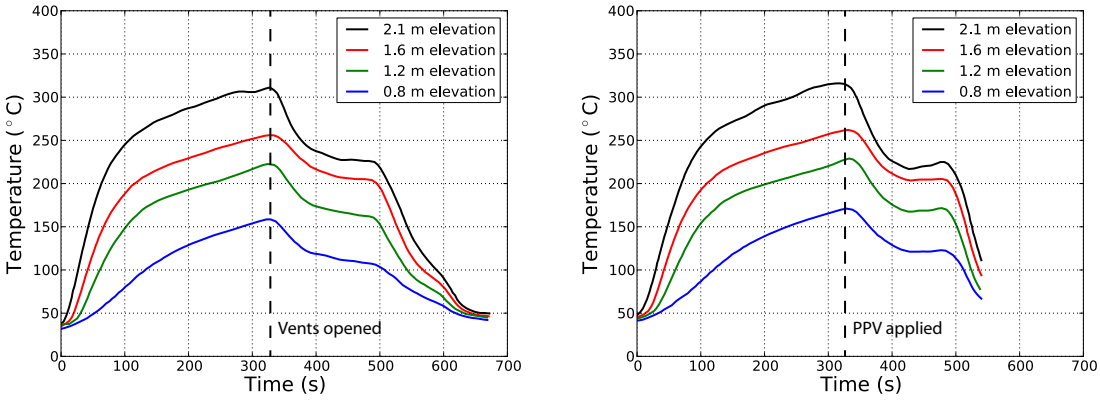

Figure 3.6: Natural ventilation (left) and improper PPV (right) for 400 kW fire cases.

ever, for the improper PPV cases, the lower elevation temperatures do not decrease as much as the natural ventilation cases. This suggests that there is more mixing with improper PPV. The effects on void ignition of the initial thermal stratification and subsequent cooling after ventilation will be discussed in a later section.

3.4.2 Pressure predictions

Computational model predictions of the temperature field agree reasonably well with experimental observations. We were unable to generate detailed pressure profiles through the experiments and thus rely on the computational fluid dynamics for pressure versus elevation predictions under the different ventilation scenarios.

For the case with natural ventilation (Scenario 1), the door and window were opened at the time of ventilation. For the case with proper PPV, the door and window were opened and fan activated at the time of ventilation. For the case with improper PPV, the door was opened and the fan activated at the time of ventilation. These events were controlled via timers in FDS that were set to activate at a time of approximately 5 minutes after the burners were ignited in the computations.

The resulting pressure profiles as a function of time are shown in Figures 3.7a to 3.7c. For the natural ventilation scenario (Fig. 3.7a), the pressure rise near the ceiling is about 7 Pa at 200 s after which the compartment fire becomes under-ventilated. After ventilation occurs, the ceiling pressure becomes steady between 5 Pa to 6 Pa. For the proper PPV ventilation scenario, the pressure rise at the ceiling is between 20 Pa and 30 Pa. For the improper PPV ventilation scenario (Fig. 3.7c), the pressure rise at the ceiling is between 60 Pa and 80 Pa.

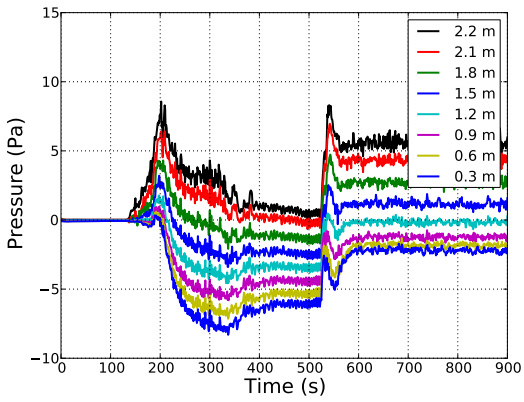

(a) Natural ventilation

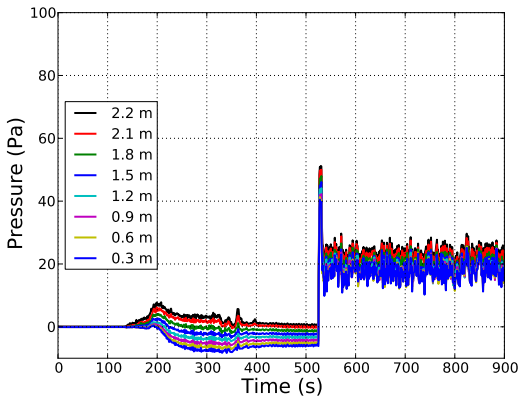

(b) Proper PPV

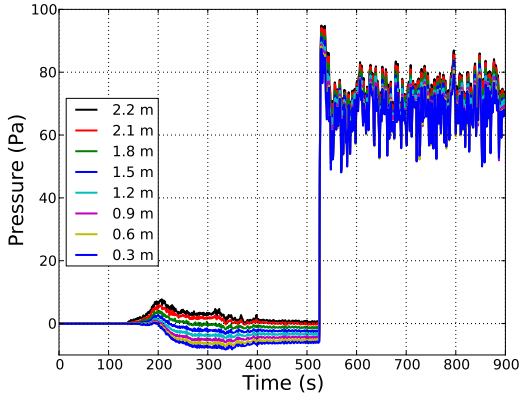

(c) Improper PPV

Figure 3.7: Pressure profiles for (a) natural ventilation (b) proper PPV and (c) improper PPV.

For the PPV cases, after PPV is applied, the differences in pressure between all the elevations are small relative to the lowest pressure in the compartment (i.e., the pressure at the floor). As a first order approximation, the compartment pressure can be assumed to be constant once PPV takes place. This is in contrast to the natural ventilation case for which a hydrostatic pressure difference is present and would create different flow directions across a void depending on the void elevation.

3.4.3 Thermal penetration

A large leakage path was placed into the wall void space to have a well-controlled failure region on the gypsum wall of the burn structure. This gypsum failure area (GFA) was located at an elevation of approximately 1.2 m above the floor. Temperature measurements were made at the GFA and also immediately behind it in the void space (cf. Figs. 3.2a and 3.2b). We investigated fire penetration into electrical boxes and the effects of failure elevation on fire penetration.

We performed a series of experiments to investigate the heat flux and extent of damage to these electrical outlets and switches. Figure 3.8a shows the mounting of an electrical outlet at the mid-wall height prior to the fire being set in the compartment and then representative outlets and a switch in Figure 3.8b after the fire. Typical heat flux measurements for a case where 150 kW fire is below an outlet are on the order of 10 kW/m^2. There was no fire penetration into the wall at the 1.2 m elevation.

The lack of interior damage under these mid-height outlet conditions led us to consider higher elevation failure. Our hypothesis was that if the gases entering the wall void are sufficiently hot at higher elevations, then these gases might induce smoldering reactions within the void. It was anticipated that once the flammable mass inside the wall ignites in a smoldering reaction (where low oxygen combustion can occur) this smoldering process could persist over relative long time durations without

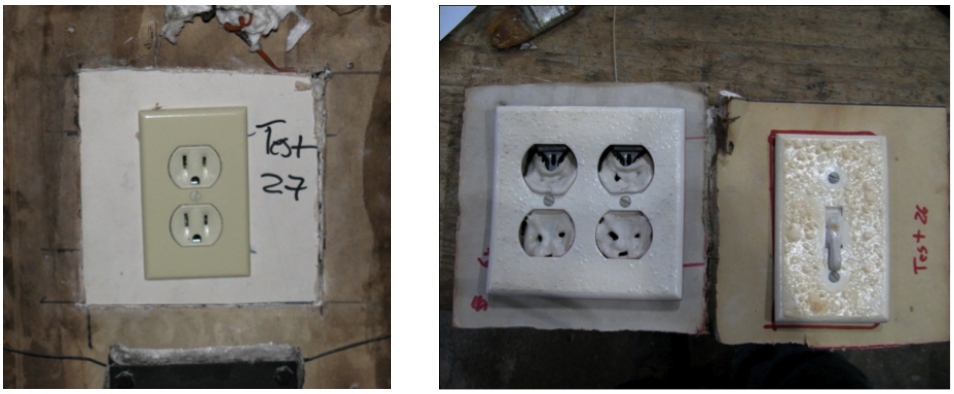

Figure 3.8: Electrical outlet mounted at mid wall elevation prior to fire (left) and typical plugs and switches post fire (right).

flaming. In the absence of PPV, the smoldering should continue during any firefighting suppression process and would eventually self extinguish or be extinguished during overhaul. With improper PPV, there exists a trade-off between the heat loss effects of any void/crevice flow generated by the PPV and the supply of oxygen associated with triggering a flaming reaction in the void.

We identified smoke alarm penetrations, surveillance camera penetrations and other high elevation electrical penetrations as potential paths for hot fire gases to ignite materials within void spaces. Figure 3.9a to 3.9c show the placement of the smoke alarm at the upper level of the compartment. A small failure area of less than 1 cm by 2 cm was located behind a smoke alarm location to simulate a conduit through which wires might pass. Often, the smoke detector would fall off the wall during the testing.

Figure 3.10 shows the placement of wood elements behind the smoke alarm location to simulate typical wooden fixtures such as studs and other mounting surfaces in the void spaces. Also, fiberglass insulation was placed in the void space adjacent to the wood panel to simulate typical thermal insulation and/or sound proofing materials that might be found in void spaces. It is construction details (e.g., unprotected pro-

Figure 3.9: Smoke alarm placement at upper level of fire compartment (left). Close-up view of smoke detector (top right) and half-inch gap behind smoke detector for electrical wiring access (bottom right).

trusions into the wall void) that could impact the transition of interest. Figures 3.11a and 3.11b show the wood panel following fire in the compartment and also the temperature history measured by two thermocouples in the void near the wooden fixture. Note that the wooden panel has burned away and that the thermocouples appear to record an ignition event. Recognize that these "ignition processes" take place before PPV has occurred. Thus, an initial penetration of hot gases into void spaces occurs independent of the application of PPV. Once PPV occurs, however, the smoldering reactions in the void space generally quickly transition to a flaming reaction. The act of applying PPV, for example as might occur during overhaul, triggers the flaming process in the wall void. For these tests, the insulating material was fiberglass insulation. Upon, heating the material melted. The impact of the flammability properties of the wall insulating material will have an effect on the transition to flaming in the wall/void space. It would be interesting to conduct similar tests with other types of insulating materials to see how the type of insulation affects the transition to flaming

ignition.

Figure 3.10: Void space cavity shown from back view (left), inset of void space showing half-inch smoke alarm wiring access gap (top right), wood placed in void space adjacent to wiring gap (middle right), and fiberglass insulation surrounding wood panel in void space (bottom right).

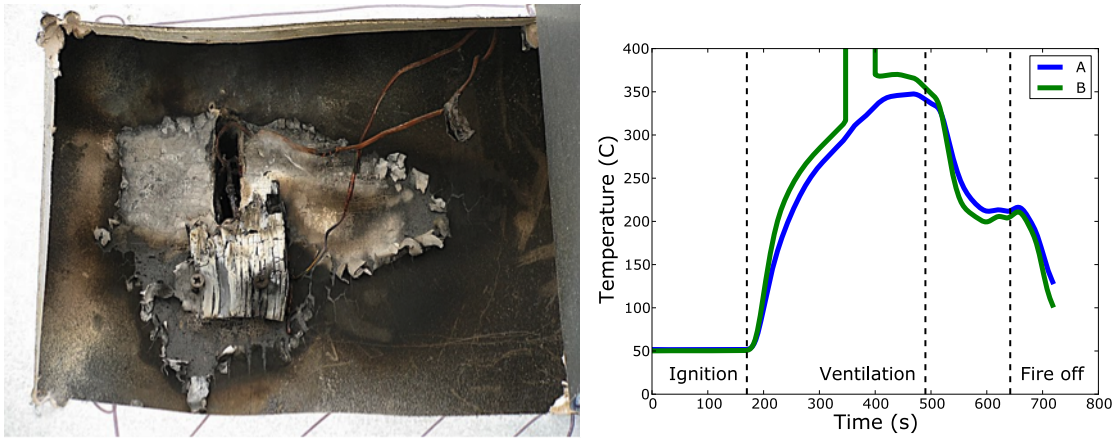

Figure 3.11: Post-fire damage to wood panel in void space behind smoke detector access hole (left) and thermocouple temperatures behind smoke detector in void space (right).

Several tests were performed to address whether or not a void of appropriate gap thickness will in fact cause an ignition process behind the void. The driving pressure that causes hot gases to infiltrate the gap was caused by the natural buoyancy of the fire gases. The natural pressure differential between the fire room and the void space can be estimated using the temperature of the upper layer. This is generally on the order of 5 Pa to 10 Pa. This pressure differential will drive a flow through a channel. The temperatures at the exit plane of the channel were sufficiently hot to ignite the solid material at the back side. Application of PPV simply ensures that enough oxygen is transported into the void to transition the smoldering reaction to a flaming reaction. To more clearly explain the observations, a theoretical modeling framework was developed.

3.5 Theory and Analysis

We developed a theoretical model that couples the large (compartment) scale and small (leakage area) scale effects to determine the conditions under which material in the void space is in danger of ignition. The model encompasses the experimental ventilation conditions as well as the pre-ventilation closed compartment. The relevant parameters for the compartment and leakage scales are detailed for a generic compartment in Figure 3.12.

3.5.1 Compartment scale

At the compartment-scale, we follow the method described by Karlsson [33] and begin with an energy balance.

$$\dot{Q} = \dot{m}_g c_p \Delta T + \dot{q}_{loss} \tag{3.1}$$

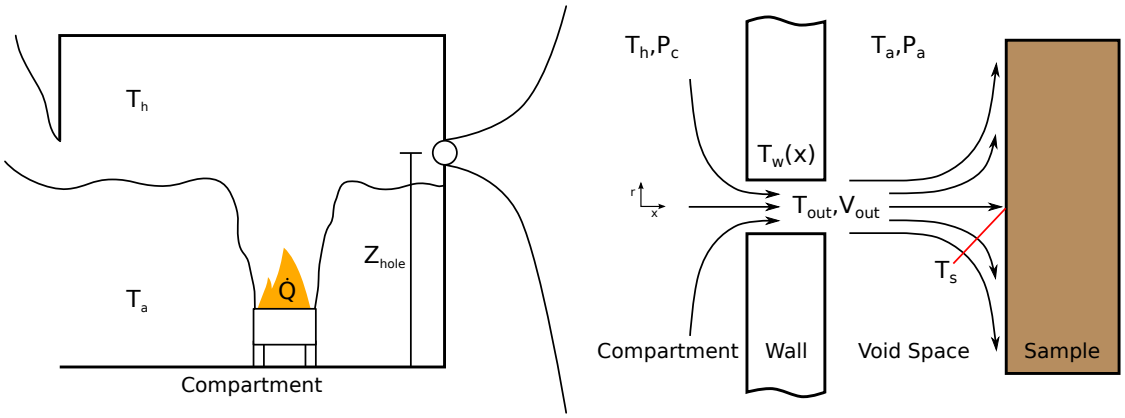

Figure 3.12: Compartment scale heat and mass transfer schematic connected to the leakage scale.

where $\dot{Q}$ is the heat release rate of the fire, $\dot{m}_g$ is the mass flow rate of gas out of the compartment, c_p is the specific heat of air, $\Delta T = T_h - T_a$ is the difference between the hot gas temperature (T_h) and ambient air temperature (T_a), and $\dot{q}_{loss}$ represents other heat loss to the surroundings.

The heat release rate is calculated from the mass flow rate to the burner(s) ($\dot{m}_f$) and the heat of combustion (Δh_c).

$$\dot{Q} = \dot{m}_f \Delta h_c \tag{3.2}$$

To find ΔT in the case of natural ventilation, Karlsson suggests the McCaffery, Quintiere, Harkleroad (MQH) correlation based on the energy balance described in Eq. 3.1.

$$\Delta T = 6.85 \left(\frac{\dot{Q}^2}{A_o \sqrt{H_o} h_k A_T} \right)^{1/3} \tag{3.3}$$

where A_o is the total vent area, H_o is the height of the vent (weighted height in the

case of multiple vents), A_T is solid boundary surface area, and h_k is the effective heat transfer coefficient. We will also use the two-zone model to approximate the temperature difference in the case of "closed" compartment.

In the case of improper PPV, we assume that the compartment is well mixed and that the flow through the leakage and void space is small compared to the flow induced by the PPV fan. We find the temperature difference by rearranging the energy balance and substituting the fan mass flow rate $\dot{m}_v$ for m_g.

$$\Delta T = \frac{\dot{Q}}{\dot{m}_v c_p + \frac{h_k A_T}{\sqrt{\pi}}} \tag{3.4}$$

We can find the compartment pressure profile by applying the Bernoulli equation across each vent and constructing a mass balance. The fluid velocity at each vent can be described as

$$v_i(z) = \sqrt{\frac{2z(\rho_a - \rho_g)g}{\rho_i}} \tag{3.5}$$

where i is ambient airflow into the compartment or hot gas flow out of the compartment, with subscripts a and g respectively. The mass flow rate $\dot{m}$ can then be written as

$$\dot{m}_{ij} = C_d \int_0^z w_j \rho_i v_i(z) \mathrm{d}z \tag{3.6}$$

where j represents the vent name, C_d is the flow coefficient (usually between 0.6 and 0.7), and w_j is the width of vent j. $z = 0$ is defined at the height of the neutral plane H_N, which is the location where the pressure difference is 0.

We construct a mass balance for a compartment with an open door and window (subscripts D and W respectively).

$$\dot{m_{gD}} + \dot{m_{gW}} = \dot{m_{aD}} + \dot{m_{aW}} \tag{3.7}$$

This is solved for the height of the neutral plane by substituting and integrating Eqs. 3.5 to 3.7. The pressure profile for the compartment is constructed as follows:

$$\Delta P(z) = z(\rho_a - \rho_g)g \tag{3.8}$$

The pressure difference induced by improper PPV is an order of magnitude higher than the pressure differences that occur in the case natural ventilation. We will treat the compartment as an approximately uniform pressure zone and calculate the pressure difference following the resistance model described by Weinschenk [19] for improper PPV.

$$\Delta P = 8\rho \left(\frac{Q_{fan}}{\pi D_{fan} H} \right)^2 \frac{1}{S^2 + 1} \left(\frac{0.32x}{H} \right)^2 \tag{3.9}$$

The fan is described by a volumetric flow rate (Q_{fan}) and diameter (D_{fan}). The remaining geometry includes the door height (H), horizontal distance from the fan to door (x), and the ratio of door area not covered by the fan to the area covered by the fan ($S = A_{Exit}/A_{Inlet}$).

3.5.2 Leakage scale

For a leakage into a generic void space as illustrated in Figure 3.12, we constructed a heat and mass transfer model to predict the time to ignition (if ignition occurs) of a sample material inside the void space. Model inputs include compartment hot gas temperature (T_h), compartment pressure (P_c), leakage height (Z_h) leakage diameter (D), leakage depth (l), and material properties of the sample thermal conductivity (k), density (ρ) and specific heat (c_p).

We calculate the channel velocity, V_{out}, by considering the leakage to be a small pipe and applying Bernoulli's equation.

$$V_{out} = \sqrt{\frac{2\Delta P}{\rho K_L}} \tag{3.10}$$

Where ΔP is the pressure difference between the chamber and atmosphere, K_L is the discharge coefficient, and l and D are the spatial dimensions of the leak.

We seek the fluid temperature at the outlet of the leak. We can model the steady state mean fluid temperature (T_m), as follows:

$$\dot{m}'' c_p \frac{\partial T_m}{\partial x} = -\frac{hP}{A}(T_m - T_w(x)) \tag{3.11}$$

where the x-axis is aligned with the direction of flow through the channel and $x = 0$ is on the inside face of the wall and $x = l$ is the outside face. The boundary conditions are

$$T_m(0) = T_h, \quad T_w(x) = (T_a - T_h)(x/l) + T_h \tag{3.12}$$

An analytical solution was found for $T_m(x)$. After solving for T_m at $x = l$, we have the temperature and velocity at the outlet of the leakage (T_{out}), and then analyze heat transfer to the sample from a hot gas jet flow. We begin by setting up the heat equation, defining a new coordinate system with $x = 0$ being the exposed face of the sample, and defining the appropriate initial and boundary conditions as follows. For the sample:

$$\rho c_p \frac{\partial T}{\partial t} = k \frac{\partial^2 T}{\partial x^2} \tag{3.13}$$

Initial condition:

$$T(x, 0) = T_a \tag{3.14}$$

Boundary conditions:

$$as \quad x \to \infty, \quad T = T_a \tag{3.15}$$

$$\left(k\frac{\partial T}{\partial x}\right)_{x=0} = h_c(T_{out} - T) - h_r(T - T_a) \tag{3.16}$$

Where T_a is the ambient temperature and h_r is the radiative heat transfer coefficient approximated by

$$h_r \approx 4\epsilon\sigma T_a^3 \tag{3.17}$$

The heat transfer coefficient (h_c) is given as

$$h_c = Nu\frac{k}{L_c} \tag{3.18}$$

in which the Nusselt Number (Nu_{avg}) is given by a correlation from Wen and Jang [34].

$$Nu_{avg} = 0.442Re^{0.696}Pr^{1/3}(H/D)^{-0.2}(r/D)^{-0.41} \tag{3.19}$$

Re is the Reynolds Number, Pr is the Prandtl Number, H is the distance from the leakage outlet to the sample, and r is the distance from the outlet jet centerline. Equation 3.19 is valid for the range

$$3 < H/D < 16, \quad 0 < r/D < 7.14, \quad 750 < Re < 27,000 \tag{3.20}$$

Solving the heat equation for these conditions, we can approximate the time (t_{ign}) it takes for the surface of the sample to reach the ignition temperature (T_{ign}) using a model for thick ignition with convective heating and radiative losses to the surroundings within the void.

$$t_{ign} \approx \frac{k\rho c}{\pi}\frac{(T_{ign} - T_a)^2}{[h_c(T_{out} - T_{ign}) - h_r(T_{ign} - T_a)]^2} \tag{3.21}$$

The model described in this section provides a simple framework for calculating the time to ignition of a material exposed to a hot impinging jet flow. However, one important assumption for the time to ignition equation is that sufficient oxygen is available at the surface of the material for ignition to occur. In reality, the hot gases entering the void space will contain a mixture of combustion products with the available oxygen in the stream being determined by the conditions inside the compartment (i.e. fire size, type of materials involved, ventilation, etc.). This model does not include the transport of oxygen to the surface of the target material.

3.5.3 Analysis

The equations presented in the previous section were used to construct a model that links compartment scale conditions to the leakage scale effects. By modeling the experimental structure, we seek to gain insight on the range of conditions which could initiate smoldering and/or ignition within the void space. We chose to vary the fire size, leakage location, and leakage dimensions to model the temperature and velocity of the hot gases entering the void space and estimate the possibility of ignition for a given material. This analysis brings to light the need for a more robust compartment scale heat transfer model and for experimental validation of the ignition model under primarily convective heating.

In the experiments, the compartment was initially closed before applying a given ventilation technique. For moderate values of the effective heat transfer coefficient, we found the experiments to be in reasonable agreement with the model. We will begin by focusing on closed compartment conditions at leakage scale. Using the model described in the previous section, we calculate the average gas temperature after passing through the gypsum board (Figure 3.13). The hot gas loses energy as it travels through the leakage with relatively colder walls. As expected, when the

diameter becomes smaller and the length increases, more heat is lost to the walls resulting in lower outlet temperatures for the same compartment temperature.

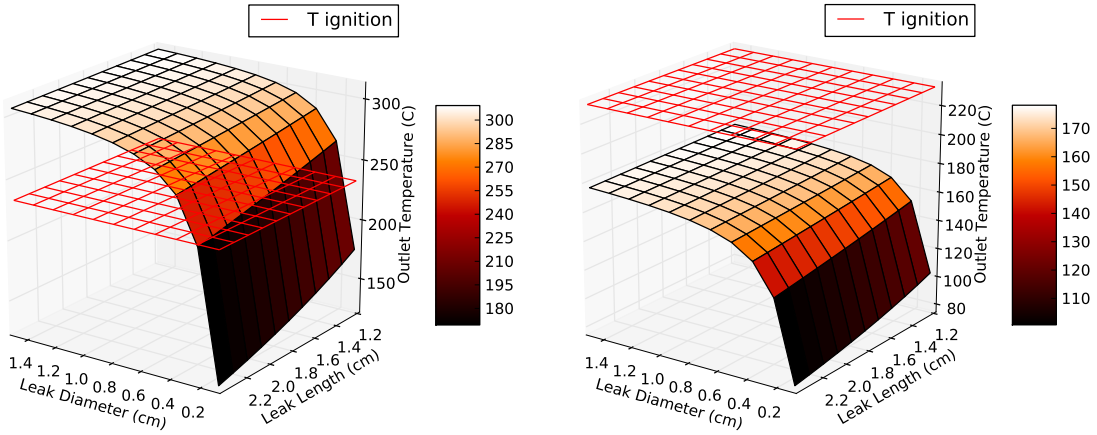

Figure 3.13: Leakage outlet temperature versus geometry for Leakage Height = 2.4 m and HRR = (left) 400 kW and (right) 150 kW.

One criterion we can use to determine the possibility of ignition is the ignition temperature. It is defined as the surface temperature above which ignition can occur and is dependent on the target material [35]. In this case we are using the material properties for a generic cellulose insulation [36]. For a 400 kW fire with a leakage height near the ceiling in Figure 3.13a, we see that a sufficiently large leakage diameter allows gases entering the void space to exceed the ignition temperature of the material. In the experiment, smoldering and ignition were observed when the leakage diameter was 1 cm and the length was 1.6 cm. At this point on the plot, the hot gas temperature exceeds the ignition temperature indicating that ignition is possible. Experimental observations also agree with the model predictions for a lower HRR of 150 kW (Figure 3.13b).

By fixing the leakage geometry to the experimental conditions, we can examine the outlet hot gas temperature as a function of fire size and hole height. This brings

to light an issue with the MQH thermal model. While it is able to sufficiently predict the temperature of the upper hot gas layer, in reality we observed greater thermal stratification in the closed compartment (Figure 3.6). The model predicts only a slight decrease in the temperature drop through the leakage as the hole height decreases. This is a result of the pressure gradient in the compartment, where the gas velocity in the leakage approaches zero as the leakage height approaches the neutral plane. In the experiments, ignition did not occur at lower leakage heights indicating the importance of thermal stratification. This calls for a compartment model with greater temperature resolution than MQH and pressure driven flow to resolve the temperature gradient in the compartment.

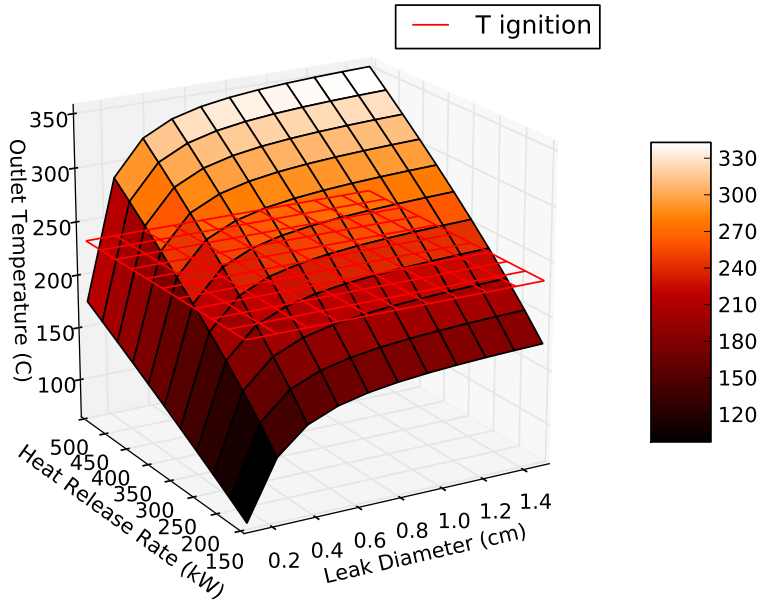

Figure 3.14: Leakage outlet temperature versus HRR and hole diameter for a fixed leakage diameter = 1 cm and leakage height = 2.4 m).

For ceiling level penetrations at high risk for ignition, we hypothesized that a sufficiently small leakage diameter would prohibit ignition within the void space. Figure 3.14 shows the relation between leakage outlet temperature and leakage diameter

over a range of heat release rates. We can see that small leakage diameters keep the leakage outlet temperature from exceeding the material ignition temperature. This is of critical importance because we have the most control over the effective leakage diameter when installing ceiling level wiring for smoke detectors, alarms, etc. Fire stops can be inserted around wiring, thus limiting the available area through which hot gases can enter the void space.

For improper PPV, the more intense mixing within the compartment generally homogenizes the temperature variations within the compartment. While pressures are higher than the closed and naturally ventilated conditions, depending on the HRR, temperatures may be below the ignition temperature of the material within the void space. For the conditions examined in this study the HRR was sufficiently low that the improper PPV mixed temperatures below the ignition temperature. One could imagine scenarios (e.g., post flashover) in which the trade-off between HRR and fan flow rate could create problems with void space ignition at all elevations.

The relatively simple analysis presented here is a useful guide to interpret the size of void holes able to cause ignition. We see that thermal stratification, pressure drop across the wall board, and wall board thickness all affect the likelihood of ignition in the void space.

3.6 Small Scale Experimental System

To better understand ignition within the void space, an experimental system was constructed to reproduce the thermal environment of a compartment scale fire localized to the region where a leakage in the compartment wall is present. This section details the development of this experimental system as well as the first series of ignition tests, the results of which are compared to the theoretical model. The

system was designed such that a range of conditions could be replicated with the focus on the thermal and pressure conditions in the burn structure during a 400 kW fire for a leakage in the compartment wall at ceiling height. This translates to a gas temperature of around 350^{o}C and gage pressure of 5-10 Pa.

3.6.1 Development of experiment

The initial concept for the experiment consisted of a roughly 15 cm by 15 cm 15 cm gypsum box supported by angle iron with openings for a Bunsen burner, air inlet, and hot gas outlet. The first working prototype had internal dimensions of 16.51 cm by 13.97 cm horizontally with an internal height of 16.51 cm. Initially, the joints holding together the walls were sealed with drywall putty and thermocouples were placed inside the box at the top and bottom of the instrument wall (Fig. 3.15). These thermocouples entered the box through the unsealed seams between the wall and the top and bottom sections. A pressure tap was constructed out of a copper tube joined to a pressure transducer (Setra Model 264) via quarter inch plastic tubing. This was inserted through the center of the instrument wall and secured with drywall putty. Adjacent to the instrument wall is the removable leakage wall. A third thermocouple was placed at the leakage outlet, secured to the outside of the leakage wall with the bead centered in the outlet stream.

For the first experimental development test, the Bunsen burner was lit and the burner air control was adjusted until the flame was mostly blue. This was done with the top of the box and leakage wall removed. After adjusting the flame, the top was closed and the leakage wall was slid into place. A large amount of gas was observed exiting through the seam between the walls and top of the box, however very little flow was observed at the leakage outlet.

Next, the bottom seam was sealed with drywall putty and the bottom thermo-

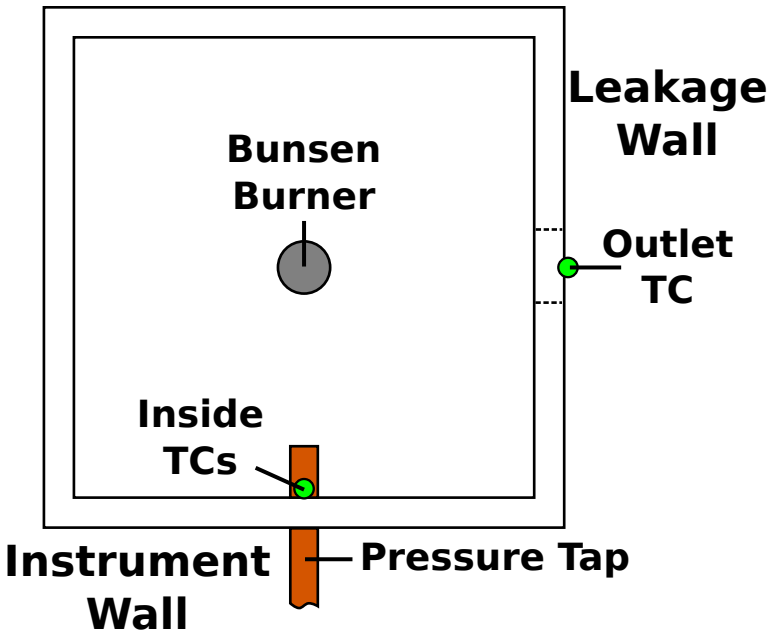

Figure 3.15: Top down illustration inside the void box.

couple was left out. We chose to leave the top unsealed so that the Bunsen burner can be lit in a safe and open configuration. Additionally, this section will likely receive the most damage over the course of several tests, and leaving the top unsealed facilitates its replacement. The next design test revealed that the top was still leaking such that there was very little pressure difference ($\sim$0.5 Pa) between the box and atmosphere. An air inlet was added to the bottom of the box 5.4 cm (center to center distance) away from the Bunsen burner. The air inlet consisted of a copper tube attached to house air with the flow controlled by a pressure regulator. Next, the air was turned on after lighting the Bunsen burner but before closing the box. This resulted in the flame extinguishing when the box leakage section was slid into place. This was likely due to large eddies disrupting the flame sheet.

The next round of changes consisted of drilling holes in the air inlet pipe to diffuse the flow. In addition, a line of fire resistant caulk was applied to the top of the walls and then flattened after drying to improve the seal at the top section.

Drywall putty was applied to the interface between the leakage wall and removable leakage section. After drying, the putty was sanded smooth to improve the seal at the leakage wall. These changes cut down on leakage in subsequent testing, but the flame still extinguished when air was supplied. It was hypothesized that the diffuser holes were not sufficient and a stainless steel pot scrubber was added over the inlet pipe to improve the diffusion of momentum from the air inlet stream and decrease the eddy size in the box (Fig. 3.16). Further testing produced a gage pressure of about 11.5 Pa with a temperature of around 350^{o}C at the outlet thermocouple.

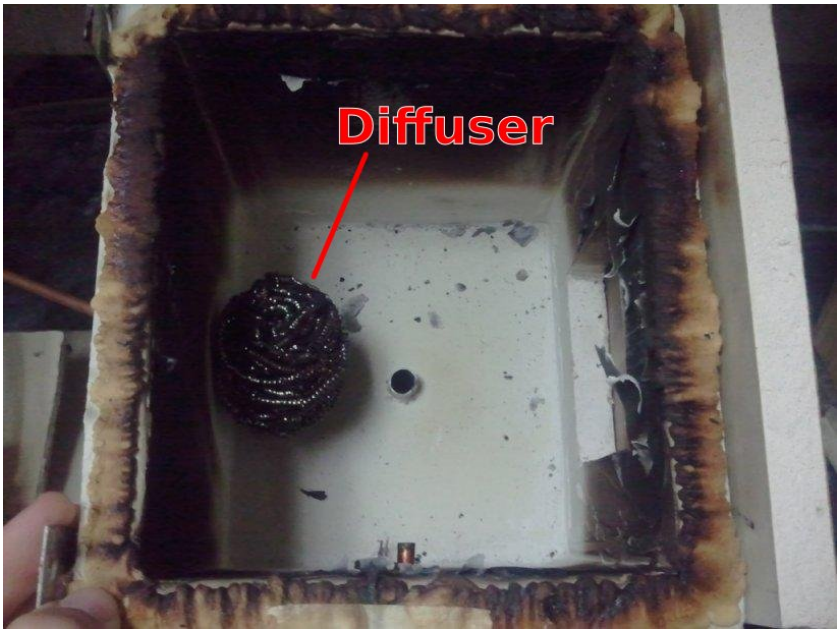

Figure 3.16: Steel diffuser.

With the experimental system now providing basic functionality, more instrumentation was added to facilitate scoping and characterization experiments that test limits of the input variables, primarily the natural gas and air flow rates (Fig. 3.17). The box was instrumented with two thermocouples: one at the top seam and one at the outlet in the center of the leakage hole. A flow meter with a range of 0.4 to 4.0 standard cubic feet per minute (scfm) and accuracy $\pm$%6 full scale was connected to

the air inlet. Another flow meter with a range of 1 to 11 standard cubic feet per hour (scfh) air and accuracy ±%4 full scale was used for the natural gas line. As per the manufacture specifications (King Instrument Company), a factor of 1.34 was used to convert the flow rate to standard cubic feet per hour of natural gas. The collar of the Bunsen burner was marked evenly at four locations to track the air flow in quarter turn increments.

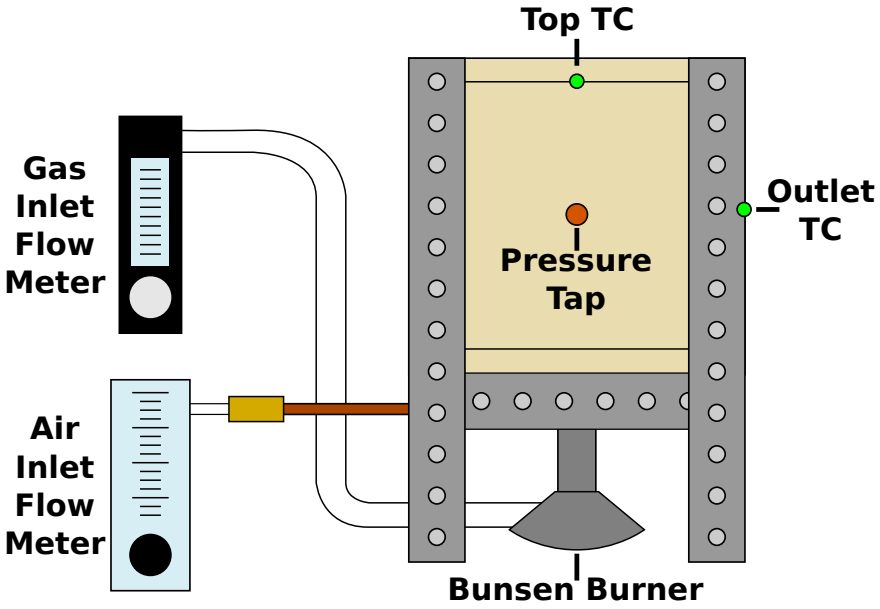

Figure 3.17: Void box setup for scoping tests 1 through 3.

A sample holder was constructed out of 2 in by 4 in lumber with the goal of holding either target material samples, drywall with a target thermocouple, or a heat flux gage. The sample holder was not attached to the box so that the distance from the leakage outlet to the target could be varied. Figure 3.18 shows the sample holder in the target thermocouple and material holder configurations. In the target thermocouple configuration, a hole was drilled through a section of drywall such that the thermocouple in the hole will be aligned with the center of the leakage outlet jet. In the material holder configuration, a thermocouple is also aligned with the outlet

jet but it is taped to the back side of the material and insulated with a 2.5 cm thick square of Kaowool.

Figure 3.18: Sample holder with drywall (left) and oriented strand board (right) targets.

This experimental system allows us to vary six input parameters to test for the thermal conditions and time to ignition of a material. These parameters are the air inlet flow rate, Bunsen burner natural gas flow rate, burner air inlet position, leakage hole diameter, target distance from the leakage outlet, and the target material.

3.6.2 Scoping

A series of thirteen tests were conducted to find the input values that produce conditions similar to test conditions observed in the burn structure (350^{o}C outlet temperature and 5-10 Pa gage pressure). Table 3.1 outlines the scoping tests and the major findings of each. The test conditions, temperature plots, and pressure plots for all scoping tests are listed in Appendix C.

Table 3.1: Scoping tests and findings.

Test #	Air Flow Rate (g/s)	Gas Flow Rate (g/s)	Notes
1	0.34	1.41	Verified flow meter operation
2	Variable	1.41	Found minimum gage pressure of ∼5 Pa
3	N/A	N/A	Burner works with and without burner air flow
4	0.56	1.47	Top temperature was lower than second highest TC
5	0.45	0.98	Weight on ceiling does not affect top TC
6	0.45	0.98	Same peak temperature order for different top TC
7	0.45	0.98	Top TC embedded in wall, now highest temperature
8	0.56	1.23	1 scfm air produces gage pressure of ∼15 Pa
9	0.22	1.72	Outlet temperature between 200^{o}C and 250^{o}C
10	0.34	1.60	Close to desired conditions
11	0.78	1.47	Outlet temperature too low
12	1.01	1.47	Outlet temperature too low
13	0.34	1.47	Outlet temperature too low

The first three scoping tests sought to verify the mechanics of the experimental setup. Both flow meters were verified to have the correct range and the minimum gage pressure was found by slowly turning down the air flow rate. The Bunsen burner air flow was opened and closed during a single test without extinguishing the flame. As expected, the open burner air flow produced higher temperatures as a result of more complete combustion when the fuel and air were premixed.

For the fourth test, four thermocouples measured the box temperatures. Three of the thermocouples passed through holes drilled in the drywall that were sealed with putty. The top thermocouple was inserted through the seam between the ceiling and instrument wall. Test four revealed that the top thermocouple read a lower temperature than the second highest thermocouple (Fig. 3.19a). While it is hypothesized that the box temperatures are stratified, mixing from the diffuser, Bunsen burner and seam leakages could result in temperature variations at the same elevation plane. The sample holder was used in the target thermocouple configuration. It can be noted in Figure 3.19b that the target temperature is higher than the outlet temperature because the paper lining on the drywall began to smolder.

For test seven, the top thermocouple was moved to 15.24 cm from the base of the box and inserted into the box in the same manner as the other three embedded thermocouples. This resulted in the top thermocouple reading the highest box temperature (Fig. 3.20). This is indicative of thermal stratification within the compartment and further investigation with more in-box thermocouples would provide greater resolution to the actual temperature profile at a given elevation plane. The locations of the four in-box thermocouples are 1.27, 5.72, 10.80, and 15.24 cm from the floor of the box. The sample holder was set up in the material holder configuration using plain white printer paper as the target material and placed at a distance of 4.1

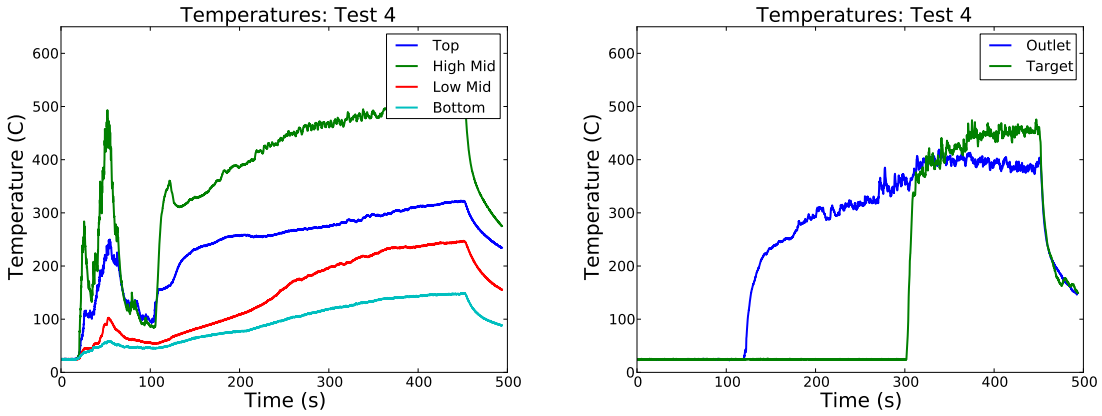

Figure 3.19: Temperatures during scoping test 4 inside the box (left) and at the outlet and target (right). The leakage section was inserted at 120 seconds, the target was positioned 300 seconds, and the gas was turned off at 450 seconds.

cm from the leakage outlet. The paper did not ignite and the target thermocouple was not touching the paper during the experiment. Only a slight temperature increase was observed by the target thermocouple with a peak around 35^{o}C (Fig 3.20b).

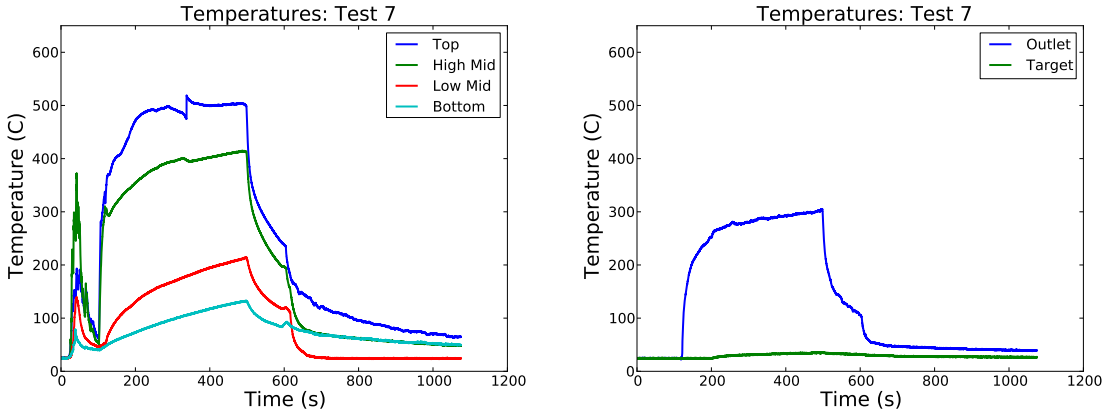

Figure 3.20: Temperatures during scoping test 7 inside the box (left) and at the outlet and target (right).

Moving the top thermocouple was the final major change to the instrumentation arrangement. The experimental set up used for test seven and shown in Fig-

ure 3.21, was used for the remainder of the experiments with only minor changes.

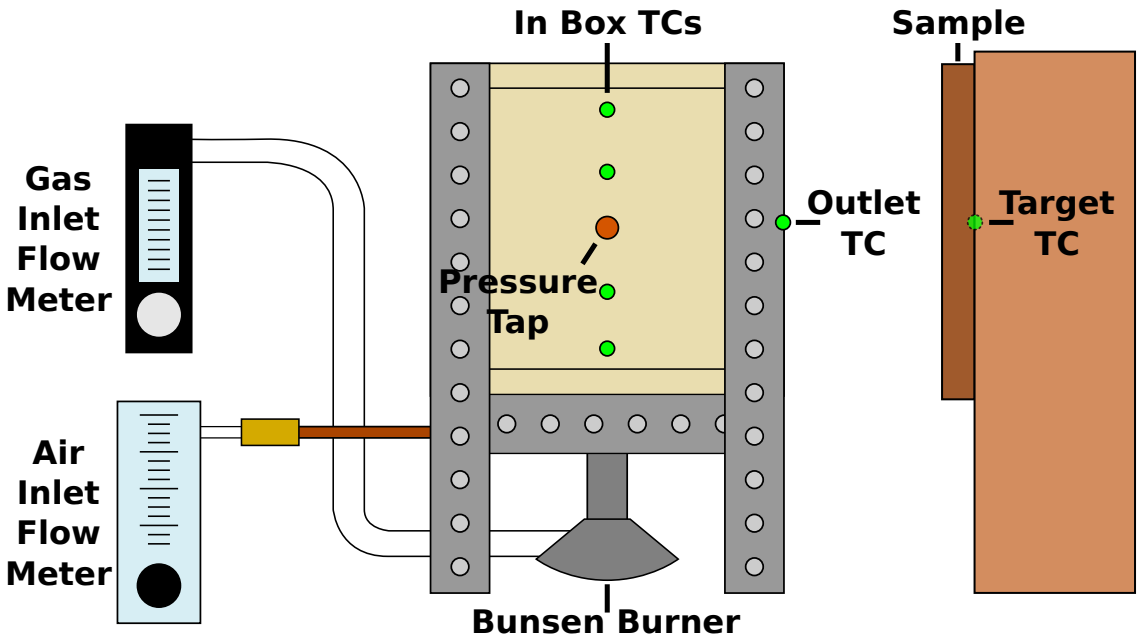

Figure 3.21: Full experimental set up.

The first ignition test was attempted for test number nine and will be discussed in greater detail in the Ignition Experiments section. The temperature and gage pressure were both below the target values and it was hypothesized that fire was under ventilated. Tests ten through twelve focused on increasing the air flow rate at lower gas flow rates than text nine.

The conditions for test ten met the target criteria and were chosen for the ignition experiments: 0.6 scfm air flow rate, 6.5 scfh gas flow rate, and 1.75 turns for the burner air inlet. It was determined that approximately 90 seconds of closed-box operation was required for the thermal and pressure criteria to reach the desired values, at this point the ignition target can be applied. In conjunction with conducting the scoping experiments, an experimental procedure was developed for efficient testing and repeatability; the steps of which are listed in Appendix B.

3.6.3 Flow characterization

The flow at the leakage outlet for a 1.27 cm diameter leakage was characterized by taking velocity measurements with a hot-wire anemometer (Amprobe Model TMA-21HW) for a range of 2.5 to 20 Pa gage pressure. The anemometer was placed about 1 cm from the leakage outlet and the Bunsen burner was left off with the burner air and gas inlets closed. The air flow rate was adjusted to reach the desired gage pressure values. Figure 3.22 shows the measured velocities versus gage pressure as well as the velocity calculated by applying Bernoulli's equation (Eqn. 3.10) with $K_L = 1$ and density of air calculated at the temperature of the room. The measured velocities were found to be in good agreement with the theory.

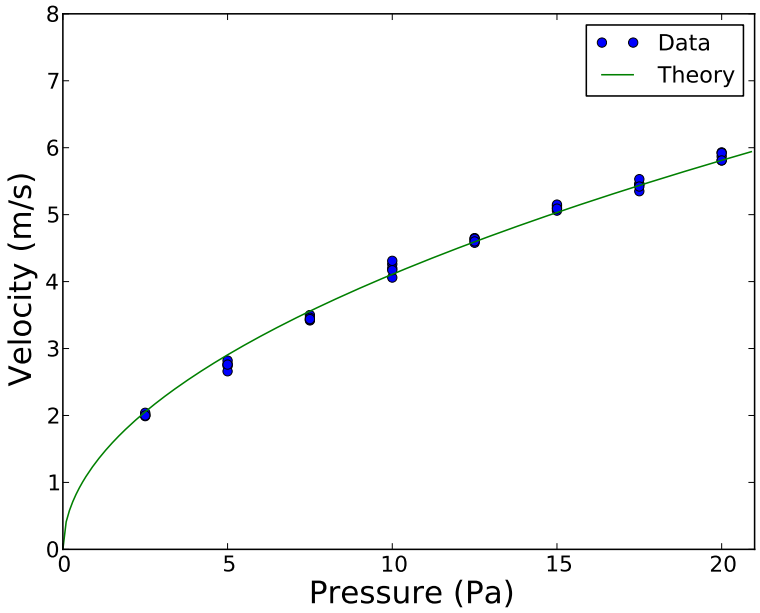

Figure 3.22: Velocity versus gage pressure for room temperature leakage test.

3.6.4 Ignition Experiments

A total of eight ignition tests were conducted on samples of oriented strand board (OSB), including scoping test number nine. Oriented strand board was chosen

Figure 3.23: Anemometer set up for room temperature leakage test.

as a target material because it is commonly found inside wall and ceiling void spaces. The target conditions for each test were a gage pressure between 5 and 8 Pa with outlet temperatures around 350^{o}C. These conditions were produced using the same set of burner and air flow input values mentioned previously, only the target spacing was varied between 1 and 2.5 centimeters between tests. The leakage hold diameter was kept constant at 1.27 cm for all ignition tests. Table 3.2 lists the average gage pressure, average outlet temperature, and time to first ignition (if ignition occurred) for each of the eight tests. The pressure criterion was met in all tests except for number nine. However, the outlet temperature criteria was exceeded in six of the eight tests, while the temperature readings for the remaining two tests (nine and fourteen) were not the true outlet temperature due to the thermocouple coming loose and slipping out of the outlet stream. For tests fifteen through twenty, the outlet temperature began around 300^{o}C to 400^{o}C and rose as the experiment progressed. The average outlet temperature in each case, with the exception of test twenty, was

below 600^{o}C which is indicative of a pre-flashover compartment fire [37]. This section details the observations made for each experiment and conclusions drawn from this round of ignition testing. The test conditions, temperature plots, pressure plots, and char patterns for all ignition tests are cataloged in Appendix C.

Table 3.2: Results of OSB ignition tests, "X" indicates no ignition event occurred, "N" indicates not cataloged (*Outlet thermocouple slipped out of alignment).

Target Spacing (cm)	Test #	Time to Glow/Flame (s)	Average Gage Pressure (Pa)	Average Outlet Temperature (^oC)
1.0	14	N /115	5.7	313*
	16	N /282	5.9	477
	18	126/212	5.7	532
	20	12 /107	5.8	601
2.5	9	X / X	4.1	233*
	15	153/178	5.2	433
	17	180/ X	6.0	453
	19	284/ X	6.6	544

In test nine, the outlet thermocouple slipped out of position when the leakage wall was inserted into the frame causing it to read a lower temperature outside of the outlet stream. The maximum box temperature was around 350^{o}C and based on observations in previous tests, the outlet temperature likely approached the upper box temperature. While no ignition was observed, a small char pattern was observed on the target OSB (Fig. 3.24).

The maximum box temperature was around 500^{o}C in test fourteen. In this case, the outlet thermocouple slipped due to charring of the tape holding it in place (Fig. 3.25a), and staples were added to secure the thermocouple as seen in Figure 3.25b for each of the following tests. Intermittent flaming began at 115 seconds after the target was set in place at 1 cm from the leakage outlet. Small flickers of flame lasted until the burner was turned off. More charring was observed than in

Figure 3.24: Char pattern for test nine.

test nine, producing a char pattern with a width and height of roughly 2.2 and 2.5 cm respectively (Fig. 3.18b). Char patterns images and dimensions for the remaining tests can be found in Appendix C.4.

Figure 3.25: Charring observed on tape after test fourteen (left) and staple arrangement for securing the outlet thermocouple (right).

Test fifteen was the only instance where a flame was observed at the 2.5 cm target spacing. Glowing began on the target at 153 seconds onward, and a single

flame flicker was observed at 178 seconds. For reporting purposes, all time to ignition values in Table 3.2 are the time at which the first instance of a flame was observed.

Video and thermal imaging cameras were used to record tests sixteen and seventeen. Charring occurred almost immediately (Fig. 3.26a) in test sixteen with the first flame observed at 282 seconds after positioning the target (Fig. 3.26b). Small pulses of flaming combustion were observed regularly for the remainder of the test.

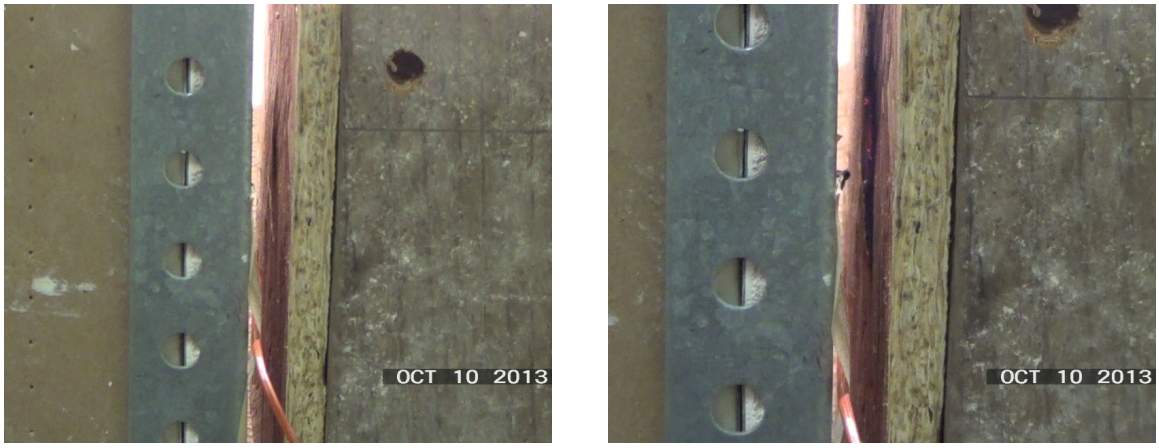

Figure 3.26: Charring observed ten seconds after target was positioned (left) and brief flame flicker at 282 seconds after target was positioned (right).

Tests seventeen and nineteen behaved similarly in that each had a target spacing of 2.5 cm and ignition was not observed. However, both targets still pyrolysed producing char patterns with dimensions of 5.1 and 5.7 cm and 5.7 and 6.4 cm respectively with glowing ignition observed in each test.

Tests eighteen and twenty were conducted with a 1 cm target spacing, and ignition was observed in both cases. In test eighteen, small pulses of flame were observed beginning 188 seconds after target application transitioning into larger pulses from 212 seconds onward. Ignition occurred in only 107 seconds in test twenty, and intermittent flaming was observed for the remainder of the time the flame was on. After the flame was turned off, the air was left on and the sample began to glow with

greater intensity as seen in Figure 3.27b. The sample right before the burner was turned off is shown in Figure 3.27a for comparison. This could be seen as similar to the application of PPV in that combustion products are cleared from a compartment resulting in a more oxygen rich stream entering into the void space. However, the hypothesis is that PPV will not cause a transition to glowing ignition if the material hasn't already reached the ignition temperature.

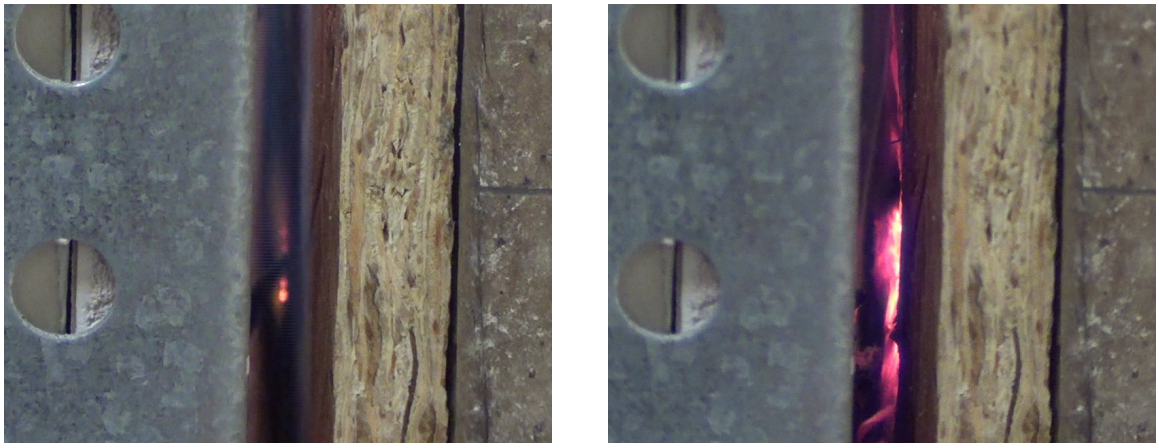

Figure 3.27: Flickering OSB before the burner was turned off (left) and intensified glowing after the burner was turned off and the air left on (right).

Table 3.3 lists the calculated values of the Reynolds number, Nusselt number, and heat transfer coefficient with the current model. The Reynolds number is calculated using the velocity from Equation 3.10 and properties of air at the average outlet temperature measured by the outlet thermocouple. The Nusselt number is calculated with Equation 3.19, however the experimental conditions are just outside the valid range for target distance over leakage diameter (H/D in Eqn. 3.20) where H/D is 1.97 and 0.79 for the 2.5 cm and 1.0 cm cases respectively. This correlation represents the closest fit to the experimental conditions found in literature as most correlations are developed for jet cooling processes that operate at much higher Reynolds numbers [38]. The result is a heat transfer coefficient prediction that ranges from 150 to

200 $\frac{W}{m^2K}$. This range appears to be high when compared to work conducted under similar conditions which found that the heat transfer coefficient was on the order of 50 $\frac{W}{m^2K}$ [39].

Table 3.3: Calculated Reynolds number, Nusselt number and heat transfer coefficient for ignition tests (omitting tests 9 and 14).

Target Spacing (cm)	Test #	Reynolds Number	Nusselt Number	Heat Transfer Coefficient ($\frac{W}{m^2K}$)
1.0	16	840.8	45.0	192
	18	761.9	42.0	190
	20	696.7	39.5	190
2.5	15	840.4	37.4	153
	17	875.0	38.5	161
	19	806.1	36.4	166

Out of the four experiments with 2.5 cm target spacing, only one transition to flaming ignition was observed whereas each of the 1 cm tests transitioned to flaming. Plotting both glowing and flaming time to ignition versus outlet temperature produces interesting results, excluding tests 9 and 14 due to inaccurate outlet temperature readings (Fig. 3.28). For the 1 cm target spacing tests the time to both glowing and flaming ignition was negatively correlated with the average outlet temperature. However, ignition times were positively correlated with the average outlet temperature for the 2.5 cm tests. The average gage pressure was fairly consistent (between 5.2 and 6.6 Pa) for tests 15 through 20, which indicates that there is another factor besides temperature and pressure that determines ignition. Besides ignition temperature, another common criteria for ignition modeling is the mass loss rate of the material [40]. There are four main mass flows near the surface of the target: products from the leakage outlet flowing in, entrained air flowing with the leakage outlet stream, volatiles flowing from the target material, and mixture of the previous three flows leaving the

area. The trends observed in Figure 3.28 are mostly likely due to the resulting gas composition near the target.

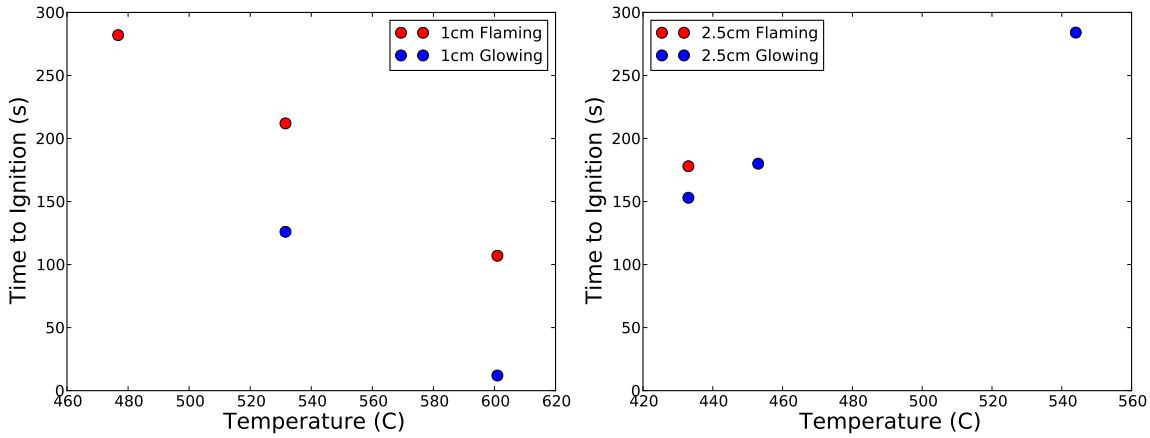

Figure 3.28: Time to ignition versus average outlet temperature for OSB samples at 1cm spacing (left) and 2.5cm spacing (right). Red indicates glowing ignition and blue indicates flaming ignition.

The set of ignition experiments present a framework for future testing of void space ignition. Following this framework more modeling work, including mixture fraction models, and experiments can be conducted in the future to better understand the mechanisms involved. Theses experiments have shown that under pre-flash conditions, both glowing and flaming ignition can occur in the void space.

3.7 Conclusions

Positive pressure ventilation is a tactic used by the fire service wherein a fan flow is directed into a compartment or structure that contains a fire and hot products of combustion. The intent is to use the fan flow to clear the hot products from the structure. Questions have arisen on the hazards associated with directing a fan flow into a compartment with fire gases inside. In particular, there are concerns about the fan pressurization process "driving" fire into void spaces within the walls

of the structure. Little has been said in the literature about this process. In fact, there has not been a clear consensus on how fire extension takes place in structures. Overall, the experimental data show that ventilation does not cause a significant jump in void space temperature, when the failure location is at this mid-height in the compartment. However, there is a significant increase in void space velocity for the pressurized PPV case. The temperature effects were never able to cause ignition of combustible material in the void space when the failure area was located at these mid-wall heights. This was irrespective of the fire size (150 kW to 400 kW) and location of the burners relative to the GFA.

The highest temperatures within a wall void occur near the point where gases enter the void space (i.e., the failure point). The further removed from the failure location, the lower the temperatures. The potential for ignition inside the wall/void is strongly correlated to the compartment temperature at the elevation of the void penetration (i.e., wall failure location). This suggests that lower elevation failures are much less dangerous than high elevation failures because of the inherent stratification in the compartment. This also suggests that electrical outlets and electrical switches might not represent significant points of fire penetration since they are generally located at relatively low elevations. The work in this chapter shows a mechanism for fire extension based upon high elevation penetrations in the protective skin of the compartment (i.e., the gypsum board). These penetrations are often there for electrical wiring access as part of other safety systems (e.g., smoke alarms and security cameras). We find that the transition from a smoldering wall void space reaction to a flaming reaction may be accelerated by the application of PPV through the addition of oxygen into the void space, provided combustion was already occurring before the application of PPV. The hot gas layer temperatures indicative of a pre-flashover compartment are shown to be capable of causing both smoldering and flaming ignition

for penetration sizes similar to those used for safety systems at length scales associated with void spaces.

Chapter 4

Conclusions

4.1 Conclusions

Two scenarios with impinging jet flow heat transfer processes were studied in this thesis. For both the ablation and void space scenarios heat and mass transfer theory was developed, experiments were conducted, and modeling efforts were made to attempt to understand the processes.

In the ablation scenario, the target measuring the recession rate using sensor system. A one-dimensional finite volume ablation model was developed with Arrhenius kinetics describing the dependence of the mass loss rate on temperature at the surface. A series of recession experiments were conducted on a carbon-phenolic material using embedded thermocouples to track the temperature evolution and material recession. The acoustic response of the material was explored for a given heat flux and verified with the thermal model. Two inversion techniques that predict the ablation rate with the thermal model using feedback from a fusion of thermal and acoustic sensor data were designed and tested. When the first technique was shown to be insufficient, a novel inversion method was developed that utilizes parallel computing. This technique was shown to accurately reproduce synthetic data generated by the thermal model, but fell short in producing the transient temperature profile observed in the experiments. Future work will focus on improving the level of detail of the thermal model and expanding the parameter search space of the parallel inversion technique.

The goal of the void space work was to examine the effects of PPV on void space temperatures and to verify an internal wall ignition that was observed in one of the compartment-scale experiments. A theoretical framework was compiled to model thermal conditions at the compartment and void levels. Through the theory, it was shown that ignition can happen under certain conditions and leak geometries with the greatest danger closest to the ceiling. Experimental void space temperatures and theoretical analysis pointed to a range of temperature and pressure conditions present in the compartment that could lead to void space ignition. Leak-scale experiments were conducted to test ignition under these proposed conditions and it was shown that both flaming and smoldering ignition can occur for a wooden building material. This work highlights the need for a better understanding of the ignitability of other building materials under convective dominated heat transfer.

Appendices

Appendix A

Iterative Hypercube Sampler Code Excerpts

A.1 Root Processor

```
...
# Scatter input strings
myVals = comm.scatter(curWorkVal,root=0)

# Do work on personal input string
itVars = hype.inParse(myVals)
myTemps = oned_forward.forward(itVars,tTCs,t_dur)[0]

# Calculate error
myErr = errs.breakFL(myTemps,tTCs,testNum)

# Gather outputs
curWorkErr = comm.gather(myErr,root=0)

# Store error values
errDict = hype.stoErr(errDict,curWorkKey,curWorkErr)
...
```

A.2 Worker Processors

```
...
while comp != None:
    # Get input string from scatter
    myVals = comm.scatter(curWorkVal,root=0)

    if myVals != 'OneMoreTime':
        if myVals != None:
            # Do work on personal input string
            itVars = hype.inParse(myVals)
            myTemps = oned_forward.forward(itVars,tTCs,t_dur)[0]

            # Calculate Error
```

```
            myErr = errs.breakFL(myTemps,tTCs,testNum)

            # Gather outputs
            curWorkErr = comm.gather(myErr,root=0)
        else:
            comp = None
    else:
        myErr = None
        curWorkErr = comm.gather(myErr,root=0)
...
```

Appendix B

Void Box Experimental Method

- Put on proper PPE (goggles and gloves).
- Turn on HP laptop, plug in DAQ, and load "Void_2.vi" in LabView.
- Check all connections and instrument position:
  - 6 TCs (4 in box, 1 outlet, 1 target)
  - Pressure tap and transducer
  - Air gage to hood air and diffuser tube
  - Gas gage to hood and Bunsen burner (dial open)
  - Bunsen burner air and gas control
  - Target spacing template
- Use the output file name "Cold_Check.lvm" and run VI to test instrument signals.
- If all readings are normal (ambient temperature and 0 gage pressure), stop VI and change output to the test name.
- Check that gas flow control on Bunsen burner is closed, open air to 1/4 turn.
- Open gas on the wall, open gas on the hood. You should see a short spike on the gas flow gage but no continuous flow.

- Start the VI.
- Open Bunsen burner gas slightly and ignite with a lighter.
- Open gas to get the desired flow rate.
- Open burner air until flame mostly blue (log the number of turns to the nearest quarter turn).
- Turn on house air and adjust to desired value (adjusting can be done before the test to save time).
- Close lid and check that the flame is still on.
- Close outlet wall and check the flame. Take note of the test time on VI clock.
- At 90 s after closing outlet wall, move target into position, take note of the test time.
- During the test:
  - Monitor box temperature for flame outage
  - Monitor the target for ignition
  - Take note of the first ignition
  - Take notes on any other observations
- 300 s after positioning the target, turn off the gas at the wall level.
- Stop the VI.
- Shut off gas at hood level and shut off the hood air.
- Save the data to a flash drive while the experiment cools.

Appendix C

Void Space Experimental Data

C.1 Test Matrix

Table C.1: Scoping raw inputs and absolute timing.

Test #	Air (scfm)	Gas (scfh)	Burner Air (turns)	Hole Diameter (m)	Target Distance (m)	Close Box (s)	Target On (s)	Ignition (s)	Flame Off (s)	Target Material
1	0.6	5.75	X	0.0127	X	140	X	X	X	X
2	X	5.75	X	0.0127	X	140	X	X	X	X
3	X	X	X	0.0127	X	100	X	X	X	X
4	1	6	1.5	0.0127	0.02	120	300	X	450	Gypsum
5	0.8	4	1.25	0.0127	0.015	215	325	X	460	Gypsum
6	0.8	4	1.25	0.0127	X	X	X	X	X	X
7	0.8	4	1.25	0.0127	0.041	120	200	X	500	Paper
8	1	5	1.5	0.0127	0.025	115	290	X	600	Paper
9	0.4	7	2.25	0.0127	0.025	180	270	X	638	OSB
10	0.6	6.5	1.75	0.0127	X	165	X	X	400	X
11	1.4	6	1.5	0.0127	X	133	X	X	300	X
12	1.8	6	1.5	0.0127	X	96	X	X	300	X
13	0.6	6	1.5	0.0127	X	67	X	X	210	X
14	0.6	6.5	1.75	0.0127	0.01	95	185	300	485	OSB
15	0.6	6.5	1.75	0.0127	0.025	182	272	450	572	OSB
16	0.6	6.5	1.75	0.0127	0.01	98	188	470	548	OSB
17	0.6	6.5	1.75	0.0127	0.025	114	204	X	567	OSB
18	0.6	6.5	1.75	0.0127	0.01	96	188	400	488	OSB
19	0.6	6.5	1.75	0.0127	0.025	92	183	X	547	OSB
20	0.6	6.5	1.75	0.0127	0.01	84	178	285	485	OSB

C.2 Temperature Plots

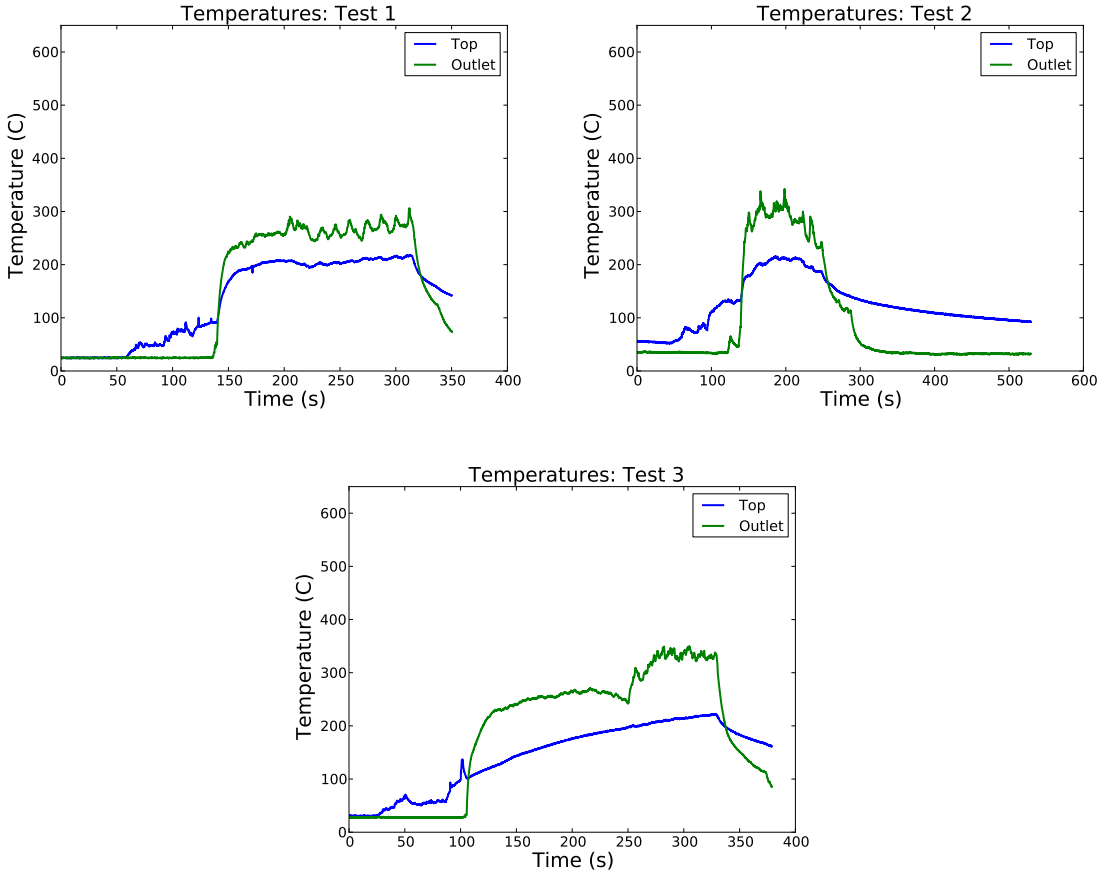

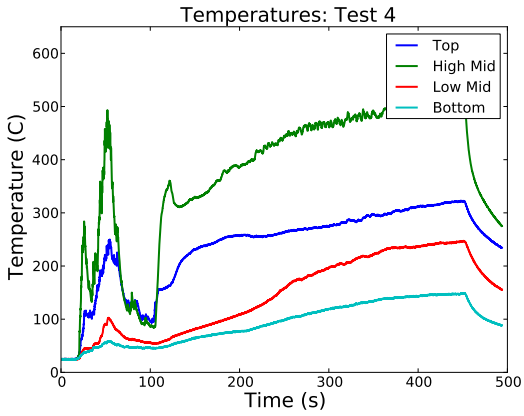
Temperatures: Test 4
Top
High Mid
Low Mid
Bottom
Temperature (C)
Time (s)
0
100
200
300
400
500
600

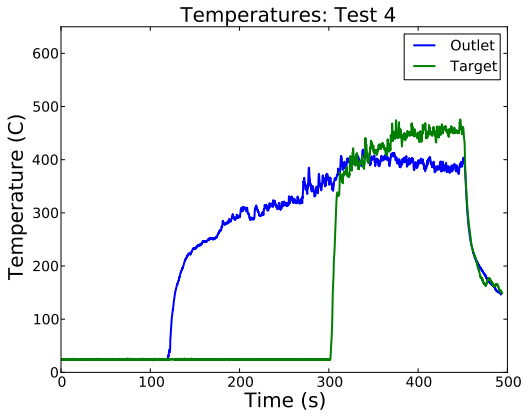
Temperatures: Test 4
Outlet
Target
Temperature (C)
Time (s)
0
100
200
300
400
500
600

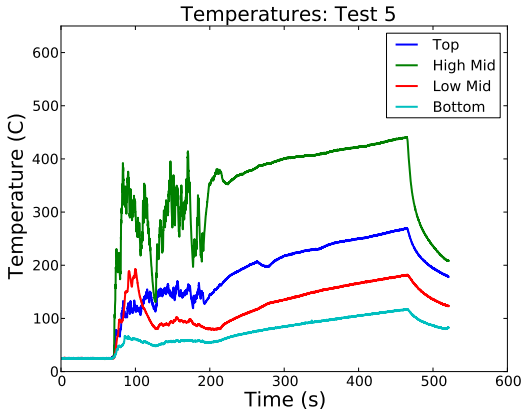
Temperatures: Test 5
Top
High Mid
Low Mid
Bottom
Temperature (C)
Time (s)
0
100
200
300
400
500
600

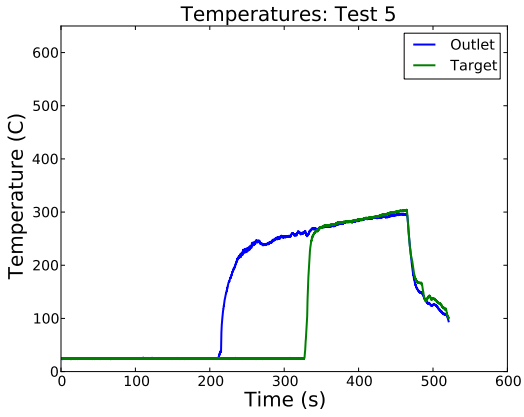
Temperatures: Test 5
Outlet
Target
Temperature (C)
Time (s)
0
100
200
300
400
500
600

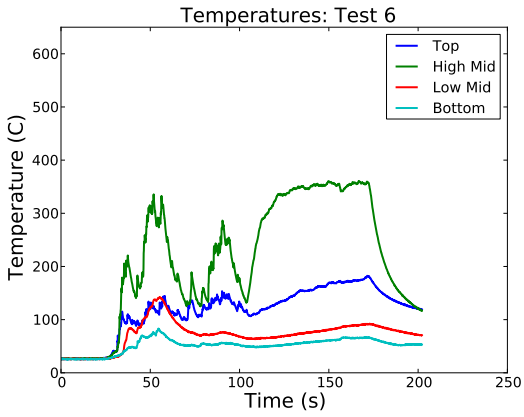
Temperatures: Test 6
Top
High Mid
Low Mid
Bottom
Temperature (C)
Time (s)
0
50
100
150
200
250
300
400
500
600

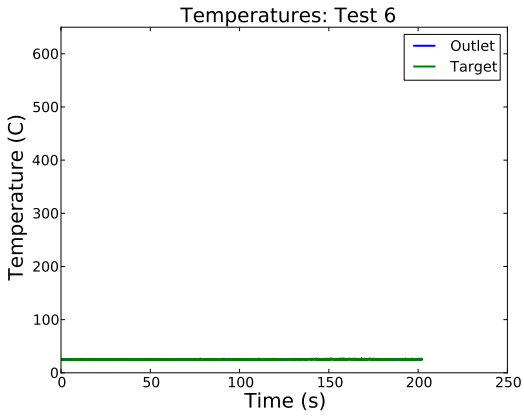
Temperatures: Test 6
Outlet
Target
Temperature (C)
Time (s)
0
50
100
150
200
250
300
400
500
600

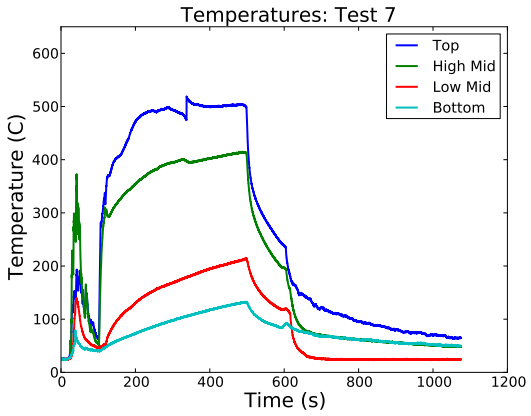
Temperatures: Test 7
Top
High Mid
Low Mid
Bottom
Temperature (C)
Time (s)
0
100
200
300
400
500
600
0
200
400
600
800
1000
1200

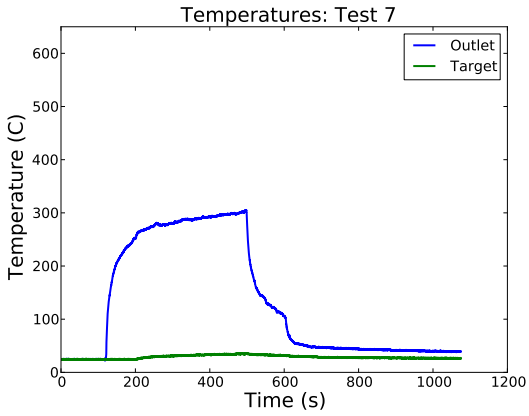
Temperatures: Test 7
Outlet
Target
Temperature (C)
Time (s)
0
100
200
300
400
500
600
0
200
400
600
800
1000
1200

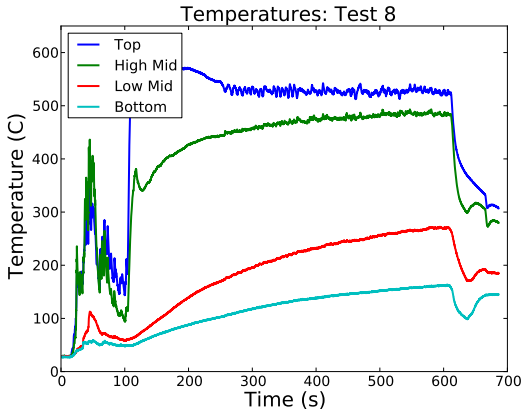
Temperatures: Test 8
Top
High Mid
Low Mid
Bottom
Temperature (C)
Time (s)
0
100
200
300
400
500
600
0
100
200
300
400
500
600
700

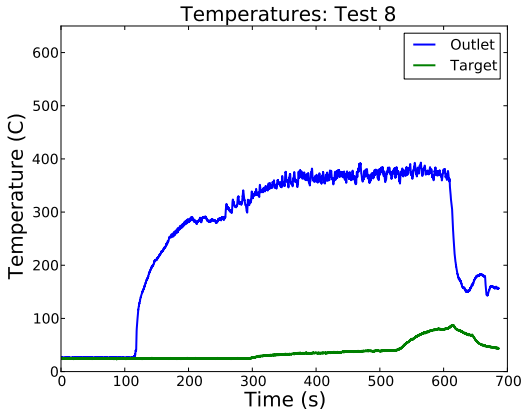
Temperatures: Test 8
Outlet
Target
Temperature (C)
Time (s)
0
100
200
300
400
500
600
0
100
200
300
400
500
600
700

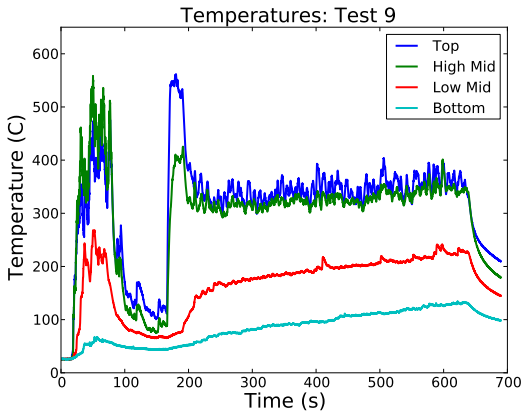
Temperatures: Test 9
Top
High Mid
Low Mid
Bottom
Temperature (C)
Time (s)
0
100
200
300
400
500
600
0
100
200
300
400
500
600
700

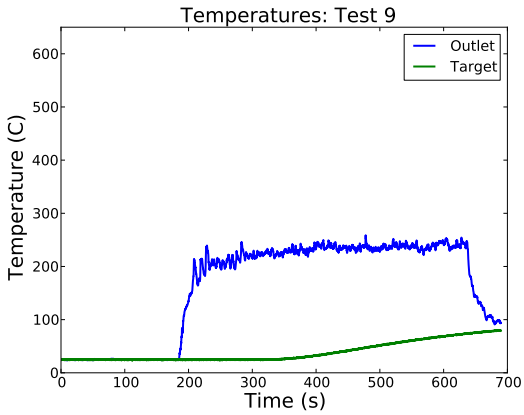
Temperatures: Test 9
Outlet
Target
Temperature (C)
Time (s)
0
100
200
300
400
500
600
0
100
200
300
400
500
600
700

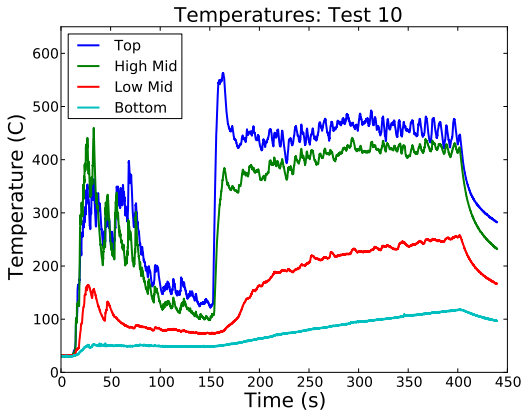
Temperatures: Test 10
Top
High Mid
Low Mid
Bottom
Temperature (C)
Time (s)

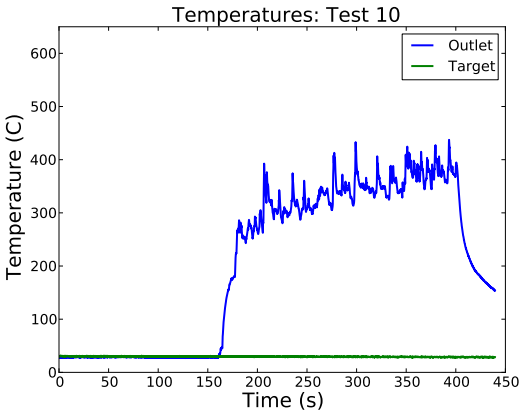
Temperatures: Test 10
Outlet
Target
Temperature (C)
Time (s)

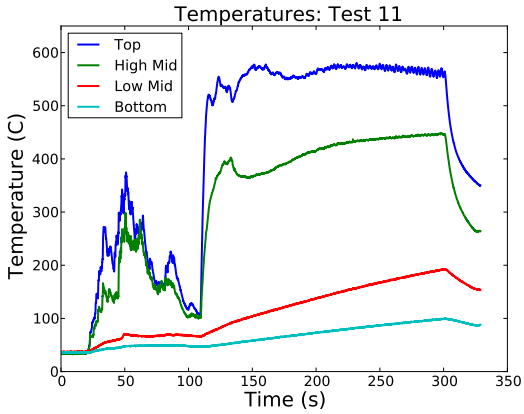
Temperatures: Test 11
Top
High Mid
Low Mid
Bottom
Temperature (C)
Time (s)

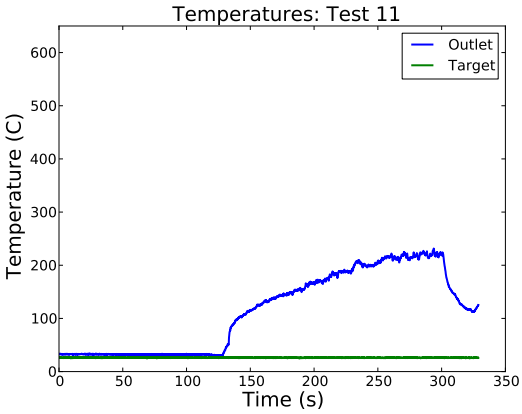
Temperatures: Test 11
Outlet
Target
Temperature (C)
Time (s)

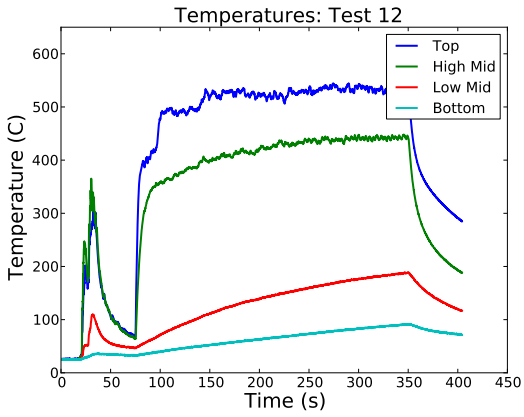
Temperatures: Test 12
Top
High Mid
Low Mid
Bottom
Temperature (C)
Time (s)

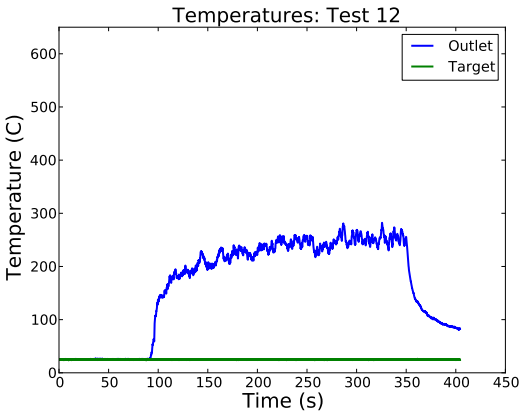
Temperatures: Test 12
Outlet
Target
Temperature (C)
Time (s)

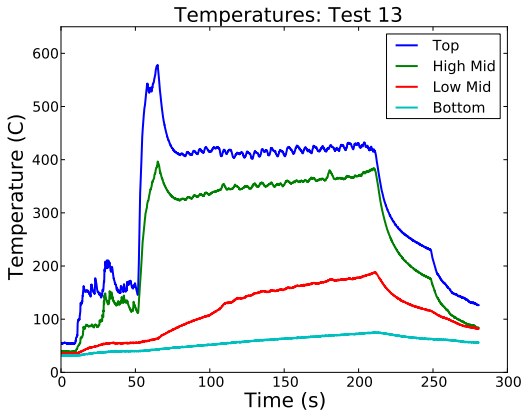
Temperatures: Test 13
Top
High Mid
Low Mid
Bottom
Temperature (C)
Time (s)

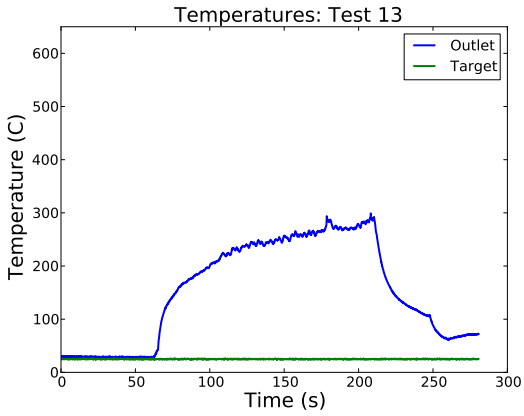
Temperatures: Test 13
Outlet
Target
Temperature (C)
Time (s)

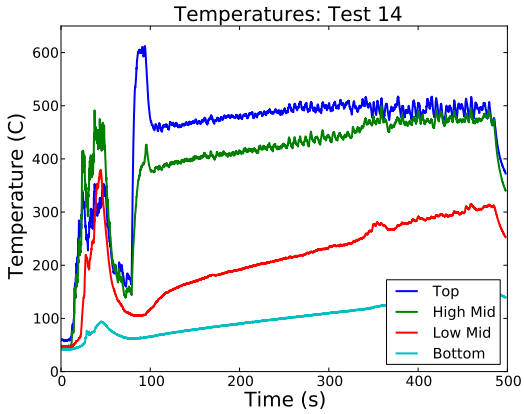
Temperatures: Test 14
Top
High Mid
Low Mid
Bottom
Temperature (C)
Time (s)

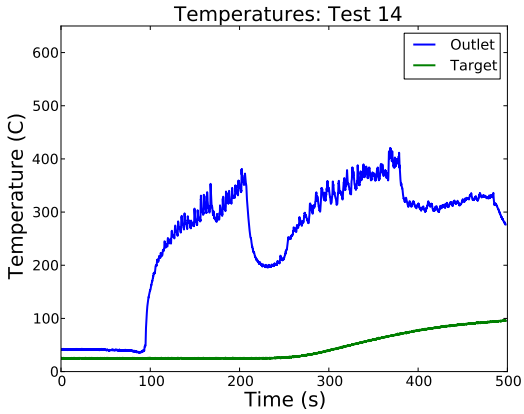
Temperatures: Test 14
Outlet
Target
Temperature (C)
Time (s)

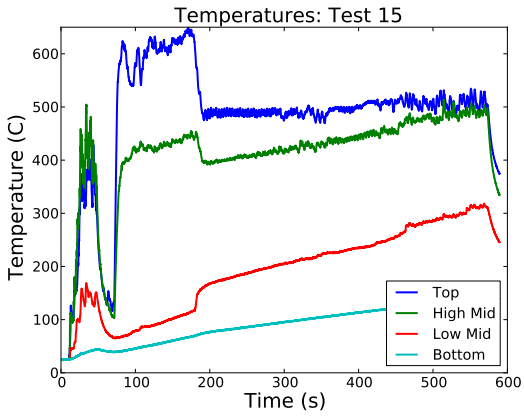
Temperatures: Test 15
Top
High Mid
Low Mid
Bottom
Temperature (C)
Time (s)

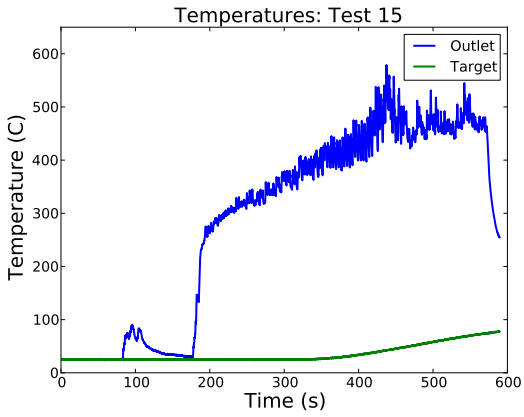
Temperatures: Test 15
Outlet
Target
Temperature (C)
Time (s)

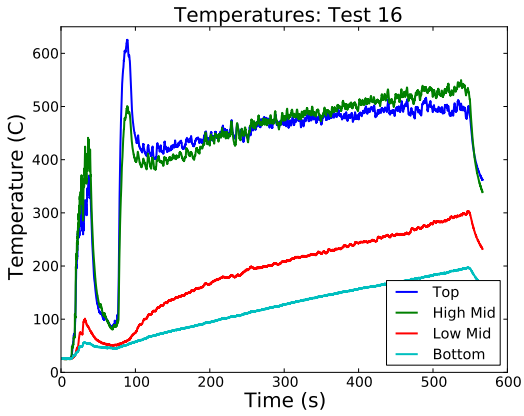
Temperatures: Test 16
Temperature (C)
Time (s)
Top
High Mid
Low Mid
Bottom

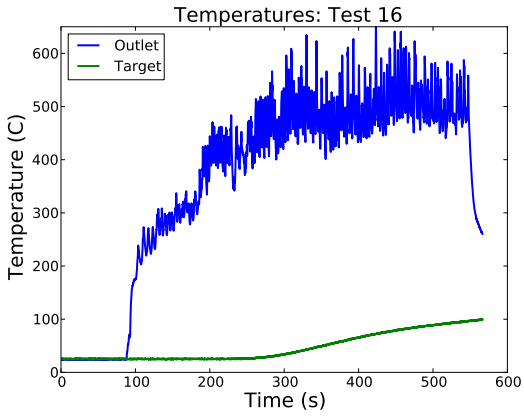
Temperatures: Test 16
Temperature (C)
Time (s)
Outlet
Target

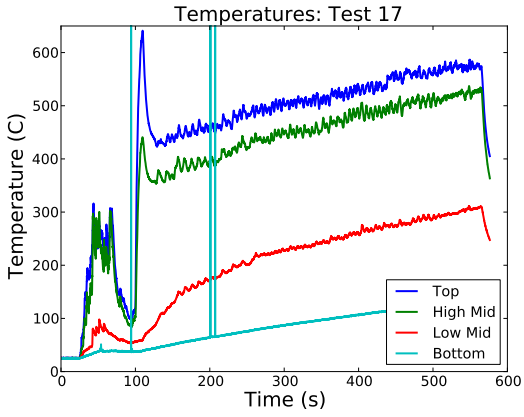
Temperatures: Test 17
Temperature (C)
Time (s)
Top
High Mid
Low Mid
Bottom

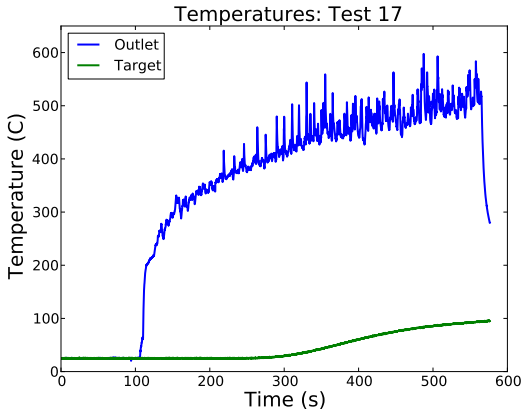
Temperatures: Test 17
Temperature (C)
Time (s)
Outlet
Target

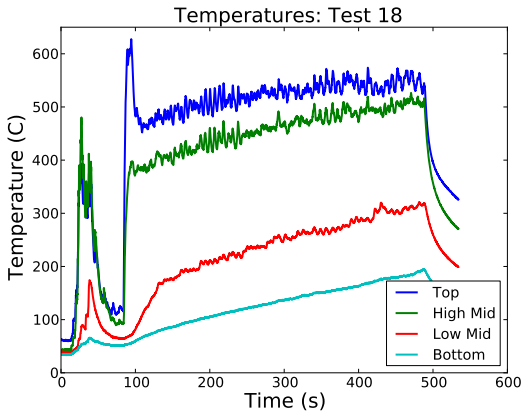
Temperatures: Test 18
Temperature (C)
Time (s)
Top
High Mid
Low Mid
Bottom

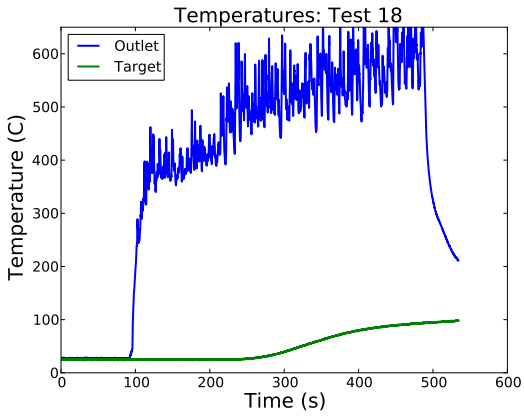
Temperatures: Test 18
Temperature (C)
Time (s)
Outlet
Target

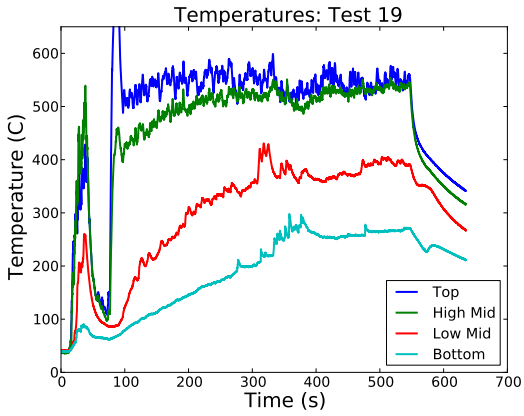
Temperatures: Test 19
Temperature (C)
Time (s)
Top
High Mid
Low Mid
Bottom

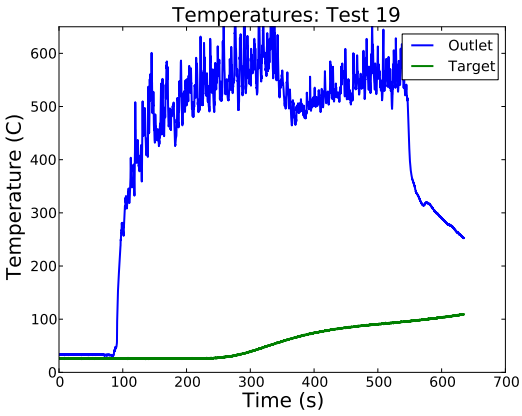
Temperatures: Test 19
Temperature (C)
Time (s)
Outlet
Target

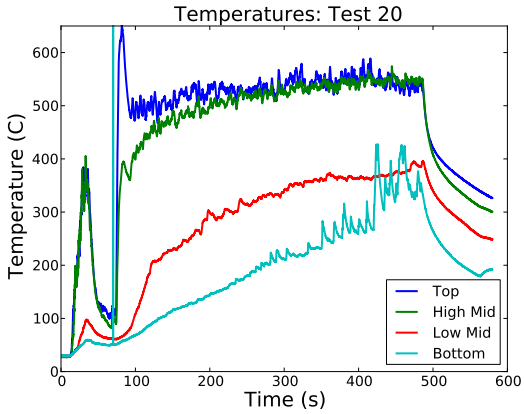
Temperatures: Test 20
Temperature (C)
Time (s)
Top
High Mid
Low Mid
Bottom

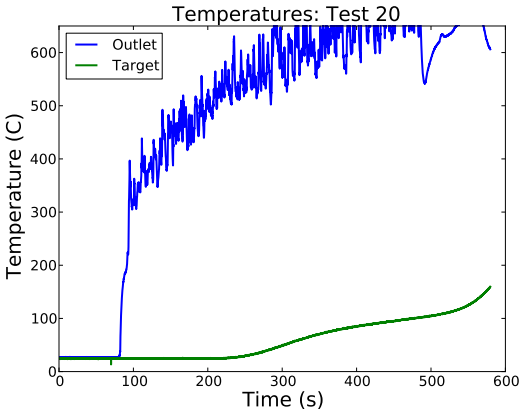
Temperatures: Test 20
Temperature (C)
Time (s)
Outlet
Target

C.3 Pressure Plots

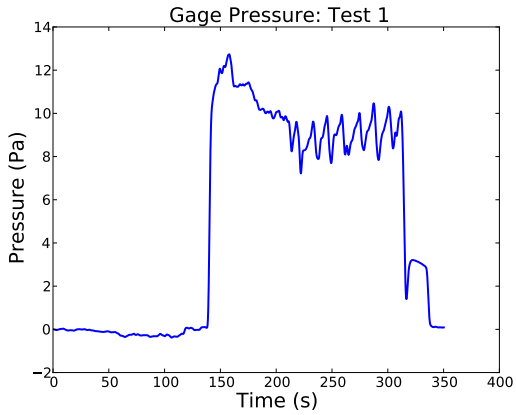

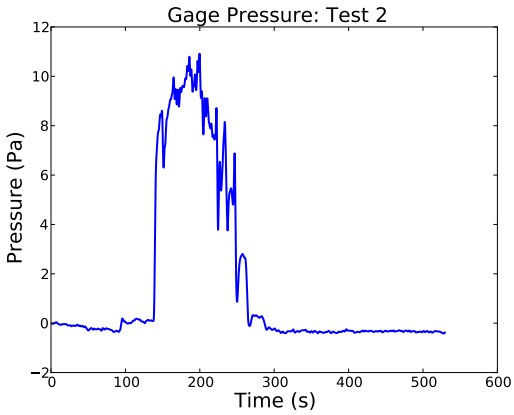

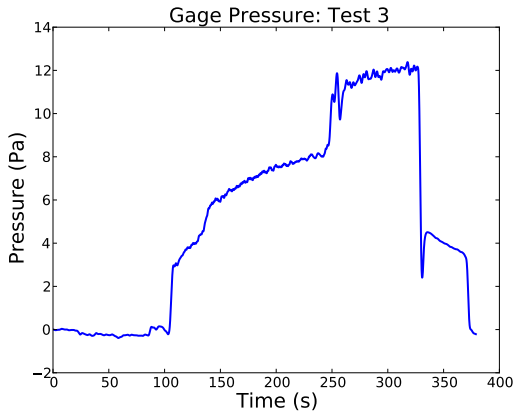

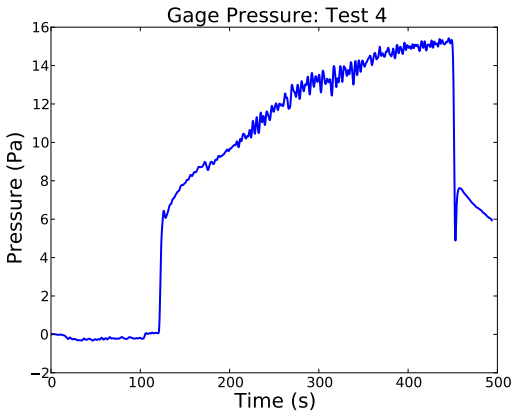

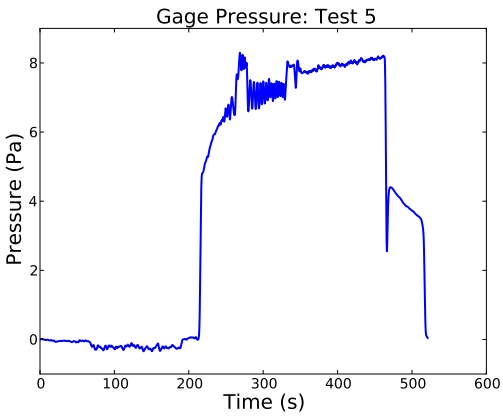

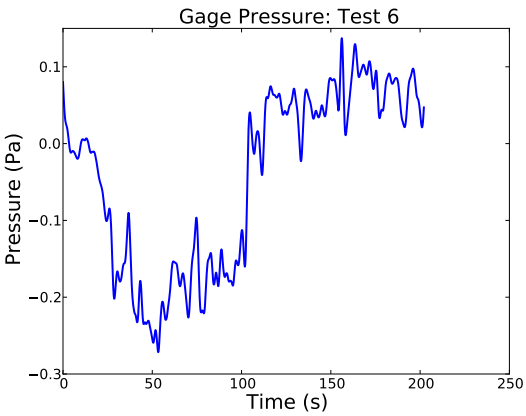

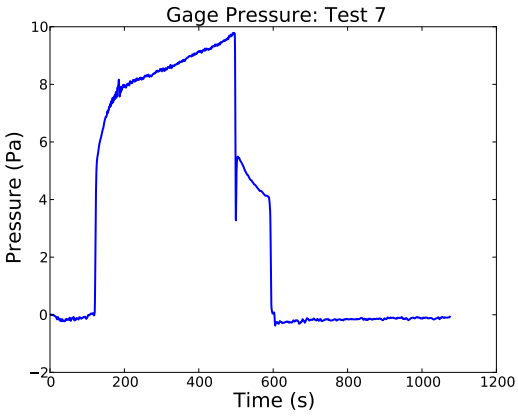
Gage Pressure: Test 7
Pressure (Pa)
Time (s)

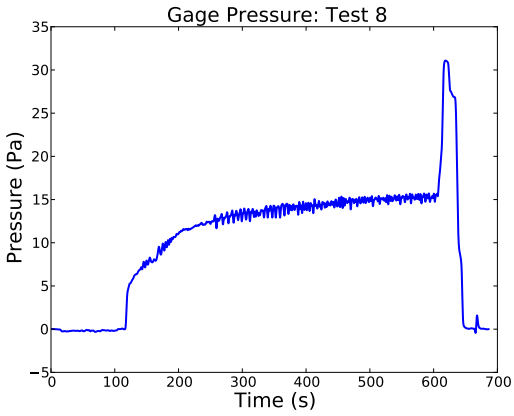
Gage Pressure: Test 8
Pressure (Pa)
Time (s)

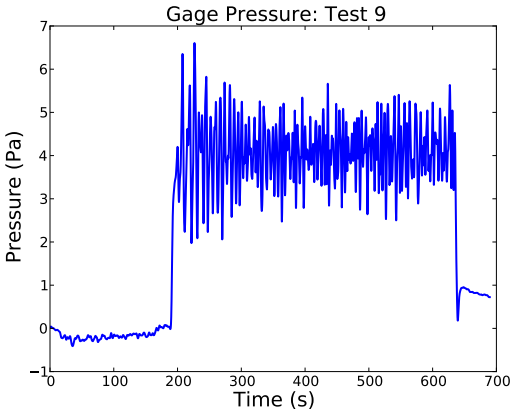
Gage Pressure: Test 9
Pressure (Pa)
Time (s)

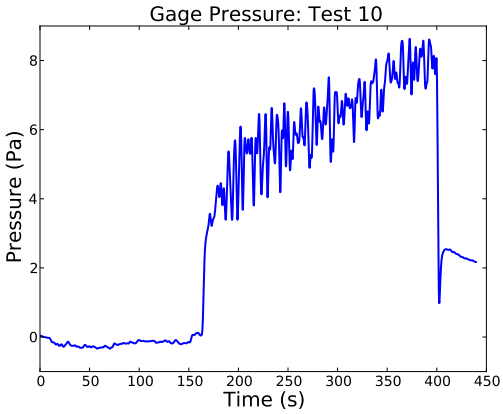
Gage Pressure: Test 10
Pressure (Pa)
Time (s)

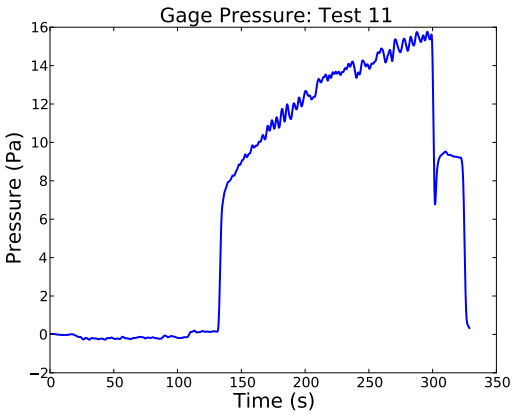
Gage Pressure: Test 11
Pressure (Pa)
Time (s)

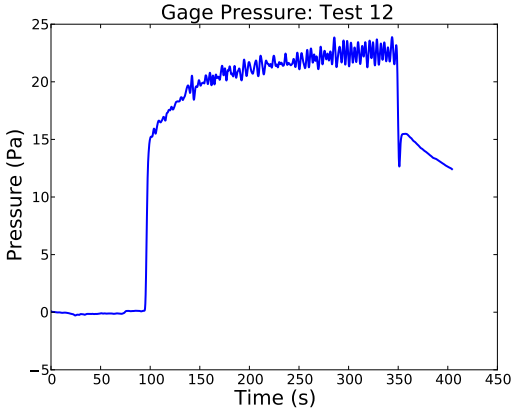
Gage Pressure: Test 12
Pressure (Pa)
Time (s)

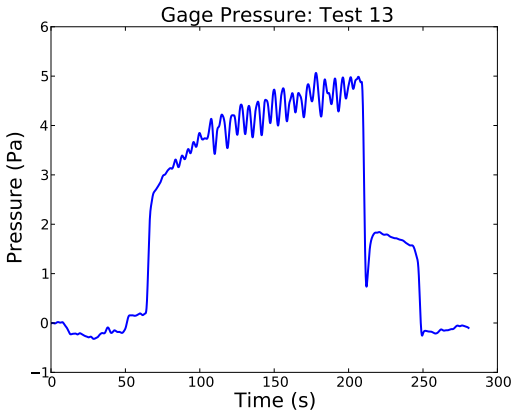
Gage Pressure: Test 13
Pressure (Pa)
Time (s)

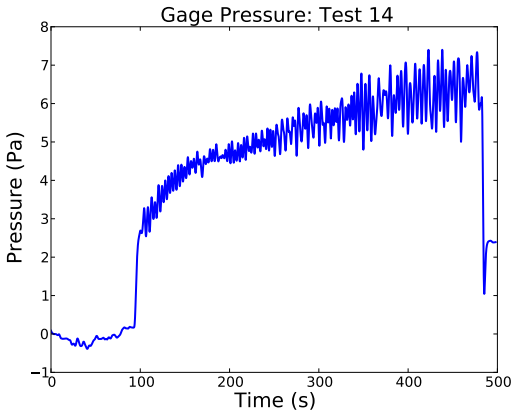
Gage Pressure: Test 14
Pressure (Pa)
Time (s)

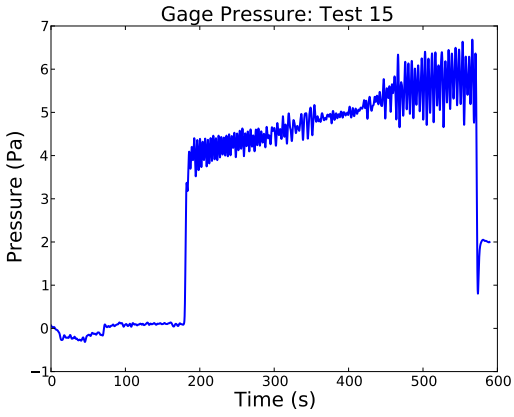
Gage Pressure: Test 15
Pressure (Pa)
Time (s)

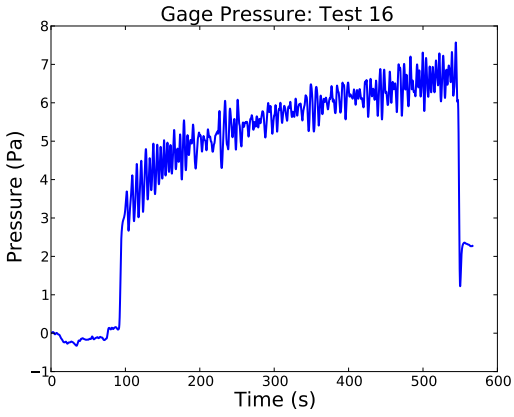
Gage Pressure: Test 16
Pressure (Pa)
Time (s)

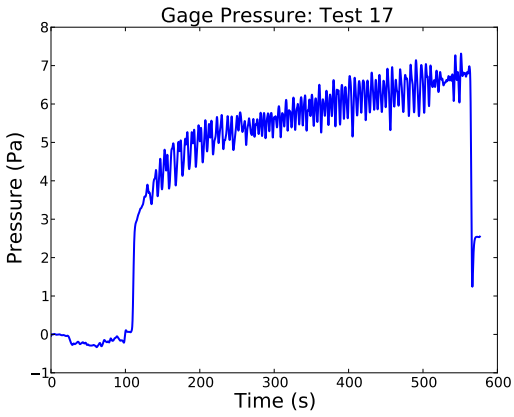
Gage Pressure: Test 17
Pressure (Pa)
Time (s)

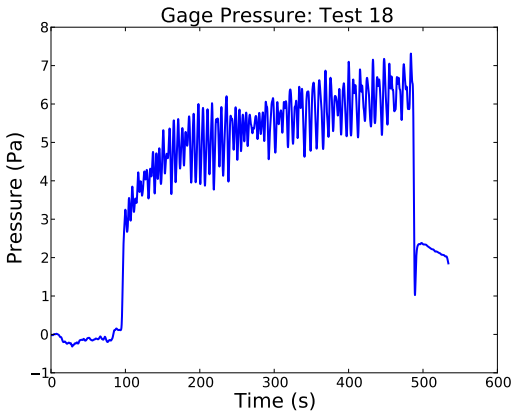
Gage Pressure: Test 18
Pressure (Pa)
Time (s)

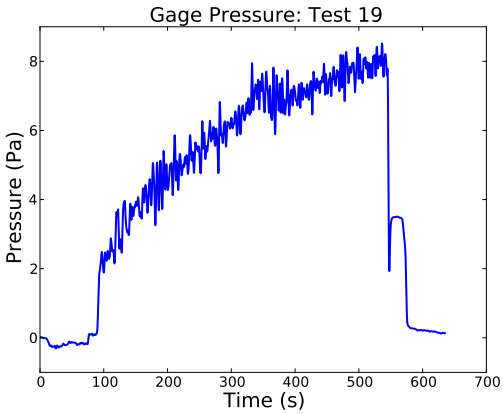
Gage Pressure: Test 19
Pressure (Pa)
Time (s)
0
2
4
6
8
0
100
200
300
400
500
600
700

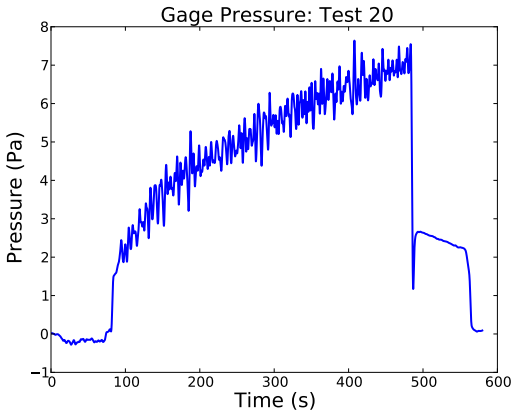
Gage Pressure: Test 20
Pressure (Pa)
Time (s)
−1
0
1
2
3
4
5
6
7
8
0
100
200
300
400
500
600

C.4 Char Patterns

Table C.2: Char pattern dimensions for ignition experiments (*Char pattern reached the edge of the sample).

Target Spacing (cm)	Test #	Horizontal (in)	Vertical (in)
1.0	14	5.7	6.4
	16	6.4	7.0
	18	5.7	6.4
	20	9.5	10.8*
2.5	9	2.2	2.5
	15	4.8	4.8
	17	5.1	5.7
	19	5.7	6.4


Scope 17
Scope 18
Scope 19
Scope 20

Bibliography

[1] H. J. Allen, "Hypersonic flight and the re-entry problem: The twenty-first wright brothers lecture," *Journal of the Aeronautical Sciences*, vol. 25, pp. 217–227, April 1958.

[2] M. C. Adams, "Recent advances in ablaion," *ARS Journal*, vol. 29, p. 625, September 1959.

[3] P. J. Shull, A. V. Clark, P. R. Heyliger, J. C. Moulder, and B. A. Auld, "Characterization of capacitive array for nde applications," *Research in Nondestructive Evaluation*, vol. 2, no. 1, pp. 11–27, 1990.

[4] V. V. Lebedev, "Application of the tikhonov method to solve the inverse heat-conduction problem for a melting plate with melt entrainment," *Journal of Engineering Physics and Thermophysics*, vol. 33, no. 6, pp. 1435–1439, 1978.

[5] J. Wang and N. Zabaras, "A bayesian inference approach to the inverse heat conduction problem," *International Journal of Heat and Mass Transfer*, vol. 47, pp. 3927–3941, May 2004.

[6] H. Molavi, R. K. Rahmani, A. Pourshaghaghy, E. S. Tashnizi, and A. Hakkaki-Fard, "Heat flux estimation in a nonlinear inverse heat conduction problem with moving boundary," *Journal of Heat Transfer*, vol. 132, May 2010.

[7] J. W. Mittendorf, "Reading a building - wood frame construction," *http://www.fireengineering.com/articles/2005/03/reading-a-building-wood-frame-construction.html*.

[8] J. Rimen and M. Thomas, "Use of positive pressure ventilation in fire-fighting operations," *Fire Engineers Journal*, vol. 60, no. 206, pp. 7–13, 2000.

[9] K. Garcia, "PPV: Just the facts," *Fire Engineering*, vol. 155, no. 11, p. 48, 2002.

[10] B. Gustin, "Fog streams and ppv: Their effects on two fires," *Fire Engineering*, vol. 150, no. 11, pp. 49–56, 1997.

[11] R. Scott, "Applying pressure," *Fire Prevention*, no. 362.

[12] P. Ziesler, F. Gunnerson, and S. Williams, "Advances in positive pressure ventilation: Live fire tests and laboratory simulation," *Fire Technology*, vol. 30, no. 2, pp. 269–277, 1994.

[13] S. Svensson, "Experimental study of fire ventilation during fire fighting operations," *Fire Technology*, vol. 37, no. 1, pp. 69–85, 2001.

[14] S. Kerber and W. Walton, "Characterizing Positive Pressure Ventilation using Computational Fluid Dynamics," NISTIR 7065, National Institute of Standards and Technology, Gaithersburg, Maryland, February 2003.

[15] S. Kerber and W. D. Walton, *Effect of positive pressure ventilation on a room fire.* US Department of Commerce, National Institute of Standards and Technology, 2005.

[16] O. A. E. PhD-PE, K. Lakshminarasimhan, P. Seers, and R. Nicks, "Effects of ppv attack on thermal conditions in a compartment downstream of a fire," *Fire Technology*, vol. 41, no. 3, pp. 193–208, 2005.

[17] C. Beal, M. Fakhreddine, and O. A. Ezekoye, "Effects of leakage in simulations of positive pressure ventilation," *Fire Technology*, vol. 45, pp. 257–286, 2009.

[18] C. Weinschenk and O. A. Ezekoye, "Analysis of fireground standard operating guidelines/procedures compliance for austin fire department," *Fire Technology*, vol. 44, p. 3964, 2008.

[19] C. Weinschenk, C. Beal, and O. Ezekoye, "Modeling fan-driven flows for firefighting tactics using simple analytical models and cfd," *Journal of Fire Protection Engineering*, vol. 21, no. 2, pp. 85–114, 2011.

[20] M. Natali, J. H. Koo, E. Allcorn, and O. Ezekoye, "In-situ ablation recession sensor based on ultra-miniature thermocouples-part a: 0.25 mm diameter thermocouples,"

[21] C. Yee, M. Ray, F. Tang, J. Wan, R. Tatuaca, J. H. Koo, and M. Natali, "In-situ ablation recession sensor based on ultra-miniature thermocouples–part b: 0.5 mm diameter thermocouples,"

[22] A. Kurzawski, O. A. Ezekoye, J. H. Koo, C. Yee, and T. Hardee, "Recession experiments and modeling for carbon surface oxidation processes," in *ASME Summer Heat Transfer Conference*, 2013.

[23] M. Natali, L. Torre, and J. Kenny, "Nanostructured ablative thermal protection systems," in *International ECNP Conference on Nanostructured Polymers and Nanocomposites*, 2010.

[24] E. Allcorn, S. Robinson, D. Tschoepe, J. H. Koo, and M. Natali, "Development of an experimental apparatus for ablative nanocomposite testing," in *Proceedings of 47th AIAA/ASME/SAE Joint Propulsion Conference*, 2011.

[25] J. Kiefer, "Sequential minimax search for a maximum," *Proceedings of the American Mathematical Society*, vol. 4, no. 3, pp. 502–506, 1953.

[26] X.-H. Sun and S. Moitra, *A fast parallel tridiagonal algorithm for a class of CFD applications*, vol. 3585. Citeseer, 1996.

[27] American Society for Testing and Materials, West Conshohocken, Pennsylvania, *ASTM E 2257-08 Standard Test Method for Room Fire Test of Wall and Ceiling Materials and Assemblies*, 2008.

[28] O. A. Ezekoye, S. Svensson, and R. Nicks, "Investigating positive pressure ventilation," *Interflam*, vol. 27, p. 2008, 2007.

[29] A. Standard, "119, air leakage performance for detached single-family residential buildings," *American Society of Heating, Refrigerating and Air conditioning Engineers*, 1988.

[30] M. H. Sherman and D. J. Dickerhoff, "Airtightness of us dwellings," *TRANSACTIONS-AMERICAN SOCIETY OF HEATING REFRIGERATING AND AIR CONDITIONING ENGINEERS*, vol. 104, pp. 1359–1367, 1998.

[31] B. McCaffrey and G. Heskestad, "A robust bidirectional low-velocity probe for flame and fire application brief communications," *Combustion and Flame*, vol. 26, no. 1, pp. 125–127, 1976.

[32] K. McGrattan, R. McDermott, S. Hostikka, and J. Floyd, "Fire Dynamics Simulator (Version 6) User's Guide," tech. rep., National Institute of Standards and Technology, 2012.

[33] B. Karlsson and J. G. Quintiere, *Enclosure Fire Dynamics*. CRC PressI Llc, 2000.

[34] M. Wen and K. Jang, "An impingement cooling on a flat surface by using circular jet with longitudinal swirling strips," *International Journal of Heat and Mass Transfer*, vol. 46, no. 24, pp. 4657–4667, 2003.

[35] A. Kanury, *SFPE Handbook of Fire Protection Engineering*, ch. Flaming Ignition of Solid Fuels. Quincy, Massachusetts: National Fire Protection Association, 3rd ed., 2003.

[36] F. P. Incropera, D. P. De Witt, and A. S. Lavine, *Fundamentals of Heat and Mass Transfer*. New York: John Wiley and Sons, 6th ed., 2007.

[37] B. McCaffrey, J. Quintiere, and M. Harkleroad, "Estimating room temperatures and the likelihood of flashover using fire test data correlations," *Fire Technology*, vol. 17, no. 2, pp. 98–119, 1981.

[38] N. Zuckerman and N. Lior, "Jet impingement heat transfer: physics, correlations, and numerical modeling," *Advances in heat transfer*, vol. 39, pp. 565–631, 2006.

[39] B. W. Barr, "Investigation and modeling of coupled thermochemical and thermomechanical erosion in thermally degrading systems," Master's thesis, The University of Texas at Austin, 2012.

[40] V. Babrauskas, *Ignition Handbook*. Issaquah, Washington USA: Fire Science Publishers, 1st ed., 2003. Co-published by the Society of Fire Protection Engineers.

Vita

Andrew Kurzawski was born in Bryan, Texas but he has spent most of his life in Austin, Texas where he graduated from James Bowie High School in 2006. He went on to obtain a Bachelor of Science in Mechanical Engineering from the University of Texas at Austin in 2011. Outside of engineering, Andrew enjoys playing music and being outdoors.

Permanent contact information: ajkurzawski@gmail.com

This thesis was typed by Andrew Joseph Kurzawski.